The Astrophysical Journal, 631:540–571, 2005 September 20

ABUNDANCE ANOMALIES AND ROTATIONAL EVOLUTION OF LOW-MASS RED GIANTS: A MAXIMAL MIXING APPROACH

Julio Chanamé, Marc Pinsonneault, and Donald M. Terndrup
Department of Astronomy, Ohio State University, 4055 McPherson Laboratory, 140 West 18th Avenue, Columbus, OH 43210
Received 2004 December 15; accepted 2005 May 26

ABSTRACT

We use a fully self-consistent evolutionary code to follow the rotational evolution of low-mass red giants, making a comprehensive attempt to assess the role of rotationally induced mixing in the development of abundance anomalies in giants with a range of masses and metallicities in stellar clusters and the field. We adopt a maximal mixing approach with reasonable initial conditions of angular momentum distribution and main-sequence rotation rates as a function of stellar type. Unlike most previous work, we do not focus on the determination of combinations of mixing rate and depth that reproduce the data on a particular stellar type. Instead, we concentrate on the more fundamental problem of the simultaneous reproduction of the patterns of CNO surface abundances in both Population I and Population II giants using the same physics and models. We follow and discuss the essential physics of rotational mixing in terms of the structural and angular momentum evolution along the red giant branch (RGB).

A general result of all our models is that rotational mixing, although present in small amounts, is inefficient on the lower RGB independently of any inhibiting effect of μ-barriers. Therefore, the lack of well-mixed stars before the luminosity of the RGB bump in globular clusters and the field does not constitute unquestionable evidence for the inhibition of mixing by μ-barriers. Instead, we argue that the rapid disappearance of the RGB bump as soon as mixing is allowed to penetrate μ-barriers is what actually constitutes the first solid evidence of such inhibition.

Maximal mixing models with differentially rotating envelopes are able to reproduce the $^{12}C/^{13}C$ data on M67 giants with initial rotation rates adequate to their progenitors but fail to do so for open clusters of larger turnoff mass and for metal-poor giants in the field and globular clusters. Possible solutions are discussed. Our favored scenario is one in which the overall strength of canonical extra mixing has been underestimated by existent derivations, but which additionally needs to be coupled with a much lower efficiency for rotational mixing among the rapidly rotating open cluster giants than in the slowly rotating ones in the field and globular clusters. We hypothesize that this last requirement is provided by the interaction between convection and rotation in the envelopes of giants, in the sense that rapidly rotating stars would develop much shallower angular velocity profiles in their envelopes than do slowly rotating stars.

Subject headings: stars: abundances — stars: evolution — stars: rotation

1. INTRODUCTION

Theoretical models of stellar structure and evolution have traditionally neglected rotation, even though stars have been known to rotate since the 17th century (Galilei et al. 1613). The reasons for this are essentially three: the remarkable agreement of standard[1] models with large quantities of observational data; the fact that, typically, rotation amounts for just a small perturbation on the structure of stars; and, finally, because of the much larger complexity involved in modeling objects not in spherical symmetry. However, modern observations, particularly regarding anomalous patterns of chemical abundances, clearly require additional physics. Convection, the only mechanism of internal mixing contemplated by standard models, is not able alone to account for the large and varied levels of mixing seen in stars across different evolutionary stages, and stellar rotation probably constitutes the most likely missing ingredient: because of the varying gravity on an equipotential surface, a rotating star cannot simultaneously satisfy both hydrostatic and radiative equilibrium (von Zeipel 1924), and large-scale internal motions (i.e., mixing) inevitably arise in order to compensate the imbalance (Eddington 1925, 1929; Vogt 1925). In this work, we address the problem of the surface abundance anomalies[2] in low-mass (0.8–2 $M_{\odot}$) red giants using stellar models that incorporate rotation and its extra-mixing properties. By combining observational constraints on the angular momentum properties of the Sun and other stars in various evolutionary stages, we develop a "maximal rotational mixing" scenario intentionally aimed to identify the advantages and limitations of this mechanism to reproduce the well-documented anomalies in the CNO surface abundances of first-ascent giants in the field and stellar clusters.

In standard models, the only opportunity for the surface convection zone of first-ascent red giants to reach nuclear processed material is known as the first dredge-up (Iben 1965). As the star moves from the main sequence (MS) to the red giant branch (RGB), the base of the convective envelope, while staying roughly at the same physical radius, deepens considerably in the mass coordinate. At its point of maximum penetration, the convective envelope encompasses about 75% of the total mass of a 1.3 $M_{\odot}$ star of solar metallicity. This first dredge-up ends when the base of the convective envelope has reached its maximum

[1] By standard we mean nonrotating, spherically symmetric models, where magnetic fields play no role, and the only mixing agent is convection.

[2] Abundance anomalies studied in this work involve stellar material that has gone through nuclear reactions and is transported to the stellar surface and should not be confused with anomalies that can be produced by gravitational settling and radiative levitation. For a recent account of such effects, which can be important in turnoff and subgiant stars, see Michaud et al. (2004).

depth and then starts to retreat (again, in the mass coordinate). After this point in the evolution, no changes in the surface abundances are produced by standard models.

Observational evidence for mixing beyond the standard model is rich, coming from measured abundances of elements such as helium, lithium, carbon, nitrogen, oxygen, sodium, etc., and is constantly and rapidly growing. Although in varying amounts, giants in both the cluster and field environments show clear signs of nonstandard mixing. Red giants in different stellar systems and environments provide information and clues on the mixing processes that are complementary to each other and, therefore, a serious attempt to understand the evolution of their surface abundances must always account for the entire phenomenology. Reviews on this subject can be found in Kraft (1994), Pinsonneault (1997), and Salaris et al. (2002).

We defer to § 2 a review of the observational evidence for extra mixing in giants in stellar clusters and the field, which the reader familiar with the subject may skip. Here we only point out the marked contrast between the anomalous surface abundances seen in red giants that belong to different Galactic populations: while Population I giants in open clusters (1.3 $M_{\odot}$ and above) exhibit very mild levels of extra mixing, the much older, less massive Population II giants in globular clusters (0.8–0.9 $M_{\odot}$) show largely anomalous patterns of surface abundances, in clear disagreement with standard models.

Abundance anomalies developing as a function of increasing luminosity along the RGB, primarily displayed by the lightest species and now seen in both clusters and the field, offer no doubt that some of the nonstandard changes must be evolutionary in nature and intrinsic to stars. Also, trends of the CNO abundances with metallicity are consistent with an evolutionary scenario: due to their lower opacities, more metal-poor stars are hotter at any given depth than their metal-rich counterparts, placing the regions of CN and ON processing closer to the surface and hence making it easier to transport nuclear processed material to the surfaces.

On the other hand, the heavier species involved in anomalies in red giants, Na, Mg, and Al, do not show a clear evolution with position along the RGB. Furthermore, the large star-to-star abundance variations among MS stars and early subgiants in globular clusters (in contrast with field stars), as well as trends involving species that burn at temperatures most likely higher than those attainable by first-ascent giants, indicate the presence of inhomogeneities in the cluster material that must be primordial to the current giants and dependent on the environment.

Hence, it has become increasingly evident that these two scenarios (evolutionary and primordial; Kraft 1994) for the origin of the abundance anomalies are not mutually exclusive, but rather they must be simultaneously at work, i.e., that initial abundance differences from star to star in the same globular cluster are further modified by a nonstandard mixing mechanism interior to the stars that operates during the giant branch evolution (for the case of M13 see Briley et al. 2002).

Two broad classes of models of extra mixing have been developed in order to account for the patterns of abundance anomalies in red giants, the difference between them being whether they incorporate or not, in a self-consistent manner, the underlying physical mechanism responsible for the additional mixing. The first class of models, which could be generally referred to as "parametric diffusion models," simulate the extra mixing by adding a diffusion term to the equation for the temporal variation of the abundances of chemical species at any given mass shell inside the star. In these models the problem is reduced to the determination of two parameters that control the mixing: depth and rate (Sweigart & Mengel 1979; Smith & Tout 1992; Charbonnel 1995; Wasserburg et al. 1995; Denissenkov & Weiss 1996; Denissenkov et al. 1998; Boothroyd & Sackmann 1999; Denissenkov & Tout 2000; Weiss et al. 2000; Denissenkov & VandenBerg 2003). Since these are essentially standard models on top of which ad hoc extra mixing is simulated, their fundamental shortcoming is either one or both of the following: (1) they do not implement the physical mechanism(s) driving the extra mixing, or (2) they do not account for the feedback effects that the redistribution of chemical composition can have on the structure and evolution of the star. On the other hand, they are helpful since they do identify the temperature to which mixing must be able to reach inside the star.

The second class of models is based on the actual implementation of mechanisms responsible for the nonstandard mixing, all of which are associated with different ways of transporting angular momentum in the stellar interior. These mechanisms are magnetic fields (Mestel & Weiss 1987; Charbonneau & MacGregor 1992, 1993; Spruit 1999, 2002; Maeder & Meynet 2003, 2004), gravity waves (Press 1981; Kumar & Quataert 1997; Zahn et al. 1997; Kumar et al. 1999; Talon & Zahn 1998; Talon et al. 2002; Talon & Charbonnel 2003, 2004), and hydrodynamic instabilities triggered by differential rotation. All these are known to interact with the angular velocity field inside stars and thus are potential mixing agents. However, while their relative importance in different evolutionary stages is still a work in progress, there are reasons to expect that both magnetic fields and gravity waves do not play an important role in the transport of angular momentum in red giants.

Being capable of exerting torques, magnetic fields have the potential to be efficient agents in the redistribution of angular momentum (although not necessarily chemicals). However, the existence of fast rotators among horizontal branch (HB) stars in globular clusters and the field provides solid evidence that a high degree of differential rotation is preserved during the RGB evolution (Sills & Pinsonneault 2000), thus arguing against not only magnetic fields, but any means of efficient angular momentum transport. Furthermore, the timescale for angular momentum evolution (tied to the timescale for magnetic field evolution), as indicated by observations of open clusters of different ages, is of the order of $\sim$100 Myr, comparable to the entire duration of the RGB phase. Therefore, there is not enough time for any magnetically induced mixing to operate significantly on this evolutionary phase. The importance of waves, on the other hand, is always determined by the balance between excitation and damping. Waves are excited near boundary layers, such as the base of the convective envelope, but would hardly be able to reach the required depths since, due to the large physical sizes of evolved stars, they would be easily damped.

Stellar rotation was found long ago to be a promising nonstandard mechanism to explain some of the abundance anomalies introduced before. Extra mixing induced by rotation appears in two forms, one associated with the global departure from spherical symmetry, and another due to internal angular velocity gradients. In the first, the latitude-dependent centrifugal acceleration makes the effective gravity smaller at equatorial zones than at the poles, generating large-scale flows of matter in meridional planes to compensate for the pressure and temperature imbalance between poles and equator (Eddington 1925, 1929; Vogt 1925). This meridional circulation also transports chemicals and therefore mixes the deep interior of stars (Sweigart & Mengel 1979). The second type of rotational mixing arises when large internal gradients of angular velocity inside radiative regions trigger hydrodynamic instabilities that redistribute the angular momentum

and, in the process, mix the material (Endal & Sofia 1978; Pinsonneault et al. 1989). While meridional circulation can take place in any evolutionary state, mixing via hydrodynamic instabilities is largely favored by the large internal shears that develop with the structural changes in post-MS stages.

The efficiency of both types of rotational extra mixing is an increasing function of the rotation rate; therefore, they have different impacts on different types of stars. The dependence of rotation rate on stellar type is commonly known as the Kraft curve (Kraft 1967) and can be summarized as follows. Early-type stars show a wide range of surface rotation rates and can reach velocities of 200 km s^{-1}, while late-type stars all rotate very slowly, almost never exceeding 10 km s^{-1}. The transition between these two regimes is extremely steep and occurs throughout stellar type F, a fact probably associated with the development of a deep surface convection zone (CZ) and magnetized winds that carry away angular momentum very efficiently.

The direction of this dichotomy between the rotation levels of early- and late-type stars, therefore, presents a fundamental puzzle for the theory in light of the patterns of abundance anomalies discussed before: how is it that the open cluster giants (whose progenitors belonged to the rapidly rotating part of the Kraft curve) display much milder levels of extra mixing than the globular cluster giants (whose progenitors rotated very slowly), if the mechanisms for extra mixing are increasing functions of the rotational velocity? This basic question, as far as we know, has not been addressed yet in the literature available on this subject and constitutes one of the goals of the present work (§§ 6.4 and 7.2).

Fully self-consistent models of rotational extra mixing are few, and all of them are restricted to the lower MS (Pinsonneault et al. 1990; Charbonnel et al. 1992; Chaboyer et al. 1995a, 1995b; Talon & Charbonnel 1998; Palacios et al. 2003) and high-mass stars (Meynet & Maeder 1997; Talon et al. 1997; Maeder & Meynet 2000). Such models are only now being applied to the case of low-mass giants, although there have been two studies that got close to that goal and are worth mentioning. The first of these is the seminal work of Sweigart & Mengel (1979), who studied classical meridional circulation as a mechanism of mixing CNO-processed material into the envelope following a procedure that, while being physically motivated, can be viewed as a variation of parametric diffusion models. Although not able to account for the evolution of the angular momentum profile or feedback effects, Sweigart & Mengel (1979) were capable of relating the interior rotation rates that are needed to produce the necessary mixing with the rotation at the surface. This already made them realize the need for the convective envelopes of low-mass giants to have differential rotation in order to achieve any extra mixing through rotational effects, a fact more recently demonstrated through the comparison of the rotation rates of HB stars in globular clusters with those of their MS progenitors (Sills & Pinsonneault 2000). The second of these semi–self-consistent models of rotational mixing in low-mass giants is that of Denissenkov & VandenBerg (2003), who adopted the theoretical framework of anisotropic turbulent mixing of Chaboyer & Zahn (1992) and Zahn (1992) to compute the strength of extra mixing associated with rotation, although they neglected the transport of angular momentum in radiative regions. However, Denissenkov & VandenBerg (2003) adopt what in our view is an unrealistic initial distribution of angular momentum (strong differential rotation during the MS) and, even then, find that their diffusion coefficients are still too small to account for the levels of mixing exhibited by the data. Finally, and most importantly, none of these works address the issue of the existence of different patterns and levels of extra mixing among stars of different populations.

In the present work, we make use of a stellar evolutionary code that includes rotation and treats the transport of angular momentum and chemical species in a fully self-consistent way, i.e., accounting for the impact of such redistributions on the structure of the star at each time step. Our main goals are the study of the evolution of the surface abundances in rotating low-mass giants of all types and environments using the same underlying physics, as well as the understanding of the roles of the various ingredients that determine the angular momentum and mixing histories in these stars. Similarly, since stars of different types show quite different rotational properties, special emphasis is placed on the adoption of initial conditions and assumptions in agreement with observational constraints. To do this, we evolve models of both Population I and Population II stars from the MS turnoff to the tip of the RGB using initial rotation rates adequate to their corresponding MS progenitors and compare our results to the data on the surface abundances of giants in open and globular clusters, as well as the field.

In particular, we ask ourselves the following question: assuming the most favorable (although physically plausible) set of conditions for extra mixing driven by rotation, is it possible to reproduce the CNO abundance patterns seen in Population I and Population II red giants of all environments (§ 2)? To answer this question, we study the consequences of rotational mixing under conditions for *maximal mixing*, among which we identify no transport of angular momentum and neglecting any inhibiting effect of composition gradients (§ 3). Thus, rotational mixing will be essentially driven by the evolution of the angular velocity field and hydrodynamic instabilities arising in response to the structural changes occurring during the post-MS evolution. In § 3 we outline our treatment of stellar rotation and the induced mixing, the input physics, and the initial conditions of our models with maximal mixing. In §§ 4 and 5 we discuss the structural and angular momentum evolution of the models and the overall properties of the induced extra mixing. The comparison with observations is done in § 6, where we also introduce a working hypothesis that could account for the different levels of mixing between Population I and Population II giants simultaneously and without conflict with the contrasting rotational regimes of their progenitors. Finally, we summarize our findings and present our conclusions in § 7.

2. A REVIEW OF THE EVIDENCE FOR EXTRA MIXING IN RED GIANTS

Open clusters in the Galactic disk provide us with giants with a range of ages (from a few tens of millions of years to several billion years) and, therefore, trace the dependence of mixing on stellar mass. The primary disadvantage of using open cluster giants is that nature has not provided us with open clusters that span the full ranges of metallicity and age. Furthermore, open clusters typically contain relatively few stars, and by extension there will be few members in short phases of evolution such as the upper RGB.

Globular clusters, on the other hand, are very populous and in principle can trace the entire RGB evolution of the surface abundances of single-mass giants, providing information as a function of luminosity. Because of their distances from the Sun, however, spectroscopic studies of globular cluster giants were typically restricted to the most luminous stars, those close to the RGB tip, although this situation has been progressively changing with the use of 8–10 m class telescopes. In addition, globular cluster giants are the oldest and most metal-poor cases, thus

probing the domains of the lowest mass and longer lived giants that are possible to find.

Things are more difficult in the field, but nevertheless some authors have managed to assemble fair samples of stars with well-determined evolutionary states and studied their abundance patterns, usually relying on parallax data from *Hipparcos* and the work of previous investigators that determined accurate physical parameters for these stars. Field giants sample predominantly old and low-mass MS precursors. Such giants are relatively bright and provide data across a range of metallicities but little direct information on the mass of the precursors. Nevertheless, field giants give us indications on the evolution of the surface abundances as a function of environment through the comparison of Population I field giants with those in the sparse open clusters and of Population II field giants with those in dense globular clusters.

Typical indicators of mixing have been lithium and the CNO species, but also Na, Mg, Al, and others have been studied. Burning at temperatures higher than $\sim 2.5 \times 10^6$ K, Li is by far the most fragile among these tracers, and measurements of its abundance are a powerful test of models of MS stars of different spectral types (Balachandran 1995; Pinsonneault 1997). However, Li exhibits a complex MS depletion pattern in Population I stars below about 1.5 $M_\odot$, and more massive stars are too hot to permit its measurement on the MS. Thus, we focus most of our attention on the surface abundances of the CNO species, which are not expected to evolve during the MS lifetimes of low-mass stars. Since the reactions of the CNO cycle of hydrogen burning are highly temperature sensitive (heavier species burn at higher temperatures), any internal mixing reaches regions of CN processing more easily than regions of ON processing; therefore, anomalies in the ratios of $^{12}C/^{13}C$, C/N, and (C+N)/O probe, in that order, progressively deeper mixing.

Finally, at even higher temperatures, proton-capture reactions in the neon-sodium and magnesium-aluminum cycles can potentially produce enhancements of Na and Al, but it is still a matter of debate whether some of the anomalies among these elements are due to internal mixing or environmental effects (Denisenkov & Denisenkova 1990; Langer et al. 1993; Armosky et al. 1994; Wasserburg et al. 1995; Pagel 1997; Denissenkov et al. 1998; Denissenkov & Weiss 2001, 2004; Denissenkov & Herwig 2003).

The surface abundance patterns among open cluster giants were thoroughly studied by Gilroy (1989) and can be summarized as follows. The most sensitive indicator of CNO-processed material, the ratio of the carbon isotopes, is consistent with standard first dredge-up expectations ($^{12}C/^{13}C \sim 30$) only among massive red giants, that is, those in open clusters with turnoff masses above $\sim 2\ M_\odot$. Red giants in clusters below this turnoff mass exhibit values of $10 \lesssim {}^{12}C/{}^{13}C \lesssim 20$, considerably lower than the standard predictions. Faint giants (i.e., close to the base of the RGB) in the $\sim$4.5 Gyr old open cluster M67 (Gilroy & Brown 1991), with masses around 1.3 $M_\odot$, show $^{12}C/^{13}C$ ratios consistent with standard models, but anomalously low $^{12}C/^{13}C$ values are obtained for all clump giants (He-burning HB stars past the He flash), suggestive of a nonstandard mixing episode occurring sometime along the upper RGB (see also Tautvaisiene et al. [2000], who obtained systematically larger values of $^{12}C/^{13}C$ but reported similar overall trends).

The overall pattern found in field stars is consistent with the properties of old open cluster stars, but also indicating a metallicity dependence. Population I giants in the field ($[Fe/H] \gtrsim -0.5$) show a pattern similar to M67, with stars on the lower RGB showing ratios $^{12}C/^{13}C \sim 40$ and stars brighter than some luminosity showing $^{12}C/^{13}C \sim 13$, again, much lower than expected just from standard first dredge-up (Shetrone et al. 1993). More metal-poor field giants ($-2.2 \leq [Fe/H] \leq -0.2$) experience a similar evolution but reach systematically lower $^{12}C/^{13}C$ ratios than their Population I counterparts in the field (Pilachowski et al. 1997; Keller et al. 2001), evidencing a trend of stronger mixing with decreasing metallicity. In a thorough analysis of the abundances of a large sample of metal-poor field (halo and thick disk) stars restricted to a narrow mass range, Gratton et al. (2000) found good agreement with standard first dredge-up predictions among stars in the lower giant branch but confirmed a second, nonstandard mixing episode kicking in just after the occurrence of the RGB bump.[3] There is evidence for changes in both the $^{12}C/^{13}C$ ratio and the C/N ratio consistent with in situ mixing above the bump: carbon decreases and nitrogen increases with luminosity and there is a steady drop in the $^{12}C/^{13}C$ ratio from its post–first dredge-up value of $\sim$30 to values $\lesssim$10. Furthermore, the Gratton et al. (2000) data also extend to the subgiant branch (SGB), as well as unevolved MS field stars, and these do not display any anomalies or changes in their surface abundances with evolutionary state. This will be an important point when we turn to the origin of the RGB abundance anomalies.

Giants in globular clusters display all the phenomenology of their counterparts in open clusters and the field, but with two key differences: the nonstandard mixing is even deeper, and there are clear signs of abundance variations already in place before the stars evolve to the giant branch. Deeper mixing is evidenced not only by $^{12}C/^{13}C$ ratios even lower than the most mixed field or open cluster giants, usually reaching as low as the nuclear equilibrium value of $^{12}C/^{13}C \approx 4$ (Suntzeff & Smith 1991; Shetrone 1996b; Briley et al. 1997; Smith et al. 2002; Pilachowski et al. 2003), but also by anomalies likely involving oxygen depletion, which only occurs at temperatures higher than those of the CN cycle (Pilachowski 1988; Brown et al. 1991; Sneden et al. 1991; Minniti et al. 1996; Smith et al. 1996; Cohen & Meléndez 2005). Although known for a long time to be the case in field giants, a clear evolution of the surface $^{12}C/^{13}C$ ratios with increasing luminosity along the RGB of globular clusters was seen only recently by Shetrone (2003) in the clusters M4 and NGC 6528, also finding that the transition luminosity corresponds well to the location of the luminosity function (LF) bump in these clusters. A clear decline in total carbon with increasing luminosity is seen in globular clusters such as M3, M13, NGC 6397, and M92 (Bellman et al. 2001; Smith & Martell 2003), and whenever nitrogen abundances are available, they are typically anticorrelated with carbon (Kraft 1994). More recently, large star-to-star variations in the carbon and nitrogen abundances have been found among subgiants and MS turnoff stars in various globular clusters (Ramírez & Cohen 2002; Cohen et al. 2002; Briley et al. 2002; Cohen & Meléndez 2005; Carretta et al. 2005), showing also the strong anticorrelation expected from

[3] The luminosity function bump, or RGB bump, is a standard feature of the color-magnitude diagram that is also a consequence of the deepening of the convective envelope in first-ascent giants and will be important throughout this work. This feature is due to a slowdown of the evolution of first-ascent giants produced when the hydrogen-burning shell crosses, and erases, the discontinuity in mean molecular weight left behind by the envelope at its point of deepest penetration. It observationally appears as an excess of stars in the differential LF or as a change of slope in the cumulative one, its exact position being metallicity dependent, and has been detected in several Galactic globular clusters (King et al. 1985; Fusi Pecci et al. 1990; Ferraro et al. 1999; Zoccali et al. 1999), as well as some Local Group galaxies (Majewski et al. 1999; Bellazzini et al. 2001, 2002; Monaco et al. 2002).

C → N cycling of this material. Some of these data may also require the occurrence of O → N cycling.

Finally, one of the most ubiquitous trends seen among globular cluster giants is a striking anticorrelation between oxygen and sodium, first noticed by Peterson (1980) in M13 giants and since then confirmed in a large number of clusters (Sneden et al. 1992, 1994, 1997; Kraft et al. 1993, 1995, 1997, 1998; Brown & Wallerstein 1992; Minniti et al. 1996; Shetrone 1996a; Ivans et al. 1999, 2001; Grundahl et al. 2002; Ramírez & Cohen 2002, 2003; Yong et al. 2003; Cohen & Meléndez 2005; Carretta et al. 2005). This O-Na anticorrelation is often accompanied by a similar behavior between magnesium and aluminum (Shetrone 1996b; Ivans et al. 1999; Yong et al. 2003). In contrast, field stars do not show any signs of O or Na abundance variations, much less any anticorrelation, all the way from the MS to the RGB tip (Gratton et al. 2000). These proton-capture anomalies have now been traced back to the SGB and all the way to the MS turnoff (Ramírez & Cohen 2002, 2003; Cohen & Meléndez 2005), thus probably indicating that they did not originate in the current generation of stars.

3. METHOD

3.1. *On the Treatment of Rotation and the Extra Mixing*

We use the Yale Rotating Evolution Code (YREC; Guenther et al. 1992) to model the evolution of low-mass stars from the pre-MS up to the tip of the RGB, just before the onset of the helium flash. Although stellar rotation is an inherently three-dimensional problem, YREC solves for the structure of the rotating star in one dimension by following the scheme initially proposed by Kippenhahn & Thomas (1970) and later modified by Endal & Sofia (1976). Under this treatment, one defines an effective potential composed by the sum of the usual (spherically symmetric) gravitational potential and a centrifugal potential. The latter depends on the distance to the axis of rotation, rather than the distance to the center, thus breaking spherical symmetry. All variables are computed on the resulting nonspherical equipotential surfaces, and an effective gravity can be defined as the gradient of the effective potential. As a result, the effective gravity varies with latitude on equipotential surfaces; it is still perpendicular to them everywhere, but, except for poles and equator, it does not point to the center of the star anymore. Of the four equations of stellar structure, only those of hydrostatic equilibrium and radiative energy transport need to be modified to account for the new form of the potential (for the modified equations see Sills et al. 2000). An important restriction on this scheme is that it assumes that the potential is conservative, and this is not valid when the star is changing in size. Hence, during the giant phase, when the star's envelope expands by over 2 orders of magnitude, it is important to take sufficiently small time steps so as to minimize the error introduced by this assumption. For details of this implementation see Endal & Sofia (1976) and Pinsonneault et al. (1989). Here we only describe the two issues that are most relevant to this work, namely, the angular momentum distribution and transport across the star, and the treatment of the mixing processes.

Two factors determine the evolution of the internal rotational profile along the giant branch: the efficiency of angular momentum transport across the star, and angular momentum loss due to mass loss and/or stellar winds. Since both gravity waves and magnetic fields are not expected to be important during this evolutionary stage (§ 1), we only consider meridional circulation and hydrodynamic instabilities driven by the star's rotation as mechanisms for angular momentum transport. After the structure of the star is calculated at each time step in the evolution, three things determine the new angular velocity profile: local conservation of angular momentum in radiative regions, the assumption for the rotation law in convective regions, and the amount of angular momentum loss. Once these are determined, the gradients of angular velocity are computed and their stability is analyzed. When an unstable angular velocity gradient appears, the corresponding hydrodynamic instability whose stability criterion is not being fulfilled is triggered, rearranging the angular momentum profile until it meets the stability conditions again. Simultaneously, the redistribution of angular momentum is accompanied by a redistribution of the chemical composition, i.e., mixing. The effect of typical mass-loss rates is small (Sills & Pinsonneault 2000).

Also, the diffusion of elements may be affected by gradients of chemical composition, and this can happen in two ways. First, the pole-to-equator pressure imbalance resulting from the different centrifugal accelerations as a function of latitude on equipotentials, which is what drives meridional circulation on the first place, can be actually accommodated without the need for circulation if the chemical composition on equipotentials has the right distribution. This can be immediately realized from the equation of state of a perfect gas if allowing the pressure P and the mean molecular weight μ to vary and keeping the other thermodynamic quantities fixed. Under the picture of anisotropic turbulence of Zahn (1992), it is the strong horizontal turbulence that homogenizes the composition on equipotential surfaces, thus maintaining the latitudinal pressure imbalance that drives large-scale circulation. The second effect of composition gradients may be appreciated with an energy argument, by considering that in order to lift a mass element of molecular weight μ_1 into a region of $\mu_2 < \mu_1$, one actually needs to do some work on the mass element. Kippenhahn & Weigert (1990) illustrate this with the help of stability arguments similar to the Schwarzschild criterion for convection. Consider, for example, Eddington circulation, and imagine a small element of stellar material being lifted by uprising meridional currents. Suddenly, this volume element finds itself surrounded by material of lower molecular weight, thus requiring a similarly positive temperature difference between the element and its surroundings in order to maintain mechanical equilibrium (i.e., no pressure or density difference). Being hotter than its surroundings, it has to radiate the excess energy, which, under pressure equilibrium, necessarily leads to an increase in density. Therefore, the mass element sinks back again, reacting on the meridional currents that made it rise in the first place. First realized by Mestel (1953), this feedback is modeled as an additional velocity, a "μ-current," that opposes the meridional ones. For large enough "μ-gradients," this mechanism could potentially inhibit circulation, and one speaks of "μ-barriers."

Such a μ-barrier actually appears during the giant branch phase when the convective envelope reaches its maximum depth at the end of the first dredge-up, retreating afterward and leaving behind a sharp hydrogen discontinuity, i.e., effectively a μ-barrier. Sweigart & Mengel (1979) argued that, assuming that circulation currents cannot penetrate this μ-barrier, and given that the temperature immediately above it is not high enough even for C → N processing to occur, any mixing of CNO processed material into the envelope would be prevented as long as this μ-barrier stays. Observationally, the abundance patterns along the RGB seem to indicate that the nonstandard extra mixing sets in only after the location of the RGB bump (Gilroy & Brown 1991; Gratton et al. 2000; Keller et al. 2001; Shetrone 2003; Charbonnel 1994; Charbonnel et al. 1998), that is, once this

μ-barrier has been erased by the advancing hydrogen-burning shell (HBS), hence apparently confirming the Sweigart & Mengel (1979) picture. There is, however, the case of M92: Bellman et al. (2001) showed that, despite the appreciable scatter in the carbon abundance at any luminosity along the RGB, the onset of carbon depletion in this cluster occurs well before its LF bump (see also Smith & Martell 2003), the location of which has been determined by observations (Fusi Pecci et al. 1990). We discuss inhibition of mixing by μ-barriers in § 5.

Parametric diffusion models have typically imposed this inhibition of mixing before the LF bump based on the aforementioned observations and theoretical expectations (Charbonnel 1995; Wasserburg et al. 1995; Boothroyd & Sackmann 1999; Weiss et al. 2000). However, a self-consistent treatment of nonstandard mixing must obtain such inhibition, if any, from first principles rather than imposing it as a universal property of stars. Since the purpose of this work is to investigate the properties of rotational mixing under the most favorable conditions for it, we do not consider the opposing effect of μ-barriers.

We anticipate that the above decision leads to the realization of several facts on the angular momentum evolution and mixing properties of red giants that have been overlooked before. For example, we find that mixing induced by rotation is inefficient in the lower RGB (i.e., before the LF bump) without any regard to the effects of μ-barriers, which has rather important implications on the interpretation of the observational data (see §§ 5.2 and 5.3).

Extra mixing is completely characterized by how fast it proceeds and how deep into the star it reaches, that is, by its rate and depth. At this point we want to stress the fact that, unlike all the currently available literature on the subject of abundance anomalies in red giants, the goals of the present work are not to determine combinations of rate and depth of extra mixing that can reproduce the data. Such an empirical way of determining the necessary parameters has been extensively explored already (see references in § 1), and, on the other hand, the computation of rate and depth from first principles is still uncertain. Instead, our goal is to determine if rotational mixing is a viable solution to the problem of abundance anomalies across all types of stars, i.e., those that are observed to be extremely mixed and those observed to be mildly mixed or not mixed at all.

In our models, the extra mixing occurs through the action of rotationally induced hydrodynamic instabilities. According to the timescale in which they act, hydrodynamic instabilities are separated into two classes: dynamical and secular. Dynamical timescales are much shorter than any evolutionary timescale, and therefore dynamical instabilities typically act on a free-fall timescale. Secular instabilities, on the other hand, are related to the local properties of the stellar material and therefore typically act on a Kelvin-Helmholtz timescale or longer.

Because of these different timescales, the transport of angular momentum and chemicals by dynamical and secular instabilities must be treated differently. When a dynamical instability appears, it gets smoothed instantaneously until the particular condition for stability is marginally matched. In the actual star, this is accomplished by mass motions that redistribute the angular momentum as well as mix the material. Hence, if a dynamically unstable region also had a composition gradient, this will be reduced by the same amount as the angular velocity gradient. The only dynamical instability considered in this work is the dynamical shear (Endal & Sofia 1978). Note that, although not related to angular velocity gradients and actually an ingredient of standard models, convection is also a dynamical instability.

Secular instabilities, on the other hand, cannot be instantaneously erased, and the changes in angular velocity and composition are treated as simultaneous (i.e., coupled) diffusion processes in which the diffusion coefficients depend on the timescales, velocities, and path lengths associated with each process. The equations for the rates of change of angular velocity and chemical abundances (X_i) are then

$$\rho r^2 \frac{I}{M}\frac{d\Omega}{dt} = \frac{d}{dr}\left(\rho r^2 \frac{I}{M} D \frac{d\Omega}{dr}\right) \quad (1)$$

and

$$\rho r^2 \frac{dX_i}{dt} = \frac{d}{dr}\left(\rho r^2 D \frac{dX_i}{dr}\right), \quad (2)$$

where I/M is the moment of inertia per unit mass, D is a diffusion coefficient, and the rest of the symbols have their usual meaning. The velocity associated with the diffusion coefficient is the combination of the velocities associated with all the secular instabilities, which in turn depend on the gradients of angular velocity and composition. As a result, D is also a function of these gradients, and equations (1) and (2) must be solved simultaneously.

Our expressions for the diffusion coefficients are taken from published estimates in the literature. We consider three secular mechanisms for mixing: the secular shear, the Goldreich-Schubert-Fricke (GSF) instability, and meridional (Eddington-Sweet) circulation. Because we are neglecting angular momentum redistribution in radiative regions, we only need to solve equation (2) above, with the total diffusion coefficient given by $D = D_{\rm SS} + D_{\rm GSF} + D_{\rm eff}$, where $D_{\rm SS}$, $D_{\rm GSF}$, and $D_{\rm eff}$ are the diffusion coefficients for chemical mixing arising from the secular shear, GSF instability, and meridional circulation, respectively. See the Appendix for the detailed expressions used in this work.

Due to the large structural changes experienced during post-MS stages, instabilities triggered by angular velocity gradients become more important during the RGB than what they were during the MS (Pinsonneault et al. 1989; Chaboyer et al. 1995a). On the upper MS, where angular momentum loss via magnetized winds is negligible (>1.3 $M_\odot$), the most important instabilities are those associated with the absolute rotation (meridional circulation). For solar-mass stars, which experience magnetic braking during their MS lifetime, the relative importance of the different instabilities is not well understood.

Finally, the maximum depth allowed for the action of extra mixing needs to be specified as well. Ideally, if mean molecular weight barriers are the only agents that prevent mixing, the maximum depth for mixing would be obtained internally from the particular profiles of chemical composition, and there should be in principle a dependence of this parameter with stellar mass and metallicity. However, the detailed dependence of the inhibition of mixing by μ-gradients is currently too uncertain and, therefore, we do not intend in this work to explore the variation of the mixing depth with mass and metallicity. Advances in this particular issue are more likely to come from careful analysis of the data, following reasonings similar to that of the study of Charbonnel et al. (1998). See, however, our discussion in § 5.3.

In our models, we set the maximum depth for extra mixing to the location at which 99% of the total stellar luminosity is generated, very close to the top of the HBS. Given that the star's luminosity is generated by hydrogen being turned into helium inside the HBS, parameterizing the mixing depth according to some fraction of the luminosity should actually follow the development of a composition gradient across the HBS and therefore should map at least the form, if not the absolute value, of the inhibition of mixing due to μ-gradients.

In parametric models, the maximum depth is typically parameterized by $\Delta \log T \equiv \log T(M_{\rm core}) - \log T(M_{\rm mix})$, the logarithmic difference between the temperature at the core's surface and that at the mass coordinate of the maximum depth. Denissenkov & VandenBerg (2003) find that $\Delta \log T = 0.19$ best matches both their parametric and rotation-based models of a Population II red giant to the data of field giants. This corresponds to slightly shallower mixing than our chosen depth, and we discuss this in more detail in § 5.4. We only advance here that varying our mixing depth does not change any of our conclusions regarding rotational mixing as a viable explanation of the abundance anomalies in all types of giants.

3.2. *Input Physics*

Using YREC, we investigate the RGB evolution of rotating stars with masses in the range 0.8–2 $M_{\odot}$ for various metallicities. All our RGB runs start at the MS turnoff, which we define as the point where the mass fraction of hydrogen in the star's core reaches 1% (i.e., $X_{\rm core} \approx 0.01$). The starting turnoff models are calculated by evolving the stars, without rotation but allowing for a stellar wind, from a pre-MS, fully convective model on the upper Hayashi track. [Fe/H] metallicities are related to heavy-element fractions by the equation $[{\rm Fe/H}] = \log (Z/X) - \log (Z/X)_{\odot}$. The initial mixtures are computed from a solar mixture with $Y_{\odot} = 0.275$ and $Z_{\odot} = 0.02003$, which are not the values measured for the current Sun but instead account for gravitational settling and diffusion (Grevesse & Sauval 1998; Bahcall et al. 2001). The Galactic enrichment factor $\Delta Y/\Delta Z$ is computed using the above values of $Y_{\odot}$ and $Z_{\odot}$ and a primordial helium fraction consistent with recent observations of extragalactic H II regions, $Y_p = 0.245$ (Izotov & Thuan 2004). The mixing-length parameter is set to 2.085, also taken from the solar models of Bahcall et al. (2001). This value of α is admittedly higher than the typical one used in RGB models, but we verified that the extra-mixing properties of our models are totally insensitive to the choice of this parameter, and its only effect is in the position of the RGB on the color-magnitude diagram (CMD). We use the nuclear reaction rates of Gruzinov & Bahcall (1998), and, currently, YREC evaluates the nuclear burning and mixing independently. This approximation is valid as long as the mixing is much slower than the rate at which the local composition changes appreciably due to nuclear reactions. Given the high temperatures achieved during HBS burning, this approximation should hold during the RGB, although we plan the simultaneous solution of burning and mixing to be implemented in YREC in forthcoming work. The low-temperature opacities of Alexander & Ferguson (1994) are used for $T < 10^4$ K and the OPAL opacities (Iglesias & Rogers 1996) otherwise. Given that the most recent and accurate equations of state (Rogers et al. 1996; Saumon et al. 1995) and atmospheres (Allard & Hauschildt 1995) do not extend to the conditions near the tip of the RGB, we use the Saha equation of state, complemented with the Debye-Huckel correction for Coulomb interactions, and Krishna Swamy atmospheres. We do not consider convective overshoot or semiconvection. Gravitational settling of helium and heavy elements is implemented in the generation of the turnoff models but not considered for the RGB models. Table 1 lists the turnoff age, luminosity, and radius for the stellar masses investigated.

Regarding the ingredients related to rotation, we need to specify an initial angular momentum budget, the angular momentum law in the convective envelope, the details of the transport of angular momentum and composition, and the rate of angular momentum loss. Let us recall at this point that the goal of this paper is to investigate the case with the most favorable conditions for extra mixing due to hydrodynamic processes triggered by internal angular velocity gradients. If the transport of angular momentum by hydrodynamic instabilities is too efficient, these gradients will be rapidly smoothed and extra mixing will consequently be minimal. On the other hand, in the case of inefficient angular momentum transport by these processes, the velocity gradients can survive for longer times, hence maximizing the mixing. Therefore, the best-case scenario for additional mixing will be one in which no angular momentum transport by hydrodynamic processes is allowed, and thus we will only let the angular velocity profile adjust itself to the structural changes during RGB evolution by requiring local conservation of angular momentum (i.e., angular momentum transport will only occur following changes in the structure of the star). Mass loss and stellar winds are not initially considered, but an exploration of their effects under typical conditions produced no appreciable differences. Also, as part of our maximal mixing conditions, we do not impose any inhibition of extra mixing due to composition gradients.

TABLE 1
PROPERTIES OF THE STARTING MODELS (MS TURNOFF)

$M/M_{\odot}$	[Fe/H]	Age (Gyr)	$\log (L/L_{\odot})$	M_V	$R/R_{\odot}$
0.8	−1.0	11.2	0.184	4.41	1.088
0.8	−2.3	10.5	0.484	3.88	1.135
0.85	−1.0	9.00	0.275	4.18	1.154
0.85	−2.3	8.73	0.483	3.68	1.147
0.9	−0.3	10.3	0.108	4.58	1.103
0.9	−0.7	8.07	0.269	4.27	1.171
0.9	−1.4	7.04	0.456	3.76	1.184
1.0	0.0	7.96	0.130	4.58	1.137
1.1	0.0	5.95	0.304	4.13	1.322
1.2	0.0	4.58	0.517	3.58	1.614
1.3	0.0	3.46	0.595	3.38	1.690
1.4	0.0	2.75	0.730	2.90	1.937
1.5	0.0	2.22	0.841	2.82	2.134
1.6	0.0	1.79	0.951	2.46	2.277
1.8	0.0	1.28	1.164	1.91	2.691
2.0	0.0	0.95	1.394	1.30	2.949

NOTES.—Numbers at $X_{\rm core} \approx 0.01$ ("turnoff"). Starting models are standard, i.e., do not include rotation.

At this point, we would like to stress the importance of the choice of initial angular momentum distribution for the final results of rotational mixing during the RGB evolution. Rotational mixing in red giants occurs in the radiative region separating the core and the convective envelope of the star; thus, it is the content and evolution of the angular momentum across this region that determine the amount of extra mixing to be experienced on the RGB. As beautifully illustrated in Figure 32.3 of Kippenhahn & Weigert (1990), the total mass of this radiative zone is actually very small, and at any given time on the giant branch ascent it is comprised of material that is falling from the convective envelope and that is on its way to being burnt inside the HBS and finally deposited on the growing helium core. Thus, the angular momentum contained in the material that is incorporated into the convective envelope during the first dredge-up is the crucial quantity determining the amount of rotational energy that will be available to drive extra mixing.

Such a quantity naturally depends on the angular momentum profile during the MS evolution. Let us consider the two extreme cases of angular momentum distribution typically discussed, namely, solid-body rotation and constant specific angular

momentum, and let us label them case A and case B, respectively. The specific angular momentum (angular momentum per unit mass) of a uniformly rotating spherical shell is $j = dJ/dm = \frac{2}{3}\Omega r^2$, where Ω is the angular velocity and r is the radius of the shell. For a given surface angular velocity Ω_s, the specific angular momentum for case A is $j_{\rm A} = \frac{2}{3}\Omega_s r^2$, while for case B we have $j_{\rm B} = \frac{2}{3}\Omega_s (R/r)^2 r^2$, where R is the total radius of the star. Thus, if $r_{\rm CZ}$ is the radius of the bottom of the CZ at its point of maximum penetration during first dredge-up, then the ratio of the total angular momentum incorporated in the convective envelope for the two cases is

$$\frac{J^{\rm A}_{\rm tot}}{J^{\rm B}_{\rm tot}} = \frac{\int_{r_{\rm CZ}}^{R} (2/3)\Omega_s r^2\, dm}{\int_{r_{\rm CZ}}^{R} (2/3)\Omega_s (R/r)^2 r^2\, dm} = \frac{\int_{r_{\rm CZ}}^{R} r^2\, dm}{\int_{r_{\rm CZ}}^{R} R^2\, dm} < 1. \quad (3)$$

Therefore, the post-MS convective envelope incorporates more angular momentum from an MS progenitor that rotates differentially than from a rigidly rotating one; therefore, case B will experience more mixing than case A. This is the reason behind the conclusion of Denissenkov & VandenBerg (2003) that "the spin-up of the star's core while it is on the MS is needed to get the right extra mixing depth on the upper RGB and thus is very important."

However, the assumption of strong internal differential rotation during the MS goes contrary to the only case of old MS star for which such a measurement is available to us, the Sun, which is a solid-body rotator down to at least 20% of its radius (Tomczyk et al. 1995). Instead, it is at this point safer to assume that turnoff stars in stellar clusters as old as the Sun and older resemble the solar state of rigid rotation. This assumption is, furthermore, in accordance with the current picture of the rotational evolution of solar- and late-type stars, in which the angular momentum distribution in the large majority of old, low-mass MS stars is determined by the coupling of the radiative cores and convective envelopes of the stars through the action of an "interface" magnetic field connecting them, and which is responsible for the extraction of the internal angular momentum via a magnetized wind (Barnes 2003).

Hence, relying on the helioseismic data on the Sun's current state of rotation and the previous discussion, we choose to assign an initial solid-body rotation profile throughout the entire MS turnoff star, such that the rotational velocity at the surface of the star has a value $V_{\rm TO}$, with the corresponding surface angular rotation rate being

$$\Omega_{\rm initial} = 1.4 \times 10^{-5} \left(\frac{V_{\rm TO}}{10\ {\rm km\ s^{-1}}} \right) \left(\frac{R}{R_\odot} \right)^{-1} {\rm rad\ s^{-1}}. \quad (4)$$

Here $R/R_\odot$ is taken from Table 1, and we run models for a wide range of initial (turnoff) rotation rates, $V_{\rm TO}$.

We study the angular momentum evolution for two extreme cases of rotation law ($\Omega \propto r^n$) in convective regions: rigid, solid-body rotation ($n = 0$) and constant specific angular momentum $dJ/dm \equiv J/M$ ($n = -2$), and we show that they lead to very different rotational and mixing histories. As shown in the next section, the key difference between these two cases is that they concentrate the angular momentum content in different regions of the star. If the outer convective envelope of a star rotates as a solid body, then the outer layers, those with large r, will concentrate most of the envelope's angular momentum. If, on the other hand, the convective envelope rotates such that j is a constant (in which case $\Omega \propto r^{-2}$), then the deeper layers of the envelope, those where the mass is mostly concentrated, will be the ones storing most of the angular momentum of the envelope. In other words, the angular momentum content of a star is more centrally concentrated in the case of differential rotation with depth than in the case of solid-body rotation. The assumption of constant j in the envelope also minimizes the loss of angular momentum accompanied by mass loss. Finally, note that, since the lower mass stars considered here ($M \lesssim 1.1\ M_\odot$) have large outer convective envelopes during their MS lifetime, when enforcing a constant J/M law to a convective region at turnoff, the star's angular momentum profile will have a discontinuity at the boundary between the radiative and convective regions due to the assignment of rigid rotation to the initial turnoff model. Although small, this feature will be preserved in our models because, as part of the maximal mixing approach, we will not allow the hydrodynamic instabilities to transport any angular momentum. We come back to this point in more length in § 5.1 when discussing the actual angular momentum profiles and diffusion coefficients.

3.3. *Calibrating Clusters and Sensible Rotation Rates*

We choose the clusters M67 and M92 as representative cases against which we will test our results. These two well-studied clusters, lying on opposite sides of the metallicity scale and with very different turnoff masses, allow for a study of the consequences of rotational mixing under very different conditions. Also, we complement the cluster observations with the data on field giants of Gratton et al. (2000).

Figure 1 shows CMDs of M67 and M92. The M67 CMD was constructed using *BVI* CCD data from Montgomery et al. (1993) and the WEBDA database,[4] while for M92 we use the fiducial (V, $V - I$) CMD given in Johnson & Bolte (1998). The solid lines are standard-model isochrones computed using YREC, with the same input physics as employed in the models with rotation. Identifying the bluest points in the 4 and 14 Gyr isochrones with the turnoff stars in these clusters, we obtain turnoff masses of 1.25 and 0.75 $M_\odot$ for M67 and M92, respectively. The models we use in the next sections for the comparison with the data from these clusters actually have initial masses of 1.3 and 0.85 $M_\odot$. However, this does not represent a problem for our conclusions since, as seen in § 5.4, our results are not too dependent on stellar mass.

We now need to determine the turnoff rotation rates for our models. The rotation velocities of turnoff stars have been measured in M67 (Melo et al. 2001), and the average rotation velocity is low ($\langle v \sin i \rangle = 7\ {\rm km\ s^{-1}}$). However, the current red giants were more massive than the current turnoff stars and would therefore have had higher turnoff rotation velocities. This effect is particularly important for clusters such as M67 with turnoffs in the mid-F star range, where there is a transition (Kraft 1967) from very rapid average rotation to very low average rotation (Fig. 2). In M67 in particular, there is good indirect evidence from two methods that the current giants had a significantly higher average rotation rate than the current turnoff stars.

The first method takes advantage of the fact that the $T_{\rm eff}$–$v \sin i$ relationship is independent of age for spectral types earlier than F8 (Wolff & Simon 1997). Therefore, a much younger cluster like the Hyades (~600 Myr), with the same metallicity as M67, can be used to infer the rotation rates of the progenitors of the current giants in M67. For our M67 turnoff mass of 1.3 $M_\odot$, Hyades analogs with the same $T_{\rm eff}$ have a mean rotation velocity of 30 km s^{-1} (more details in Fig. 2).

[4] See http://obswww.unige.ch/webda.

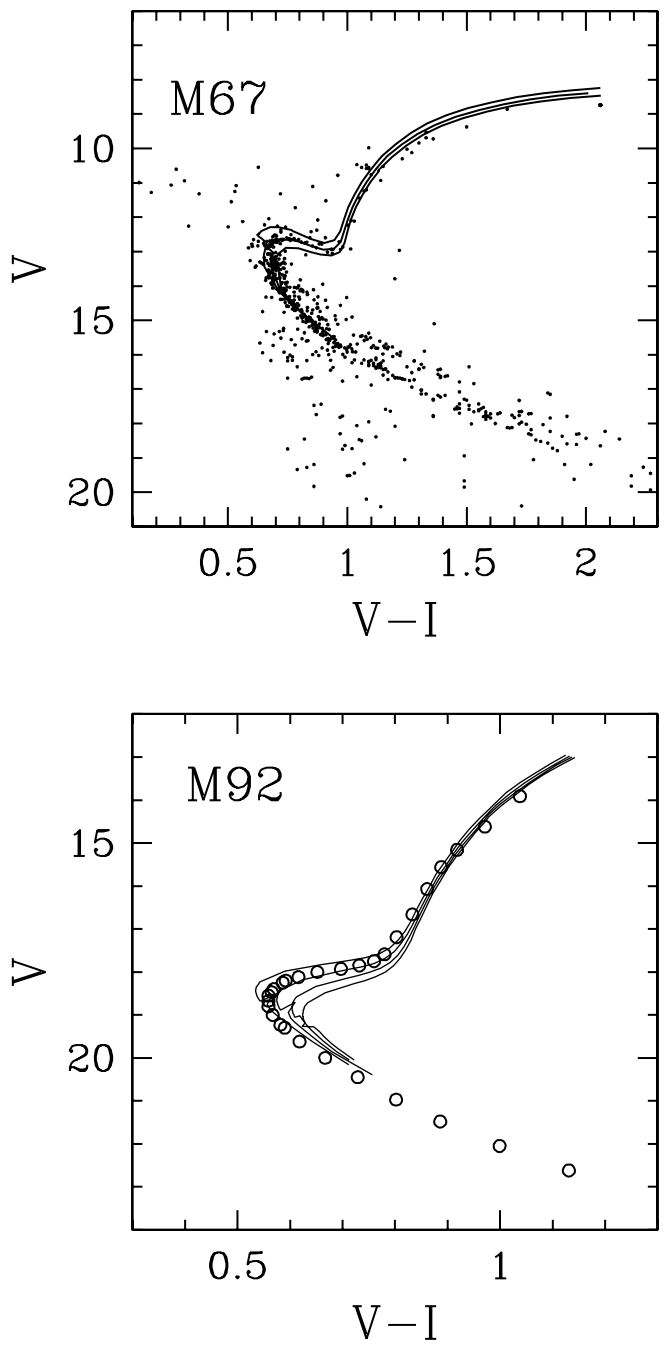

FIG. 1.—CMDs of representative clusters used in the comparison with surface abundance data. Data for M67 are from Montgomery et al. (1993) and the WEBDA database, while for M92 we plot the fiducial CMD given by Johnson & Bolte (1998). The solid lines are theoretical isochrones constructed with the same evolutionary code used in this work, but without rotation. For M67 we show solar-metallicity isochrones for ages of 3, 4, and 5 Gyr, using a distance modulus of $(m - M) = 9.45$ and reddenings of $E(B - V) = 0.04$ (Grocholski & Sarajedini 2003) and $E(V - I) = 1.5E(B - V) = 0.06$. The M92 isochrones are for ages of 12, 14, 16, and 18 Gyr and have a metallicity of [Fe/H] $= -2.3$ and an initial mixture enhanced in α-elements by $[\alpha/\mathrm{Fe}] = +0.3$. Distance modulus and reddening used to shift the M92 isochrones are $(m - M) = 14.60$ and $E(V - I) = 0.013$ (Harris et al. 1997). The transformation to magnitudes and colors was done using the bolometric corrections and color-temperature calibrations of Lejeune et al. (1998).

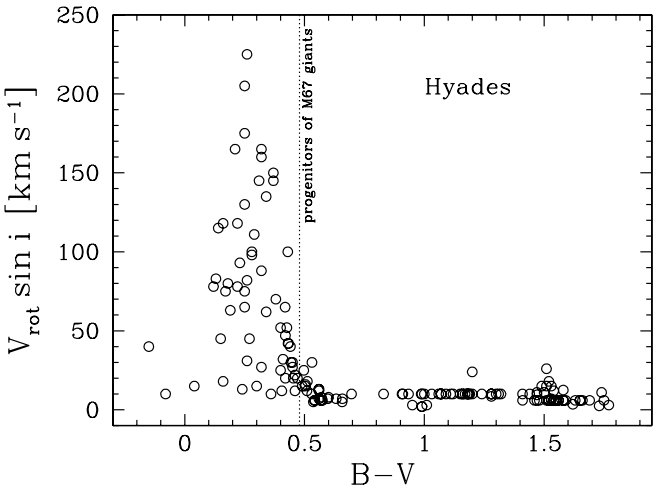

FIG. 2.—Distribution of projected rotational velocities for the Hyades, obtained from the Open Cluster Database (http://cfa-www.harvard.edu/~stauffer/opencl). The steep break in the Kraft curve throughout spectral type F is clearly displayed by the Hyades stars. The vertical dotted line at $B - V = 0.47$ marks the location of a 1.3 $M_\odot$ star of solar metallicity at the age of the Hyades in our models (log $T_{\rm eff} = 3.82$). Such a star, a progenitor of current M67 first-ascent giants, falls right on the region of the diagram where rotational velocities are abruptly decreasing, and it can be seen that appropriate rotational velocities for this star are between 10 and 40 km s^{-1}. See § 3.3.

An independent test is provided by the comparison of lithium data. Boesgaard & Tripicco (1986) discovered the mid-F star lithium dip in the Hyades. Lithium is very efficiently destroyed in stars with a narrow range of effective temperatures; thus, there is a strong correlation between the lithium abundance, $T_{\rm eff}$, and the stellar mass. Balachandran (1995) found that the current red giants at the RGB base in M67 had progenitors in the lithium dip region (see her Figs. 9 and 13). Hyades lithium dip stars have rotation velocities in the 20–40 km s^{-1} range (right on the break of the Hyades Kraft curve), which implies that the current M67 giants had comparable zero-age main-sequence (ZAMS) rotation rates, consistent with the estimates derived above.

The same approach cannot be applied to the case of M92 because there is no younger cluster with measured rotation rates that shares such a low metallicity, while well-studied open clusters such as the Hyades cannot be used here because the relationship between color and surface rotation rate is metallicity dependent. There is, however, some evidence that turnoff stars in globular clusters do not show large rotational velocities. Lucatello & Gratton (2003) find an average projected rotational velocity of 3.1 km s^{-1} for five turnoff stars in the cluster NGC 6397 ([Fe/H] $= -2$), and old field halo stars are observed to have small rotational velocities as well. Hence, it is clear that surface rotation rates larger than, say, 10 km s^{-1} are not observed among old, metal-poor stars.

Having stressed the importance of adopting initial conditions that reflect the observed properties of the different stellar types under study, let us now argue why the generation of models with initial surface rotation rates larger than realistic for any given type of star is actually not a fruitless exercise but, instead, has important advantages. As discussed in § 3.2 and quantified by equation (3), a red giant star whose MS progenitor had a core more rapidly spinning than its envelope experiences much stronger extra mixing than if the progenitor star, like the Sun, rotated rigidly. Since the reason behind this result is that the material incorporated into the convective envelope during the first dredge-up has a much higher angular momentum content when starting from a differentially rotating turnoff star, we can mimic such a

situation but for a rigidly rotating turnoff star simply by starting with an unusually large (for a given type of star) surface rotation rate.

Last but not least, since the diffusion velocities used to model the extra mixing scale as Ω^2, the same results of a rapidly rotating model can be achieved with a slowly rotating one by enhancing the diffusion coefficients associated with extra mixing by the appropriate factor. Therefore, the great utility of generating models that start with unreasonably large rotational velocities is that these are an excellent way to estimate by how large a factor the available theoretical estimates of the diffusion coefficients fail to account for the observations when using sensible initial conditions, and this approach is used extensively in our analysis. Such direct proportionality is only possible in these models because we are not allowing any angular momentum transport due to hydrodynamical instabilities, thus preventing the feedback on the structure due to different degrees of absolute rotation. For these reasons, it is worthwhile to run rotating models with initial surface rotation rates that are too high for the stellar types studied here.

4. RESULTS: THE STRUCTURAL AND ROTATIONAL EVOLUTION

Compared to its effects on the pre-MS and MS on the Hertzsprung-Russell (HR) diagram (Sills et al. 2000), rotation has a small effect on the giant branch tracks. Figure 3 shows post-MS evolutionary tracks for nonrotating and rotating models. The models shown start with a surface rotational velocity of 40 km s^{-1} at turnoff and do not include mass or angular momentum loss. Models with rotation are slightly brighter because of rotationally induced mixing (which we allow to occur regardless of composition gradients) rather than from direct structural effects. The effects of rotation increase at lower masses because of their longer RGB lifetimes. Although not shown here, the choice of angular momentum law in the convective envelope does not have any effect on the HR tracks but leads to quite different mixing histories (§ 5).

Figure 4 shows snapshots of the evolution of the angular velocity and angular momentum profiles as a function of mass and radius, for a star of 1.3 $M_\odot$ and solar metallicity that started with a rotation rate at turnoff of 40 km s^{-1}. The location of these snapshots in the HR track is indicated in Figure 3 by the open squares labeled with a capital character. Solid lines represent the case with constant specific angular momentum in convective regions, and dotted lines show the profiles for solid-body rotation in convective regions.

The structural changes experienced during the giant branch generate a contrast of more than 10^6 between the rotation rates of the core and the surface of the star, a result impossible to achieve during the much longer MS lifetime and also independent of the rotation law assumed for convective regions. As the model ascends the giant branch, its core contracts and spins up considerably, while the envelope expands. At the tip of the giant branch (E), the core rotates more than 100 times faster than at the turnoff (A). At the same time, the model's radius has grown by about a factor of 50 and the surface angular velocity is 4 orders of magnitude smaller, becoming completely undetectable.

The angular velocity profiles in Figure 4 show that almost all the contrast between the rotation at the surface and the core is confined to a narrow region in mass coordinate that coincides with the radiative zone between the core and the base of the convective envelope. This is crucial because angular velocity gradients can generate extra mixing.

Initially (stage A), all the profiles are nearly equal to the initial solid-body rotation throughout the star. There is little change

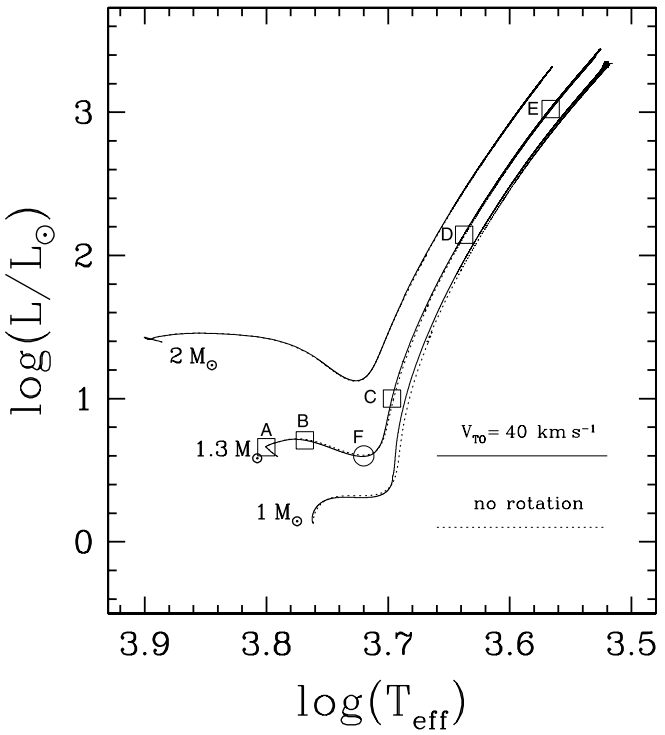

FIG. 3.—Evolutionary tracks for stars with masses of 1.0, 1.3, and 2.0 $M_\odot$ and solar metallicity, from the main-sequence turnoff and up to the tip of the giant branch. Dotted lines represent standard, nonrotating models, and solid lines are models that started with a rotational velocity of 40 km s^{-1} at the main-sequence turnoff. The open squares along the track for the 1.3 $M_\odot$ star represent the locations of the snapshots chosen to illustrate the rotational evolution and shown in Fig. 4. The open circle labeled F marks the location of the bottom of the RGB.

during the transition from core to shell hydrogen burning (the SGB, panels B). At C, on the giant branch but before the LF bump, the convective envelope has reached its maximum depth in both mass and radius. Thereafter, its base slowly retreats in mass, while staying at the same location inside the star (see the position of the arrows from panels C to E). In the case of solid-body rotation (*dotted lines*), while the angular velocity stays constant, J/M increases as r^2.

For constant specific angular momentum in the convective envelope (*solid lines*), there is a discontinuity in the angular velocity and angular momentum profiles that, only at the very beginning, is a consequence of our choice of initial conditions, appearing when a differentially rotating convective envelope encounters a rigidly rotating interior.

Later, however, the angular momentum being incorporated into the deepening envelope is redistributed such that J/M is constant across the envelope. This effectively spins up the deep layers immediately above the base of the convective envelope, therefore creating what is now a large discontinuity in the angular momentum profiles. We emphasize that the latter effect is real and has nothing to do with the initial (small) discontinuity introduced by the initial configuration of angular momentum at the turnoff. Furthermore, this discontinuity does not get smoothed in our models because we are not allowing any transport of angular momentum as an ingredient of the maximal mixing scenario; we come back to this point in § 5.1.

In the case of constant specific angular momentum and after the end of the first dredge-up, the material that was part of the (now) retreating convective envelope and now is falling into the radiative regions remains with constant J/M and an r^{-2} angular velocity profile (regions at the left of the arrows in panels D

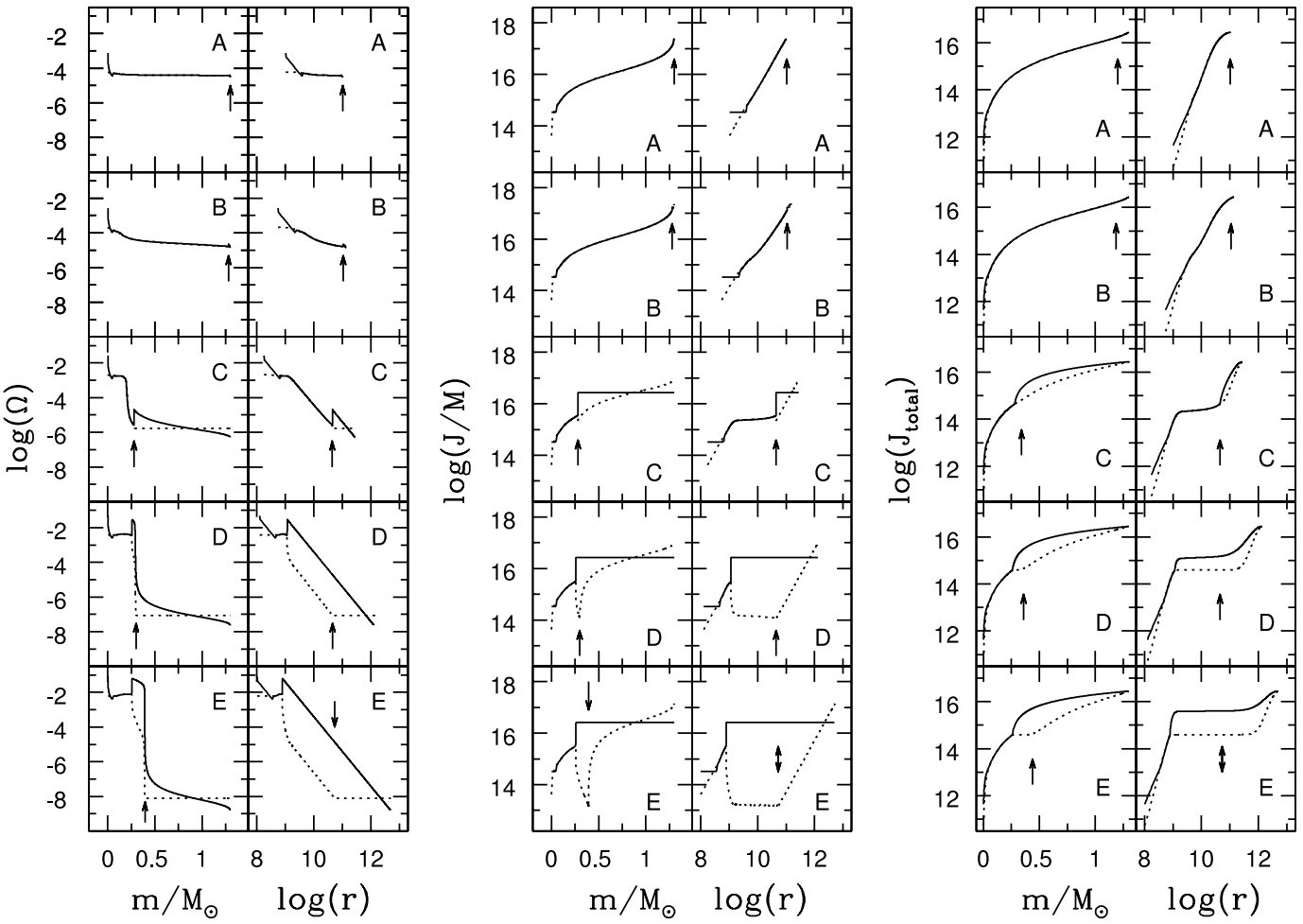

FIG. 4.—Evolution of the profiles of angular velocity (Ω), specific angular momentum ($dJ/dm \equiv J/M$), and total angular momentum ($J_{\rm total}$), as a function of mass and radius (cm), for a star of 1.3 $M_\odot$ and solar metallicity that started with a rotational velocity of 40 km s^{-1} at turnoff. Each snapshot is labeled by a capital character (A, B, C, D, and E) that indicates its location on the evolutionary track shown in Fig. 3. Solid lines represent constant specific angular momentum in the convective envelope, and dotted lines represent solid-body rotation. The location of the base of the outer convection zone is indicated with arrows.

and E). As a result, the star stores much of its angular momentum in its radiative interior, retaining a large angular velocity gradient. In the presence of efficient angular momentum transport, this gradient would be smoothed by hydrodynamical instabilities. Therefore, our assumptions of large differential rotation in the envelope and suppression of angular momentum transport by hydrodynamic instabilities result in a case where rotational mixing is maximized.

As Sills & Pinsonneault (2000) found, the fast observed rotation rates of HB stars imply that red giants retain most of their MS angular momentum, even after the mass loss experienced at the top of the RGB. If the star were effective in distributing its internal angular momentum to the envelope (which would be the case if angular momentum transport were effective in smoothing internal gradients), then mass-loss episodes would be accompanied by significant loss of angular momentum, and HB stars would rotate slowly.

This result is illustrated by Figure 4, where it can be seen that the solid-body profiles in the inner radiative region get progressively lower relative to the constant J/M profiles. This implies that, for the rigidly rotating case, angular momentum from the interior is being deposited in the outer regions. Simple arguments explain this effect. For stars with rigidly rotating convective envelopes, the ratio of specific angular momentum at the surface to that at the base of the convection zone scales as $(R/r_{\rm CZ})^2$, where R is the radius of the star and $r_{\rm CZ}$ is the position of the base of the convection zone. As the star expands, R gets larger but $r_{\rm CZ}$ remains constant, and the surface's specific angular momentum increases. Since there are no external sources of angular momentum, this happens at the expense of angular momentum from the interior, which is therefore redistributed within the surface convection zone. The opposite effect occurs for the case with constant J/M, which concentrates most of the angular momentum content where the bulk of the mass lies and, as the model star expands, the interior spins up with respect to the outer layers.

5. RESULTS: THE PHYSICS OF MIXING

An internal mixing episode other than the standard first dredge-up is now recognized to occur in first-ascent giants. One of its main characteristics is a strong dependence with spectral type: while the more massive (early type) giants in open clusters show mild levels of extra mixing (Gilroy 1989), the oldest (late type) giants in globular clusters experience stronger and deeper extra mixing, typically displaying abundance patterns characteristic of material in nuclear equilibrium.

Still, theoretical investigations on the subject have dealt almost exclusively with the lowest mass, most metal-poor end of the spectrum, i.e., Population II giants (in the field and globular clusters) with progenitor masses between 0.8 and 0.9 $M_\odot$.

Furthermore, such nonstandard mixing is widely assumed to work only once the μ-barrier left after first dredge-up has been erased by the advancing HBS and thus would only affect stars on the upper RGB.

This "canonical" extra mixing, to use a term coined recently by Denissenkov & VandenBerg (2003), is mostly believed to be associated with rotational effects (Sweigart & Mengel 1979; Charbonnel 1995; Denissenkov & VandenBerg 2003) that must be deep enough to have an effect on the surface abundances of the CNO elements but cannot be responsible for the anomalies involving heavier species like Na, Mg, and Al.

A rapid summary follows of the overall features of our models, which involve several differences with all previous theoretical studies of this subject. Then, in §§ 5.1–5.4 we use rotating models for M67 giants (Figs. 4–9) to discuss in detail the physics of rotational mixing and the results from our models.

We have a standard first dredge-up very similar to that of all other works on the subject. Post–dredge-up abundance ratios can be significantly altered only at high rotational velocities, due to deep meridional mixing arising as a consequence of the significant departure from spherical symmetry. However, when exploring the impact of differences in the initial composition from cluster to cluster, we obtain that the post–first dredge-up abundance ratios, particularly that of $^{12}C/^{13}C$ (which has always been assumed to start at the solar system value), depend significantly on the adopted initial mixture.

While all previous theoretical studies have assumed that extra mixing is only possible beyond the RGB bump, a generic result of all our models is that rotational mixing, although present in small amounts, is anyway inefficient on the lower RGB independently of any inhibiting effect of μ-barriers. Therefore, the lack of well-mixed stars before the luminosity of the RGB bump in the field and globular clusters (§§ 1 and 6) should not be interpreted as evidence for the inhibition of mixing by μ-barriers.

Furthermore, our models, with no transport of angular momentum allowed in radiative regions, actually erase the μ-barrier left by the deepening of the convective envelope even at very small rotation rates. This fact, rather than the absence of mixed stars before the RGB bump, is what really constitutes evidence that μ-barriers may actually inhibit mixing.

On the upper RGB, only models with differentially rotating (constant J/M) convective envelopes experience canonical extra mixing, consistent with the early predictions of Sweigart & Mengel (1979), although for reasons other than the disappearance of the μ-barrier (§ 5.1). The amount of extra mixing is a strong function of rotation rate and shows a weaker dependence on metallicity. On this evolutionary stage, our work presents two main departures from that of previous investigators. First, canonical extra mixing does indeed start at the approximate location of the RGB bump, but, rather than being due to the disappearance of the μ-barrier, it occurs as a consequence of simple angular momentum considerations that, not surprisingly, are intimately related to the requirement of having differential rotation in the envelope (§ 5.1). Second, we simultaneously treat both the Population I and Population II regimes using the same models and adopting initial rotation rates in accordance with data as a function of stellar type. This comprehensive approach has led us to new insights on the problem of the interaction between rotation and convection in the envelopes of stars (§ 6.4).

Mass-loss rates typical of red giants in globular clusters ($\Delta M \sim 0.1$–$0.15\ M_\odot$), since important only close to the tip of the RGB, produce almost negligible effects in the surface abundance ratios of the most luminous giants. For extreme mass-loss rates, however, larger differences might be possible.

5.1. *Mixing and the Angular Momentum Distribution in the Convective Envelope*

Different assumptions about the distribution of angular momentum result in different amounts of rotationally induced mixing. The mode of rotational mixing related to differential rotation is that associated with hydrodynamical instabilities, in contrast with rotational mixing associated with departures from spherical symmetry (§ 5.2), which depends on whether rotation is fast or slow.

The impact that different angular momentum profiles in the convective envelope have on the core's rotation is well illustrated in Figure 4, where, even though both cases of angular momentum law in the convective envelope start with almost the same angular momentum budget (A), at the RGB tip (E) the case of constant J/M has a specific angular momentum and a rotation rate at the base of the convective envelope that are about 2 orders of magnitude larger than those of the case with a rigidly rotating envelope. In both cases, the material falling from the convective envelope keeps its angular momentum content (due to local angular momentum conservation), but the key difference is that the material that had constant J/M while being part of the convective envelope is spinning at a much higher rate (material immediately to the left of the arrows in the radial profiles in panels D of Fig. 4). This occurs because the assumption of a constant J/M in the convective envelope during the SGB and lower RGB effectively redistributes the envelope's angular momentum content such that most of it is stored in the deeper layers, therefore spinning up those immediately above its base. Comparison of the mass profiles of the specific angular momentum J/M in panels A and C in Figure 4 clearly illustrates this phenomenon. Hence, hydrodynamical instabilities are triggered in both cases of angular momentum distribution in the convective envelope, but the constant J/M case will experience mixing velocities more than 10^4 times larger ($D \propto \Omega^2$) than those of the case with solid-body rotation. This is a solid result of all models of rotational mixing since the work of Sweigart & Mengel (1979) and constitutes the ultimate reason for the departure of the extra mixing experienced by the two cases of rotation law in the convective envelope (see also discussion of Fig. 6 below).

Figure 5 shows the evolution of the radial profiles of angular velocity, composition gradient, and the diffusion coefficient associated with the extra mixing for a $1.3\ M_\odot$ star of solar metallicity (our M67-like case). Only the case capable of extra mixing, i.e., that with constant specific angular momentum in the convective envelope, is shown. The top panels include some of the snapshots of angular velocity profile also appearing in Figure 4 (labeled B, C, and E), along with others chosen because of their relevance to the present discussion, and again illustrate the building of a large angular velocity gradient soon after the MS turnoff. The location of the convective envelope is indicated with an arrow in each panel. Note that, while the star is progressively expanding, the base of the convective envelope remains almost at the same physical position, $10.5 \lesssim \log r \lesssim 11$, even though it is at the same time incorporating an increasingly larger fraction of the star's total mass until the first dredge-up finishes around point C (see also the mass profiles in Fig. 4).

Until point C in Figure 5, the location of the arrow coincides with a jump or step in the angular velocity profile already noticed in § 4 and that, rather than being an artifact of our choice of initial conditions, is instead a physical phenomenon that is fundamental to our picture of rotational mixing. This jump corresponds to the same discontinuity present in the specific angular momentum profiles of Figure 4 for the case of constant J/M in the convective envelope and is the natural consequence of three factors.

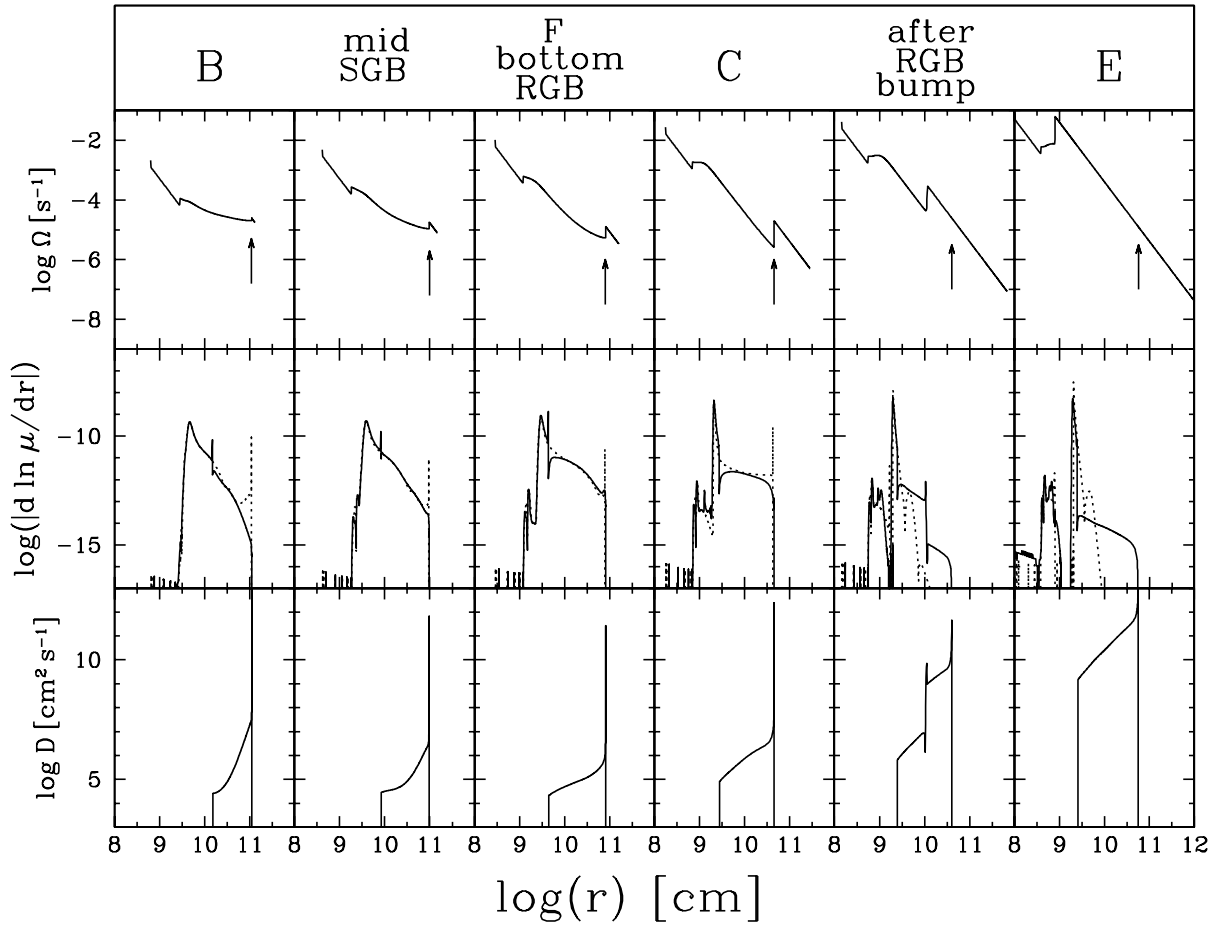

FIG. 5.—Radial profiles of angular velocity, gradient of mean molecular weight, and the diffusion coefficient associated with extra mixing at six different points in the post-MS evolution for a rotating model of a 1.3 $M_{\odot}$ star of solar metallicity that started with a rotational velocity of 40 km s^{-1} at turnoff. The B, C, E, and F labels refer to the locations shown on the evolutionary track of Fig. 3. The base of the convective envelope at each snapshot is indicated by arrows. The dotted lines in the μ-gradient panels represent the standard model profiles.

First, the condition of constant specific angular momentum in the convective envelope ensures that the angular momentum content of the material incorporated into the envelope during the deepening of the convection zone is redistributed such that most of it is stored in the deepest layers of the envelope, that is, where most of the mass lies. We further assume local conservation of angular momentum in the radiative region, which means that nothing happens to the angular momentum profile of the region below the point of maximum depth of the convection zone. Finally, the absence of any transport of angular momentum in regions of strong angular velocity gradients also effectively decouples the rapidly spinning base of the convective envelope from the slowly rotating radiative core. If, on the other hand, there was effective angular momentum transport in differentially rotating regions, then this discontinuity would tend to be smoothed. However, we argue that the real situation could actually closely resemble that depicted here because μ-barriers may have the effect of suppressing circulation and inhibiting extra mixing. If such were the case, angular momentum transport by hydrodynamic means would also be suppressed, and a discontinuity in the angular momentum distribution similar to that seen in our models should appear.

The middle panels of Figure 5 show the evolution of the gradient of chemical composition from the SGB to the tip of the RGB for the rotating model of a 1.3 $M_{\odot}$ star of solar metallicity. The sharp edge of the profiles at large radii marks the base of the convective envelope, where composition gradients vanish. Note also the evolution of the HBS, slightly broad past the MS turnoff in panel B, and progressively narrowing thereafter. Similar to the base of the convective envelope, the physical location of the HBS remains approximately constant (its peak always around $\log r \approx 9.5$), as hydrogen-rich material falls from the convective envelope and is afterward deposited in the growing core of the star.

In the bottom panels of Figure 5 we show the evolution of the diffusion coefficient associated with rotational mixing. Note that the profiles are always confined by the outer edge of the HBS on the inner side (more exactly, where the luminosity reaches 99% of the total luminosity; see § 3.1) and the base of the convective envelope on the outer side. Inspection of panels B through C (SGB and lower RGB) provides a clear demonstration of the direct proportionality between the diffusion coefficient, i.e., the strength of extra mixing, and the total luminosity of the star (as is expressed in eq. [5]). On the one hand, since the locations of the HBS and the base of the envelope remain approximately the same and, furthermore, local angular momentum is conserved, this radiative region does not experience major structural changes across these evolutionary stages. On the other hand, the luminosity does change by a factor of $\sim$2.5 from B to C, experiencing a local minimum at an intermediate location (marked as F in Fig. 3), and one can verify in the bottom panels of Figure 5 that the diffusion coefficient simultaneously experiences the same minimum.

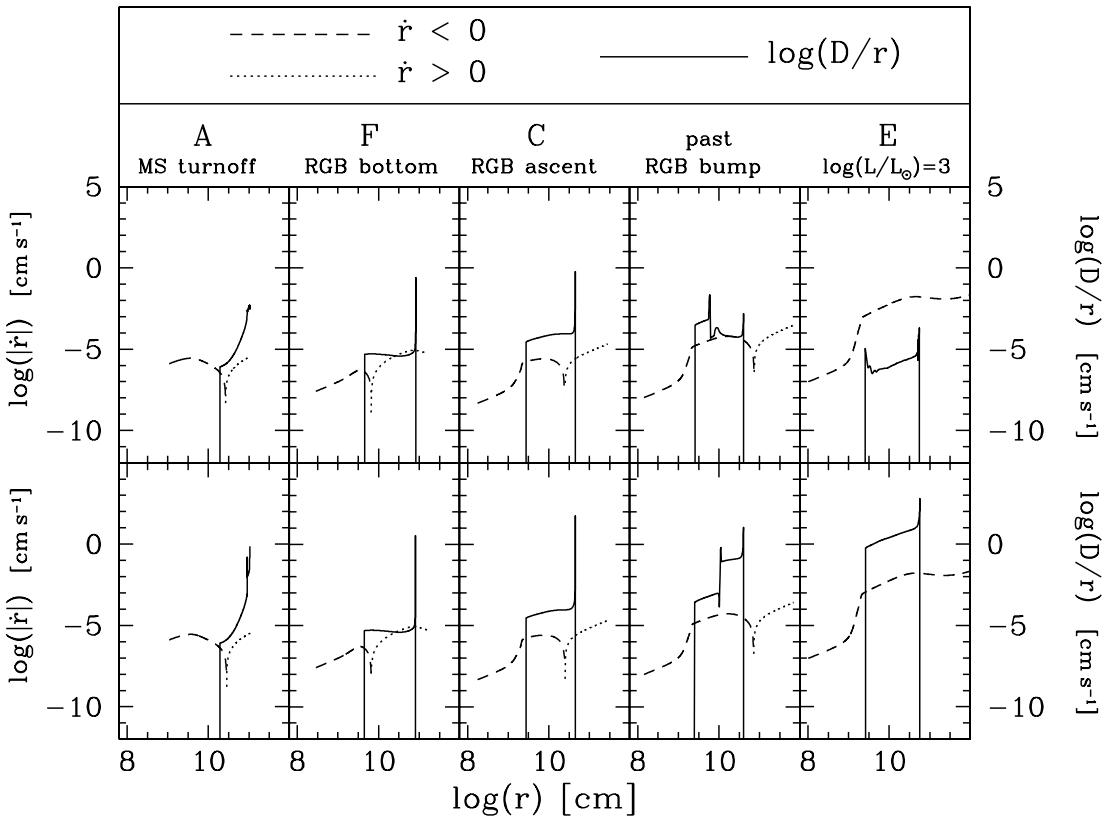

FIG. 6.—Diffusion velocities of extra mixing against the instantaneous velocity field of matter inside a star of 1.3 $M_{\odot}$ and solar metallicity from the MS turnoff to close to the RGB tip. The A, C, E, and F labels refer to the locations shown on the evolutionary track of Fig. 3. Dashed lines represent infalling velocities, dotted lines represent regions in expansion, and the solid line is an order-of-magnitude estimate of the velocity at which extra mixing proceeds in our models. The top panels correspond to the case of solid-body rotation in the convective envelope, and the bottom panels to a constant specific angular momentum distribution in the envelope. Giants with any of the angular momentum laws in the convective envelope behave identically until the location of the RGB bump, after which only the case with a differentially rotating envelope achieves diffusion velocities larger than the velocity at which the material falls from the convective envelope, and thus this is the case able to affect the surface abundances.

The rapid structural evolution of red giants makes rotational mixing a threshold process. To be reflected in the surface abundances, rotational mixing must overcome the infalling velocity field inherent to the region of the red giant where it occurs. In Figure 6 we show, for our M67-like giant, both the instantaneous velocity field of the material inside the star and a first-order estimate of the diffusion velocity of extra mixing, for various evolutionary stages from the MS turnoff to close to the tip of the RGB. The dashed lines represent infalling material ($\dot{r} < 0$), the dotted lines represent material moving outward ($\dot{r} > 0$), and the solid line is our estimate of the velocity of extra mixing. The top panels shows the case of a model with a rigidly rotating convective envelope. No extra mixing is experienced by this model, and the diffusion velocities are always smaller than those associated with the structural changes (either infall or expansion) all the way from the MS turnoff (panel A) to the tip of the RGB (past panel E). For models with differentially rotating envelopes (*bottom panels*), the opposite occurs, and mixing eventually overcomes the infalling velocity field.

As demonstrated by Figures 5 and 6, our scenario contemplates extra mixing at all evolutionary stages immediately past the MS turnoff, including the SGB and the lower RGB. At the same time it reproduces the observed lack of well-mixed stars before the location of the RGB bump as a natural consequence of the still small amount of energy available to drive rotational mixing during those early stages (eq. [5]), i.e., for reasons different than so far claimed in the literature (Charbonnel et al. 1998; Denissenkov & VandenBerg 2003).

Finally, we have also shown that the key ingredient for driving efficient extra mixing on the upper RGB is the angular momentum content of the material falling from the convective envelope into the radiative region above the HBS. The conclusion that the μ-barrier is not the agent preventing the extra mixing is evidenced by the fact that our models with solid-body rotation in the convective envelope are not able to mix even after the μ-barrier has already been erased by the advancing HBS (§§ 5.2 and 5.4).

Once again, we stress that this constitutes a crucial theoretical departure from all previous models of extra mixing in red giants: in our models, canonical extra mixing becomes a vigorous process only at the location of the RGB bump, not necessarily because a steep μ-barrier inhibits the mixing of chemicals to occur earlier in the RGB evolution (which it may or may not be able to do), but, more fundamentally, because a steep μ-barrier would also inhibit the transport of angular momentum between the rapidly rotating base of the convective envelope and the radiative region, thus creating the appropriate conditions of angular momentum distribution that permit extra mixing to occur.

5.2. *Mixing on the SGB and Lower RGB*

Figure 7 shows selected internal abundance profiles for a 1.3 $M_{\odot}$ model of solar metallicity (M67-like case) located on the SGB (point B in Fig. 3), where the top panel corresponds to a standard model and the bottom panel to a rotating model. In contrast to the standard case, the small amount of extra mixing during the early post-MS stages in the rotating models has the

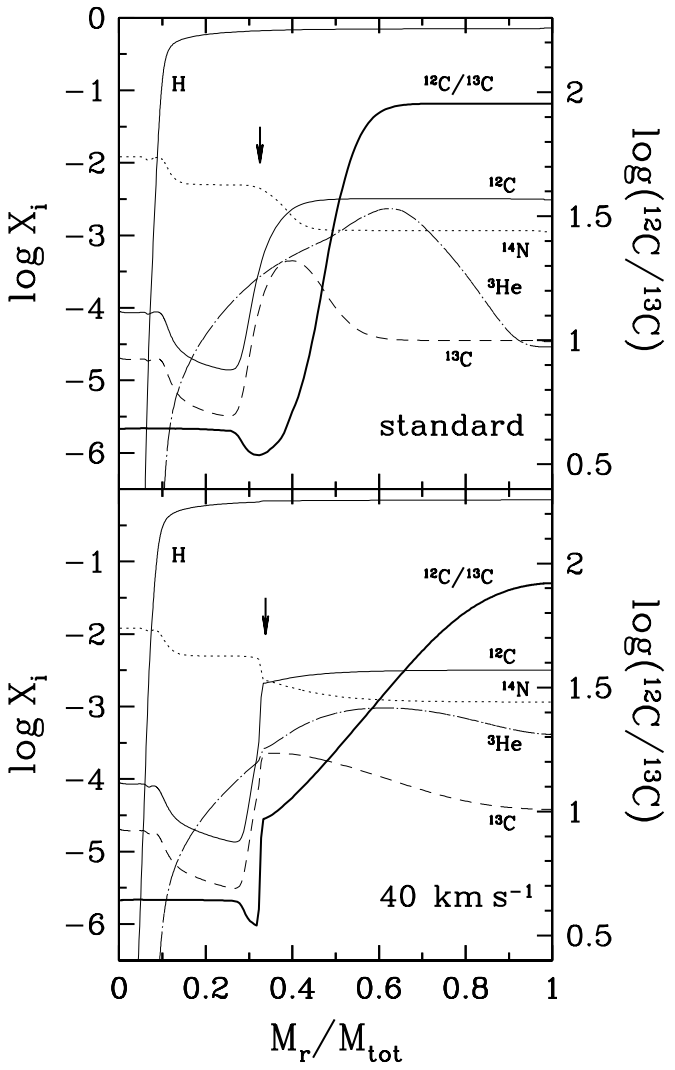

FIG. 7.—Internal composition profiles of some relevant species, as well as the $^{12}C/^{13}C$ ratio, for a 1.3 $M_\odot$ star of solar metallicity on the SGB [marked as B in Fig. 3, i.e., $\log(L/L_\odot) \sim 0.7$]. The top panel shows a standard model, and the bottom panel is a rotating model that started with a rotational velocity of 40 km s^{-1} at turnoff. The arrows indicate the location of the base of the convective envelope at its point of maximum depth during the first dredge-up. Comparison of both panels clearly reveals the smoothing effect of the extra mixing on the abundance profiles, which produces the slight difference of the surface $^{12}C/^{13}C$ ratio between the standard and the rotating cases even before the onset of the first dredge-up.

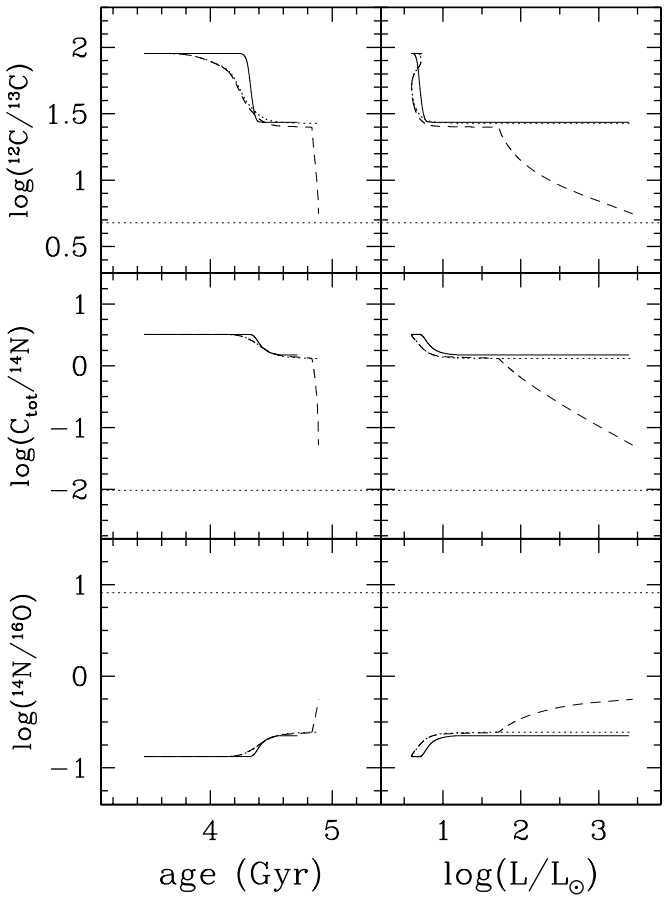

FIG. 8.—Surface ratios of the carbon isotopes, carbon to nitrogen, and nitrogen to oxygen, for the case of a 1.3 $M_\odot$ star of solar metallicity, as a function of age and luminosity since the MS turnoff. Solid lines correspond to the standard model, i.e., without any rotation. The other two lines represent rotating models that started with a rotational velocity of 40 km s^{-1} at turnoff, for the two different rotation laws in convective regions studied: solid body (*dotted lines*) and constant specific angular momentum (*dashed lines*).

effect of flattening the internal profiles but, with the exception of ^{3}He, has little impact on the abundances at the surface. Indicated with arrows is the location of the base of the convection zone at its point of maximum penetration during the first dredge-up ($M_r/M_{\rm tot} \approx 0.34$). The discontinuity in all the composition profiles of the rotating model (*bottom panel*) is artificial and is due to the maximum depth allowed for extra mixing to occur in our models (approximately the outermost edge of the HBS).

The evolution of the surface $^{12}C/^{13}C$ ratio, as well as that of carbon to nitrogen and nitrogen to oxygen, is shown in Figure 8, for both standard (*solid lines*) and rotating (*broken lines*) models of a 1.3 $M_\odot$ star of solar metallicity. In the standard model, the changes in surface abundance ratios only occur during the first dredge-up and take place early in the ascent up the giant branch [almost completely done at $\log(L/L_\odot) \sim 1$; *right panels*]. By the end of the first dredge-up, the top panels show that the carbon isotope ratio $^{12}C/^{13}C$ has dropped from the initial (solar) value of $\sim$100 to $\sim$25. As one moves to ratios that are more temperature sensitive, the dredge-up effects decrease, and one can see in the middle and bottom panels the characteristic overall net conversion of carbon and oxygen into nitrogen, typical of CNO processing.

The broken lines in all panels of Figure 8 represent the two extreme cases of angular velocity law in the convective envelope: dotted lines correspond to rigid, solid-body rotation, while dashed lines correspond to constant specific angular momentum J/M. All rotating models started at the MS turnoff with a rotational velocity of 40 km s^{-1}, which lies at the high end of the range of rotation rates shown by the precursors of this type of star (Fig. 2 and discussion in § 3.3). In the rotating models, the changes start even before the first dredge-up takes place in the standard models. This is the result of subsurface changes in the composition profile of our models in early post-MS stages driven by the departure from spherical symmetry.

However, rotation does not significantly affect the post–first dredge-up ratios, regardless of the angular momentum law in the convective envelope. Then, after dredge-up, the abundance ratios in the two rotating models remain constant throughout the entire lower RGB, a general result of our models without invoking any inhibiting effect from μ-barriers.

The fact that extra mixing, although present in small amounts, is inefficient on the SGB and lower RGB is not surprising when

one considers that the energy ϵ available to drive circulation can be expressed as a fraction of the total luminosity,

$$\epsilon \approx \chi L \approx \left(\frac{\Omega^2 r}{g}\right)_{\rm eq} L, \quad (5)$$

with χ usually expressed as the ratio between the centrifugal acceleration and that of gravity at the equator, thus measuring the departure from spherical symmetry. While the fraction χ does not change much all along the RGB, the star's luminosity during the SGB and the lower RGB is 1 or 2 orders of magnitude smaller than during the upper RGB, and thus rotational mixing is correspondingly inefficient in these early post-MS stages. Note that this happens independently of any inhibiting effect of μ-barriers: while most investigations suppress mixing on the lower RGB because of the existence of a strong μ-barrier, we do not enforce such suppression and obtain that our lower RGB models exhibit minimal mixing anyway.

Even though the globular clusters, particularly the data on the carbon isotopes (§ 6.3), seem to show strongly mixed stars only in the upper RGB and not before, this should not be taken as confirmation that extra mixing "only" occurs after the RGB bump, nor as evidence for any inhibiting effect of μ-barriers. Instead, if one were to follow equation (5), the lack of well-mixed stars on the SGB and the lower RGB is a natural consequence of the small amount of energy available to perform mixing, given that the luminosity of the star is still too low in comparison to its luminosity once on the upper RGB. Thus, it seems more appropriate to talk about inefficient, albeit present, extra mixing on the lower RGB, rather than extra mixing occurring only on the upper RGB (we also refer the reader to the discussion of Figs. 5 and 6 in § 5.1).

Even in our most mixed models, the vigorous extra mixing only kicks in when the star is on the upper RGB, and this rather abrupt transition happens approximately at the expected location of the RGB bump. The important difference is, however, that since we have not considered any inhibiting effect of composition gradients in the models, the disappearance of the μ-barrier when the HBS crosses it is not the reason behind the onset of the strong mixing at that particular point in the evolution. Instead, as discussed in § 5.1, what really matters is the angular momentum content of the material falling from the retracting (in mass coordinate) convective envelope into the radiative interior above the HBS, where the extra mixing is at work.

Therefore, rotational mixing before and after the RGB bump may be thought of as the difference between the two modes of mixing provided by rotation. In the absence of any inhibition by μ-barriers, rotational mixing is active at any time on the RGB in the form of meridional circulation driven by the departure from spherical symmetry (eq. [5]). On the other hand, rotational mixing associated with strong differential rotation only becomes important when the right conditions of angular momentum content are matched (§ 5.1), which in our models occurs at the approximate location of the RGB bump.

5.3. *The RGB Bump and the Effect of μ-Barriers*

In § 5.2 we showed that the CNO abundances previous to the location of the RGB bump are not sensitive to whether mixing is inhibited or not by μ-barriers, and therefore they should not be taken as evidence for such inhibition. However, here we find that it is another indicator, the very existence of the RGB bump itself, the one that indeed provides sound evidence for inhibition of mixing by μ-barriers.

Our models, with no inhibition of mixing by μ-barriers, erase the discontinuity in the hydrogen profile that gives rise to the standard μ-barrier, and this happens even for very slow rotation rates. Figure 9 shows the evolution of the gradient of chemical composition from the MS turnoff to the tip of the RGB, for both a standard model (*left panels*) and a rotating model (*right panels*) of a 1.3 $M_\odot$ star of solar metallicity with a turnoff rotation rate of 40 km s^{-1}. Each of the upper three pairs of panels shows the profile of μ-gradient at four closely consecutive evolutionary stages located at the SGB, the lower RGB, and the upper RGB, as indicated by the labels at the right. The order of the profiles in each panel is, with increasing evolutionary state (age), dot-dashed lines, dashed lines, solid lines, and finally dotted lines. The last profile on each pair of panels is then plotted again as the first one on the panel immediately below.

The first peaks on the left edges of the profiles in Figure 9, very broad close to the turnoff and rapidly narrowing with advancing evolutionary state, correspond to the HBS. The growth of the convective envelope, which starts during the SGB and continues to the lower RGB, can be followed by tracking the motion of the right edge of the profiles of μ-gradient in the upper two pairs of panels. Below, the pair of panels corresponding to the upper RGB show how the extremely narrow HBS gradually advances with increasing luminosity, depositing the ashes of hydrogen burning into the growing helium core. Note that all the sharp edges of the profiles of μ-gradient in the standard case are smoothed by extra mixing in the rotating models.

The bottom pair of panels in Figure 9 show the μ-gradient profiles near the location of the RGB bump. Note, in the standard model case (*left panel*), the sharp right edge of the μ-gradient profiles, located at $M/M_\odot \approx 0.28$ for the dashed line (point C in Fig. 3) and $M/M_\odot \approx 0.248$ for the solid line [just before the occurrence of the RGB bump; $\log (L/L_\odot) \sim 1.6$]: they correspond to the standard μ-barrier, created by the base of the convective envelope as it penetrates during the first dredge-up. The locations of these two lines differ because at point C [$\log (L/L_\odot) = 1$] the first dredge-up has not ended yet and the base of the convective envelope is still deepening in mass. The model just after the RGB bump is represented by the dotted line in the bottom pair of panels. In the standard case (*left panel*) the μ-barrier does not exist anymore, since it was erased by the pass of the HBS (now being the highest peak of the dotted line) through that location.

On the other hand, in the rotating case, the μ-barrier is almost entirely erased by the action of mixing well before the location of the bump. Given that the RGB bump is a real feature already seen in the CMDs and LFs of various Galactic and extragalactic systems, it is clear that stellar models should not get rid of μ-barriers as easily as ours.

Therefore, our results actually provide the first convincing evidence that μ-barriers must indeed inhibit mixing across them, since otherwise the RGB bump would easily disappear. Note the large qualitative departure of this claim from those of all previous works on the subject, which mistakenly identified the lack of well-mixed stars on the lower RGB as evidence for the inhibiting effect of μ-barriers.

5.4. *Upper RGB: Canonical Extra Mixing*

Differential rotation provides an additional mixing mechanism that becomes important only on the upper RGB, and different assumptions on the distribution of angular momentum in the convective envelope result in different amounts of rotationally induced mixing (§ 5.1).

Figure 8 shows that after first dredge-up the abundance ratios remain constant for both cases of angular velocity distribution in

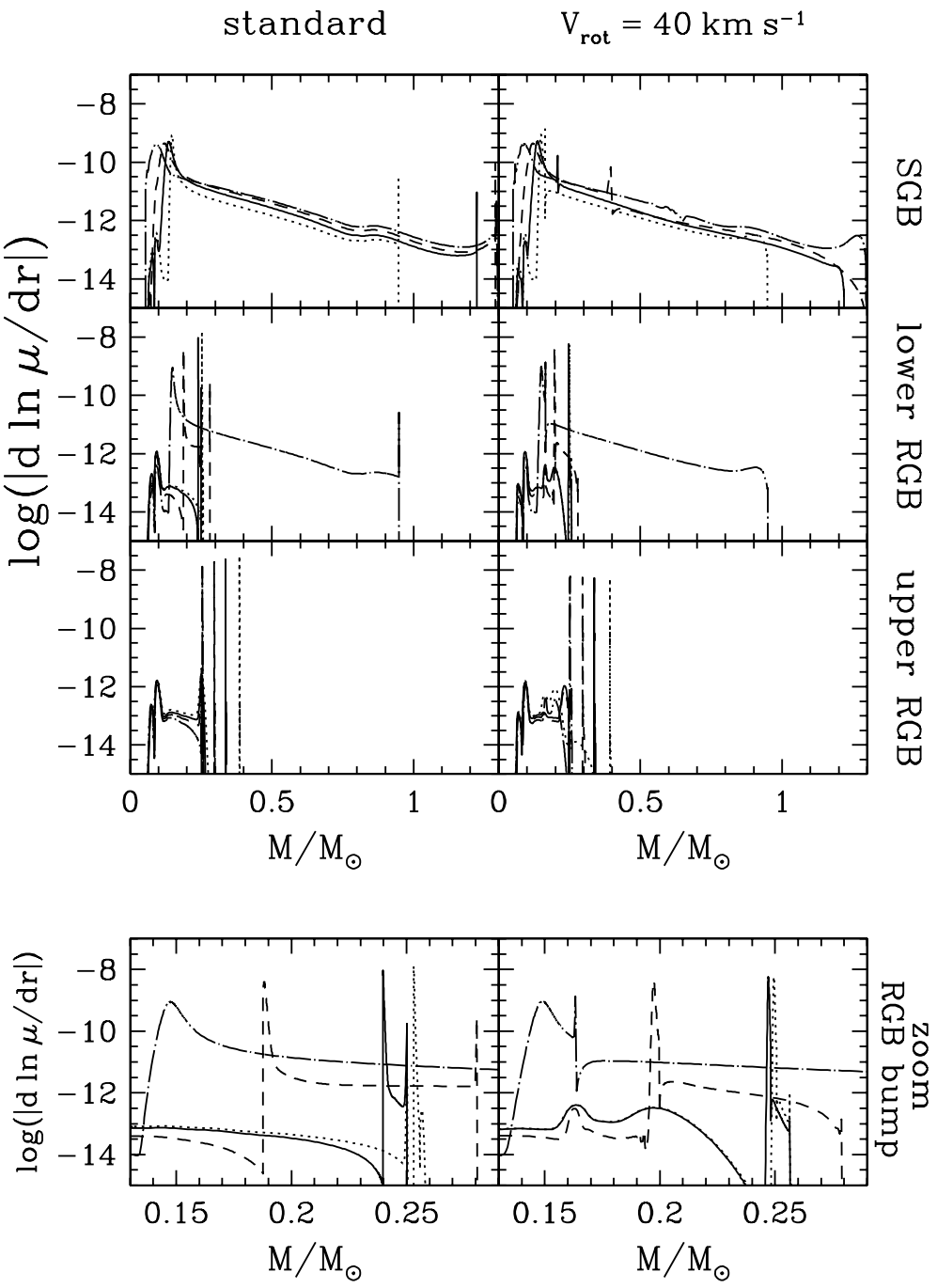

FIG. 9.—Evolution of the gradient of mean molecular weight for a standard model (*left*) and a rotating model (*right*) of a 1.3 $M_\odot$ star of solar metallicity. Each of the upper three pairs of panels shows the profile of μ-gradient at four closely consecutive evolutionary stages located at the SGB, the lower RGB, and the upper RGB, as indicated by the labels at the right. The order of the profiles in each panel is, with increasing evolutionary state (age), dot-dashed lines, dashed lines, solid lines, and finally dotted lines. The last profile on each pair of panels is then plotted again as the first one on the panel immediately below. The bottom pair of panels show zooms of the μ-gradient profiles around the location of the RGB bump. With respect to Fig. 3, the different lines represent F (*dot-dashed line*), C (*dashed line*), just before the RGB bump [$\log(L/L_\odot) = 1.63$; *solid line*], and just past the RGB bump [$\log(L/L_\odot) = 1.66$; *dotted line*].

the envelope only until the approximate location of the RGB bump [$\log(L/L_\odot) \sim 1.6$ for our M67-like giant]. At this position, the situation is very different for the case of rotation with constant J/M in the envelope: this model suddenly starts to experience strong mixing that steadily continues up until the tip of the RGB. This is the canonical extra mixing, whose appearance has been thoroughly discussed in § 5.1.

The dependence of canonical extra mixing on rotation rate, mass, and metallicity is shown in Figures 10 and 11, in which luminosities are normalized with respect to those of the corresponding RGB bump. Such a normalization is optimal for our purposes of looking for mass and metallicity effects because, as has been extensively discussed before, extra mixing only starts to be important once the star has passed the location of this feature in the H-R diagram. Furthermore, in this way we also separate the effects of extra mixing on the upper RGB from those due to the first dredge-up, as well as the different SGB morphologies inherent to different stars. In both figures, the left panels show models with solid-body rotation in the convective envelope for an initial rotation rate of 40 km s^{-1} at turnoff, while the middle and

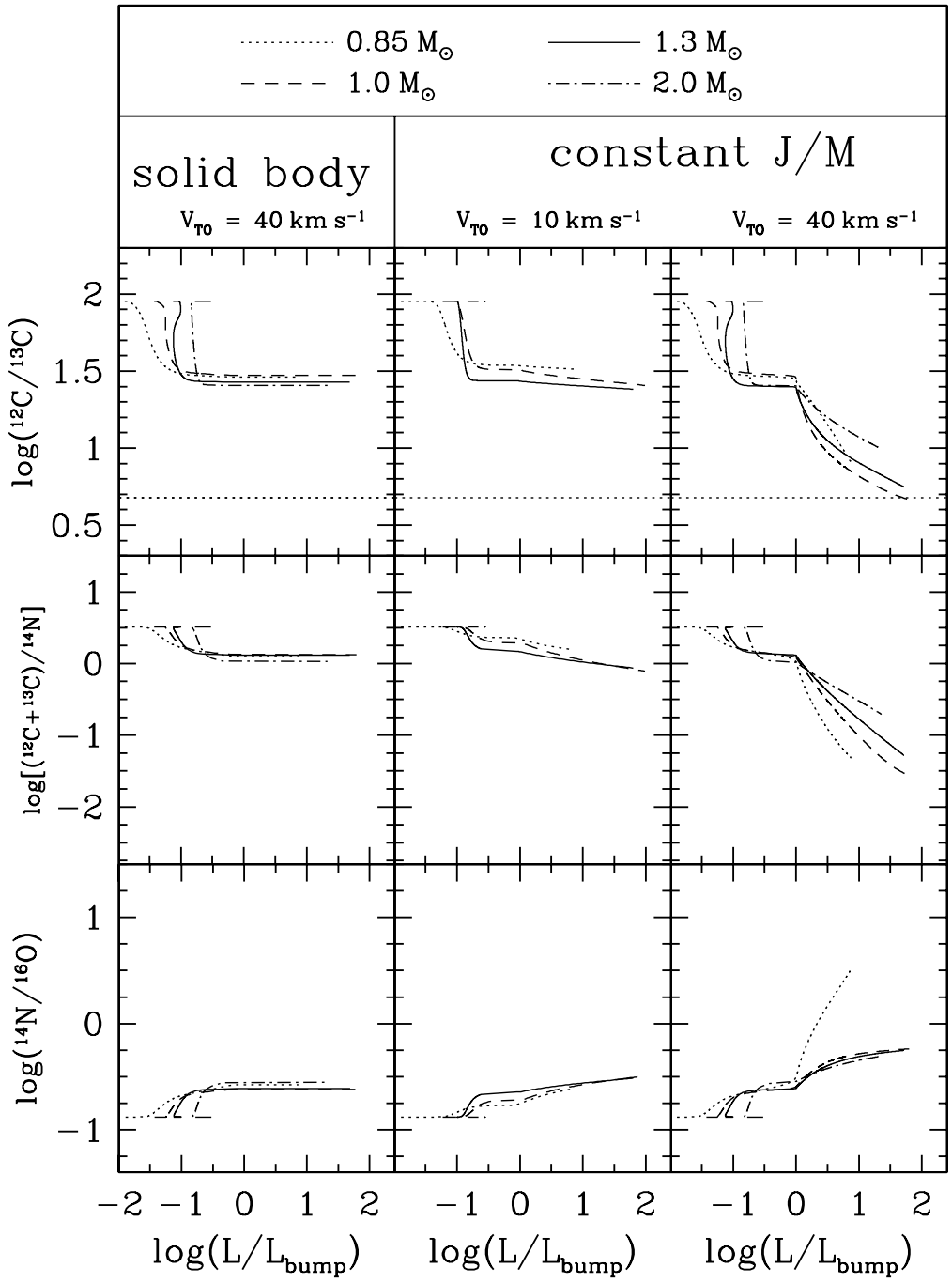

FIG. 10.—Evolution of the surface abundance ratios as a function of stellar mass. Luminosities are plotted with respect to the luminosity of the RGB bump of the corresponding model in order to separate effects due to the first dredge-up from those of extra mixing. The 0.85 $M_{\odot}$ model has [Fe/H] = −2.3, while the other three are solar-metallicity models. All masses display similar behavior, with the differences among them being mainly due to first dredge-up.

right panels show the results of models with differentially rotating envelopes and initial rates of 10 and 40 km s^{-1}, respectively.

At all masses, metallicities, and initial rotation rates, only the models with differential rotation in the convective envelope can mix, and the strongest effect is that of initial rotation rate: the faster the rotation, the more extra mixing.

Once past their respective RGB bumps, the models with constant J/M in the envelope and initial rotation rate of 10 km s^{-1} show very mild extra mixing for all the stellar masses shown in Figure 10, but no obvious trend is distinguishable. For the differentially rotating case with larger initial rotation rate (40 km s^{-1}), however, a slight trend can be noticed of more efficient extra mixing for lower mass stars: the right panels in Figure 10 evidence a larger rate of change in the surface abundance ratios as the stellar mass decreases, or, in other words, the slope of the evolution of the abundance ratios is shallower for higher mass stars. Note that this trend of progressively more efficient mixing is in general very mild, with the exception of the $^{14}N/^{16}O$ ratio in the lowest mass, most metal-poor star, the M92-like case, which shows a very large level of oxygen depletion for the model with an initial rotation rate of 40 km s^{-1} that is not shared by any of the higher mass models.

Metallicity effects are explored in Figure 11, where we plot the evolution of the surface abundances for rotating models of giants

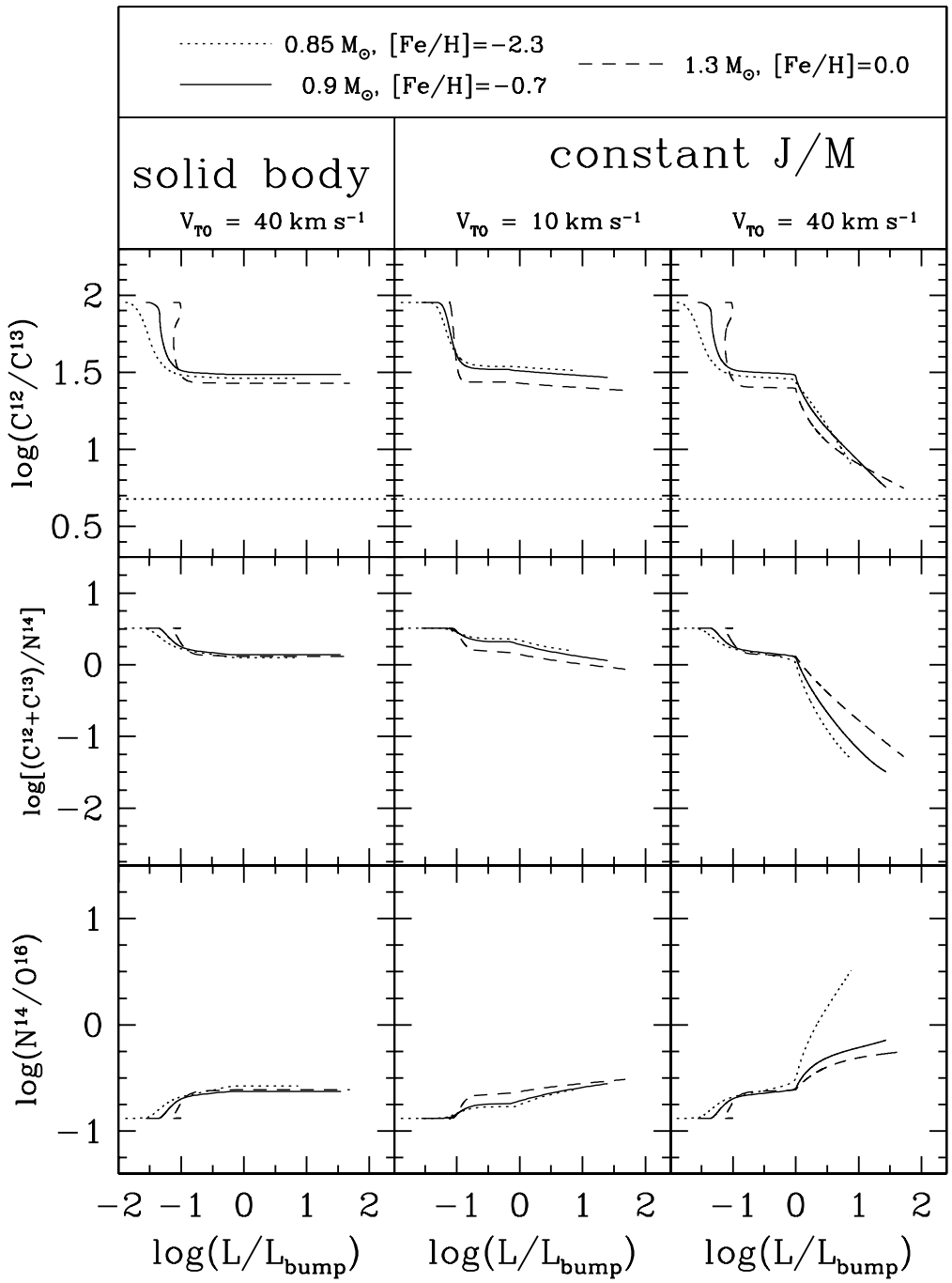

FIG. 11.—Metallicity dependence of the evolution of surface abundance ratios for rotating stellar models. Luminosities are plotted with respect to the luminosity of the RGB bump of the corresponding model in order to separate metallicity effects due to the first dredge-up from those of extra mixing. Left panels correspond to solid-body rotation in the convective envelope, and right panels to constant specific angular momentum.

representative of clusters with progressively decreasing metallicity: M67, M71, and M92. The situation is very similar to that of Figure 10. For an initial rotation rate of 10 km s^{-1} (*middle panels*), the evolution of the surface abundances is only slightly different than the standard case. Although the three lines are vertically displaced from one another (due to their different standard first dredge-up), the rates of change of the surface ratios after the RGB bump for the three stars are essentially indistinguishable. For a larger initial rotation rate (*right panels*), however, extra mixing is strong in all of them, and, although it would be ambiguous to say anything from the evolution of the $^{12}C/^{13}C$ ratio, the other two abundance ratios, $(^{12}C + ^{13}C)/^{14}N$ and $^{14}N/^{16}O$, clearly indicate more efficient extra mixing for the more metal-poor stars.

Finally, we explore the effects of varying our choice of the maximum depth for extra mixing. As discussed in § 3.1, we parameterize the mixing depth as the location where some (large) fraction of the total luminosity is generated, that is, to some coordinate close to the top of, but inside, the HBS. For no strong reason in particular, we chose this fraction to be 99%. We compare this choice with the recent work by Denissenkov & VandenBerg (2003), where they find that the mass coordinate at which $\Delta \log T = 0.19$ produces a good match between their models and the data of field giants. The top panel of Figure 12

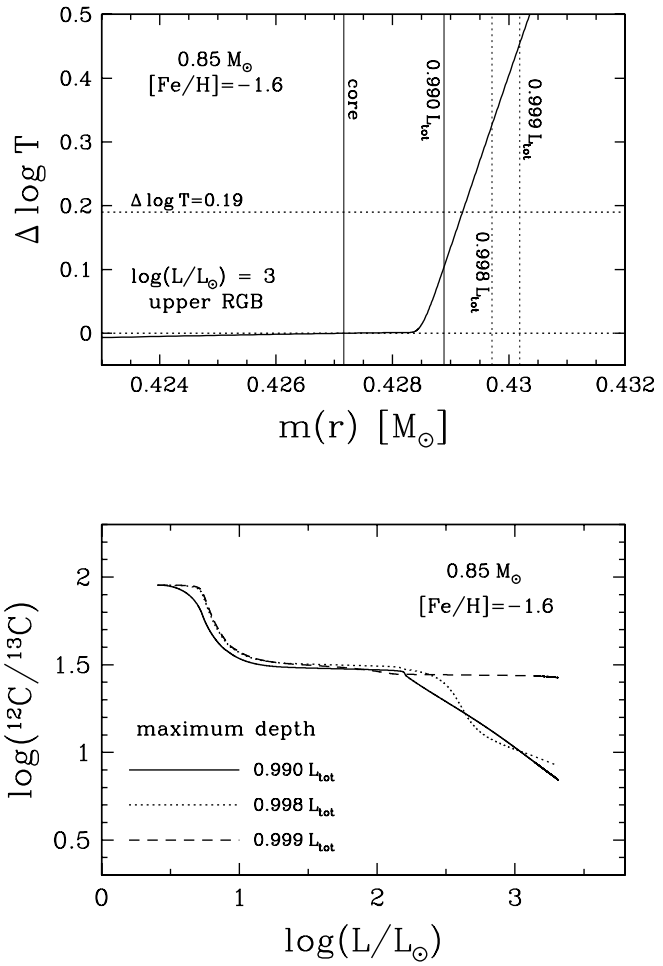

FIG. 12.—Exploring the variation of the maximum depth for extra mixing. For a star of 0.85 $M_{\odot}$ and [Fe/H] $= -1.6$ ($Z = 0.0005$), the top panel compares the parameterization of the maximum depth for extra mixing in terms of the temperature inside the HBS and our parameterization in terms of some fraction of the total stellar luminosity. Here $\Delta \log T \equiv \log T(M_{\rm core}) - \log T(M_{\rm mix})$, where $M_{\rm core}$ and $M_{\rm mix}$ are the mass coordinate of the core's surface and of the maximum depth for mixing, respectively. The dotted horizontal line at $\Delta \log T = 0.19$ indicates the best value found by Denissenkov & VandenBerg (2003) for the same stellar mass and metallicity, which in our models lies in between the locations at which 99% and 99.8% of the total luminosity is generated. The bottom panel shows that, for mixing depths between these two mass coordinates, our models produce almost the same amount of canonical extra mixing, as indicated by the evolution of the surface $^{12}C/^{13}C$ ratios.

shows the parameter $\Delta \log T$ in the region of interest for one of our models of a 0.85 $M_{\odot}$ star of [Fe/H] $= -1.6$ ($Z = 0.0005$), the same star studied by Denissenkov & VandenBerg (2003). It can be seen that our chosen depth [marked by the vertical line close to $m(r) = 0.429$] is slightly deeper than the location where $\Delta \log T = 0.19$.

In order to quantify the effect of changing the maximum depth, we run models with shallower mixing, as indicated in the top panel of Figure 12, where the dotted vertical lines mark the locations at which 99.8% and 99.9% of the total luminosity is generated. Note that the preferred mixing depth of Denissenkov & VandenBerg (2003), $\Delta \log T = 0.19$, lies in between the depths set by 99% and 99.8% of the total luminosity. The bottom panel of Figure 12 shows the RGB evolution of the $^{12}C/^{13}C$ ratio for the models with maximum depths of 99.8% (*dotted line*) and 99.9% (*dashed line*) of the total luminosity, in comparison with our adopted depth (*solid line*). While the model with the most shallow mixing does not experience almost any extra mixing, the model with just 0.1% deeper in total luminosity produces as much extra mixing as that of our adopted depth. Therefore, we see that reasonable variations of the maximum depth for extra mixing do not affect our results on the evolution of the carbon isotopes.

6. RESULTS: COMPARISON TO OBSERVATIONS

The general trends discussed in § 5 provide a set of theoretical predictions that can be tested against the large observational database. We begin with our benchmark solar abundance case, the old open cluster M67. In this system the theoretical predictions match the observed pattern. However, we will see that there are some issues related to the behavior of more massive Population I giants, as well as with the metal-poor Population II giants in the field and globular clusters, that depart from the theoretical expectations. In our view these two issues provide two distinct clues about the underlying physical nature of the mixing process, namely, that the overall efficiency of mixing must be higher than in our base case, and that there must be a relative reduction in the efficiency of mixing in more rapidly rotating giants. We discuss the physical interpretation of these empirical results in § 6.4.

6.1. *Population I Giants*

Figure 13 summarizes the $^{12}C/^{13}C$ data in the old open cluster M67 (Gilroy & Brown 1991; Tautvaisiene et al. 2000) and illustrates the dependence of the first dredge-up on the initial $^{12}C/^{13}C$ ratio with M67-like standard models. In Figure 14 we compare the luminosity evolution of our rotating models to the M67 data, where the clump giants have been placed at a luminosity higher than that of the RGB tip to indicate that, in an evolutionary sense, they are posterior to the first-ascent giants. Finally, the predicted RGB tip abundances as a function of mass and rotation rate are compared with open cluster $^{12}C/^{13}C$ ratio data (Gilroy 1989) in Figure 15.

Three stages can be identified in the M67 data. The subgiants (*open triangles*) clearly have a higher $^{12}C/^{13}C$ ratio than the more evolved stars, and the lower RGB data (*filled circles*) level off at $^{12}C/^{13}C \sim 22$. These values are consistent with the theoretically expected first dredge-up and lack of mixing on the lower RGB itself (i.e., prior to the RGB bump), regardless of rotation rate, angular momentum distribution in the convective envelope, or any inhibiting effect of μ-barriers. The intermediate-luminosity giants [$\log (L/L_{\odot}) \sim 2.2$] have conflicting data; Gilroy & Brown (1991) reported lower ratios than for the faint giants, while Tautvaisiene et al. (2000) reported the same abundances for these stars as found for the fainter giants. The clump giants (*crosses*) show the lowest $^{12}C/^{13}C$ ratios, indicating the presence of a mixing episode either on the upper RGB [past $\log (L/L_{\odot}) \sim 1.8$] or associated with the helium flash. The first explanation is more consistent with the trends seen in more densely sampled Population II giant studies. Models with turnoff rotation rates similar to the predicted ones for progenitors of M67 giants (20–40 km s^{-1}) successfully reproduce the observed trends, while more rapidly rotating models have too much mixing (Fig. 14).

The comparison with $^{12}C/^{13}C$ data as a function of mass in Figure 15 is at first glance similarly encouraging, with the 20 km s^{-1} turnoff rotation models reproducing the observed data. However, the actual theoretical prediction is that shown by the solid line since, as discussed in § 3.3, the mean rotation rates of turnoff stars increase dramatically above $\sim$1.3 $M_{\odot}$, so the data in this mass range are actually much less mixed than we would expect based on typical turnoff rotation rates of 150 km s^{-1} above the break in the Kraft (1967) mass-rotation relationship (Fig. 2).

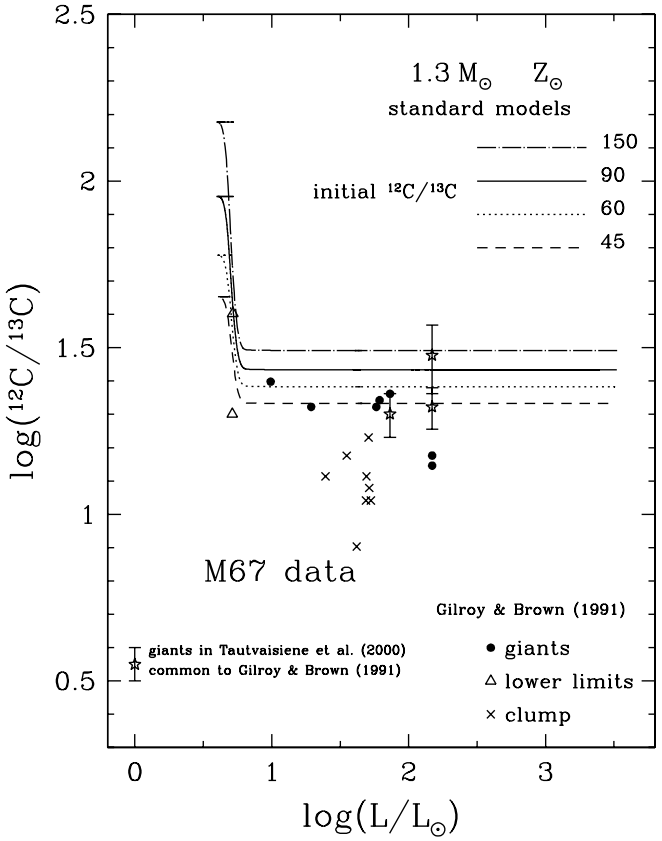

FIG. 13.—Dependence of the post–first dredge-up $^{12}C/^{13}C$ ratio on the adopted initial $^{12}C/^{13}C$ value. The four lines are standard (i.e., nonrotating) models of M67-like giants with varying MS $^{12}C/^{13}C$ ratios, bracketing the range of values measured in the interstellar medium of the Galaxy. It can be seen that the surface $^{12}C/^{13}C$ ratio at the end of the first dredge-up depends on the initial $^{12}C/^{13}C$ ratio. Also shown are the $^{12}C/^{13}C$ data for M67 evolved stars from two different sources. Filled circles, open triangles, and crosses are taken from Gilroy & Brown (1991), representing red giants with actual detections of both carbon isotopes, lower limits, and clump stars, respectively. Uncertainties in these $^{12}C/^{13}C$ data are typically between 5% and 8%. Stars with error bars represent the measurements of Tautvaisiene et al. (2000) of three giants in common with Gilroy & Brown (1991), corresponding to the three most luminous ones in the sample.

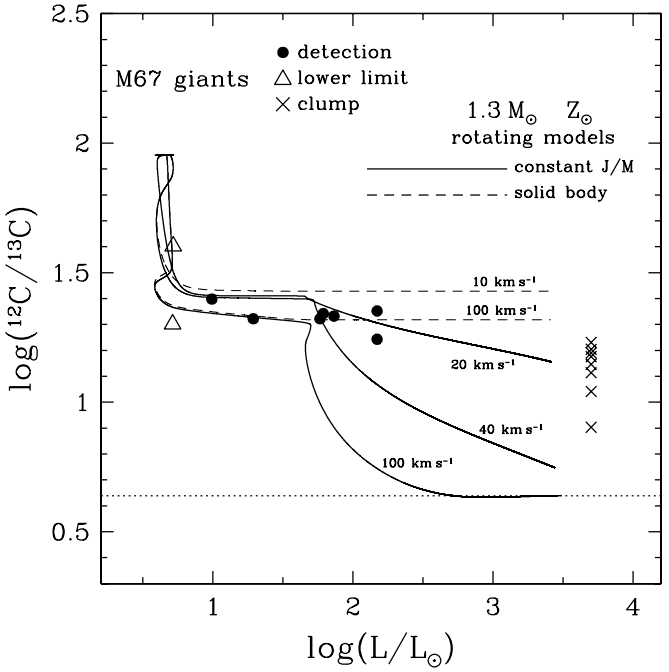

FIG. 14.—Post-MS evolution of the surface $^{12}C/^{13}C$ ratio of a rotating 1.3 $M_\odot$ star of solar metallicity as a function of the rotational velocity at turnoff, for the two extreme cases of angular momentum distribution in the convective envelope. The dotted horizontal line indicates the nuclear equilibrium value of $^{12}C/^{13}C \sim 4.5$. The $^{12}C/^{13}C$ data for M67 of Gilroy & Brown (1991) and Tautvaisiene et al. (2000) have been averaged. Filled circles represent giants with actual detections, and open triangles are giants with only lower limits. The clump stars are represented by crosses and have been placed at $\log(L/L_\odot) = 3.7$ in order to avoid crowding and also to indicate that, in an evolutionary sense, they have already been through the first-ascent RGB. Their actual luminosities are those shown in Fig. 13.

The mean measured $^{12}C/^{13}C$ ratio for the faint M67 giants (lower RGB) is moderately below the theoretically predicted values, as can be seen in Figure 13. Some classes of models (fast rotation) experience internal mixing on the SGB, and it is tempting to ascribe these lower $^{12}C/^{13}C$ measurements to the existence of such early mixing. However, there is a significant uncertainty in the initial conditions that is not usually included in theoretical models of RGB mixing. The predicted post–dredge-up abundances are a sensitive function of the assumed turnoff $^{12}C/^{13}C$ ratio. Although the solar mix value is commonly assumed, there is no a priori reason why all stars should share this local property.

Measurements of the $^{12}C/^{13}C$ ratio toward molecular clouds in the solar neighborhood show a wide range of values, ranging from as low as 40 to as high as 150 (Goto et al. 2003), and there exists an unmistakable trend of increasing $^{12}C/^{13}C$ ratio from the Galactic center to the edge of the Galaxy (Langer & Penzias 1990), clearly indicating different stages in the evolution of carbon at different Galactic locations after a number of generations of stars. Until $^{12}C/^{13}C$ ratios are obtained for dwarfs in the distant stellar clusters under study (see Carretta et al. 2005), the only safe assumption regarding its initial or MS value is that

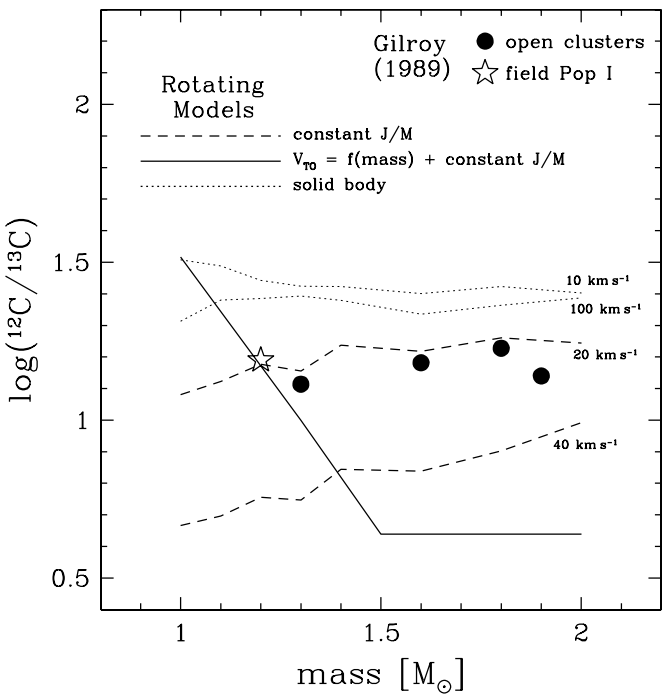

FIG. 15.—Comparison between the $^{12}C/^{13}C$ open cluster data from Gilroy (1989) and our rotating models. The theoretical lines represent the $^{12}C/^{13}C$ ratio at the tip of the RGB, just before the helium flash. Dotted and dashed lines are, respectively, models with solid-body and differential rotation enforced in the convective envelope. For both types of angular momentum law, the tip $^{12}C/^{13}C$ ratios are plotted for two initial rotation rates, as indicated. The solid line represents models with differential rotation in the envelope and initial rotation rates selected according to the stellar mass as given by the Kraft (1967) curve.

this should be systematically higher the older the population in question is.

The dependence of the $^{12}C/^{13}C$ ratio after first dredge-up is shown by the four lines in Figure 13, which correspond to standard models with varying initial ratios. The level of the first dredge-up among the M67 giants is best explained with initial $^{12}C/^{13}C$ ratios lower than the solar system value, but consistent with that inferred from the large-scale Galactic trend at the position of this cluster. This low value, however, may have been higher 4–4.5 Gyr ago, when the Sun and the M67 stars formed.

6.2. *Population II Giants: The Field*

While the open clusters (Figs. 14 and 15) represent the high-metallicity half of the problem of abundance anomalies in red giants, the old field population and the globular clusters comprise the much better explored, both observationally and theoretically, metal-poor half. In summary, the field data show a nonnegligible scatter in the initial abundances, no changes in the abundance ratios during the lower RGB, and the presence of nonstandard mixing operating on stars brighter than the lower RGB and past the bump.

One of the most comprehensive studies of old, metal-poor field giants is that of Gratton et al. (2000), which selected well-studied stars with metallicities in the range $-2 < [Fe/H] < -1$. In Figure 16 we present a comparison between the Gratton et al. (2000) data and rotating models for a representative fieldlike star of 0.9 $M_\odot$ and $[Fe/H] = -1.4$. In the panel with the $^{12}C/^{13}C$ ratios, filled circles represent reliable measurements (i.e., both isotopes are detected) and the open triangles are stars with only lower limits. The HB stars of the sample are not included. With varying degrees, the data in all four panels of Figure 16 show the signatures of some gradual CNO processing as the luminosity increases: conversion of ^{12}C into ^{13}C, overall carbon depletion, and nitrogen enhancement.

In the same spirit as with M67, we dissect the field data of Figure 16 into three different evolutionary stages. The first goes from the MS turnoff (or even before) to the completion of the first dredge-up during the SGB. Since all the $^{12}C/^{13}C$ data of this phase are lower limits, the only thing that can be said about them is that they are at least at the level of or above the standard first dredge-up expectation, except for the four MS stars with lower limits below $^{12}C/^{13}C \sim 20$. For the other three abundance ratios shown ([C/N], [C/O], and [N/O]) the large intrinsic scatter, present already among the MS stars, obscures any possible underlying trend on this early evolutionary stage [$\log (L/L_\odot) \gtrsim 1$]. This indicates that a similarly large scatter in abundance ratios on more evolved stages may be primordial and need not require star-to-star variations due to mixing.

The second evolutionary stage is better populated with data and corresponds to the lower RGB, in the interval $1.2 \lesssim \log (L/L_\odot) \lesssim 2$. The abundance ratios do not change along the lower RGB. The third distinct group of stars are those on the upper RGB, with luminosities brighter than $\log (L/L_\odot) \sim 2.1$, and which show in all panels systematically lower $^{12}C/^{13}C$ and [C/N] ratios than stars on the lower RGB. These stars exhibit clear evidence of in situ mixing on the upper RGB.

Finally, there is no evidence in the [O/Fe] measurements of Gratton et al. (2000) of any change in oxygen (as well as in the data of Fulbright & Johnson 2003), and thus the low levels of [C/O] and high levels of [N/O] in the bottom two panels are the result of the aforementioned carbon depletion and nitrogen enhancement, respectively. This implies that the extra mixing in these field giants is not deep enough to reach regions of significant ON processing, as is the case in some globular clusters (§ 6.3).

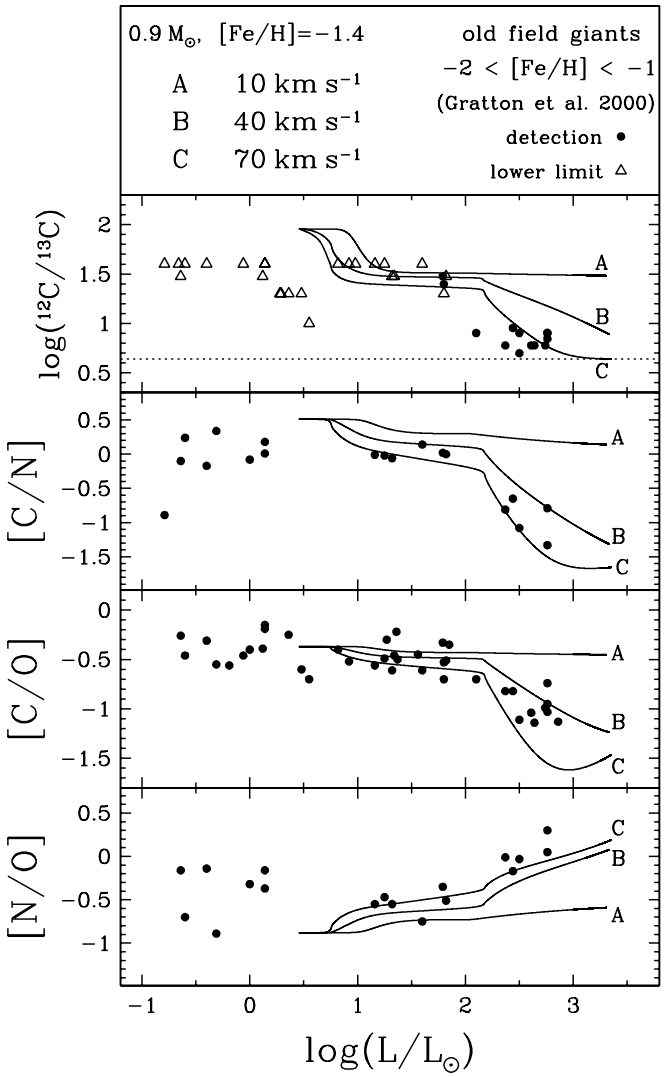

FIG. 16.—Comparison between the Gratton et al. (2000) data for metal-poor field giants with well-determined metallicities in the range $-2 < [Fe/H] < -1$ and rotating models of a star of 0.9 $M_\odot$ and a metallicity of $[Fe/H] = -1.4$. Initial rotation rates are 10, 40, and 70 km s^{-1}, corresponding to models with a turnoff rotation rate of 4 km s^{-1} and mixing velocities enhanced by a factor of $(10/4)^2$, $(40/4)^2$, and $(70/4)^2$, respectively. The dotted horizontal line in the top panel indicates the nuclear equilibrium value of $^{12}C/^{13}C \sim 4.5$. Compare with the $^{12}C/^{13}C$ ratios of globular cluster giants of Fig. 17.

The models in Figure 16, chosen to be representative of the Gratton et al. (2000) field data, started from a rigidly rotating MS turnoff star with surface rotation rates of 10, 40, and 70 km s^{-1}, and, given that we already know that models with rigidly rotating envelopes do not mix, only models with constant specific angular momentum in the convective envelope are considered. Before going further, note that the initial mixture used to generate these models is solar, which is not the most optimal mixture to use for comparison to metal-poor field stars. Increasing evidence (Bessell & Norris 1982; Henry et al. 2000; Norris et al. 2001, 2002; Li & Burstein 2003; Israelian et al. 2004) indicates that a significant fraction of these stars have overabundant amounts of nitrogen (with respect to solar). Thus, when inspecting the panels of Figure 16 involving nitrogen, one has to bear in mind that the lines representing our theoretical results could be shifted vertically by that initial overabundance.

The evolution of the theoretical surface ratios is very similar to those of Figure 14. First, the post–dredge-up level of the

models [$\log (L/L_{\odot}) \approx 1.3$] is dependent on the initial rotation rate, which is the result of extra mixing in the deep radiative interior prior to the occurrence of the maximum penetration of the convective envelope (i.e., before the end of the first dredge-up). Furthermore, the post dredge-up ratios of the models are consistent with the $^{12}C/^{13}C$ ratios of field giants in this luminosity range (*top panel*) and also with the [C/N] and [N/O] data (recall here that the likely higher initial nitrogen abundances would vertically shift these lines), while the large scatter in the [C/O] data prevents us from saying anything about this ratio.

Second, along the lower RGB, $1.2 \lesssim \log (L/L_{\odot}) \lesssim 2.1$, all rotating models of fieldlike giants show little or no extra mixing: the $^{12}C/^{13}C$ ratio does not change at all, the total carbon and nitrogen abundances do change although very slowly and are inversely correlated, while oxygen remains unaltered.

Finally, the third distinct evolutionary stage corresponds to the upper RGB, after the occurrence of the RGB bump, $\log (L/L_{\odot}) \approx 2.2$, and at which point the models with differential rotation in the envelope experience strong extra mixing. The amount of nonstandard mixing is a strong function of the initial rotation rate. The case of $V_{\rm TO} = 10$ km s^{-1} (which, we recall, actually corresponds to an upper limit for the rotation rates of old field stars) experiences very little extra mixing and is not able to reproduce the abundances of stars brighter than the RGB bump, which all show $^{12}C/^{13}C \lesssim 10$. For larger initial angular momentum budgets, however, the extra mixing is vigorous, and the top panel shows that the low values of $^{12}C/^{13}C$ are achieved by the model with an initial rotation rate of $V_{\rm TO} = 70$ km s^{-1} at approximately the right luminosities. The two middle panels of Figure 16 show that, for initial rotation rates between 40 and 70 km s^{-1}, our models reproduce the right [C/N] and [C/O] ratios. The bottom panel, showing the evolution of the [N/O] ratio, would seem to require a higher degree of oxygen depletion, since most data points fall above the model with $V_{\rm TO} = 70$ km s^{-1}. However, if we had started with a larger initial nitrogen abundance, as shown by a fraction of metal-poor field stars, it is easy to verify that such a discrepancy would disappear and the evolution of the [N/O] ratio of the models would agree with the Gratton et al. (2000) data.

Nevertheless, despite this apparent success of the models with larger rotation rates at turnoff, we need not forget that metal-poor field stars are observed to have rotation velocities of less than 10 km s^{-1} (§ 3.3). Therefore, the maximal mixing scenario, with the currently available estimates for the velocities of extra mixing, cannot reproduce the observed abundances of these old field stars with rotation rates that are sensible for them.

In conclusion, and considering that the amount of extra mixing scales as the square of the rotation rate, we obtain that the diffusion coefficients associated with the rotationally induced hydrodynamic instabilities as computed in our code (§ 3.1 and Appendix) are too small by a factor between FC $= (40/10)^2 \sim 20$ and FC $= (70/10)^2 \sim 50$ to account for the surface abundance patterns of metal-poor field giants. Note also that this conclusion applies for surface rotation rates of stars that are rotating rigidly at the MS turnoff. If, contrary to the solar case, we had started our models from differentially rotating MS stars, then, for any fixed initial surface rotation rate, the extra mixing would have been much more vigorous than that of the models we show in Figure 16 simply because of the larger initial angular momentum budget of the turnoff star (see § 3.2 and eq. [3]).

6.3. *Population II Giants: Globular Clusters*

The case of globular clusters is explored in Figures 17–20. In the first two we plot, respectively, data on the $^{12}C/^{13}C$ ratio for several globular clusters and carbon and nitrogen data for M92. The issue of oxygen depletion is explored in Figures 19 and 20 using very recent data for M13 and NGC 6752, two globular clusters with approximately the same metallicity.

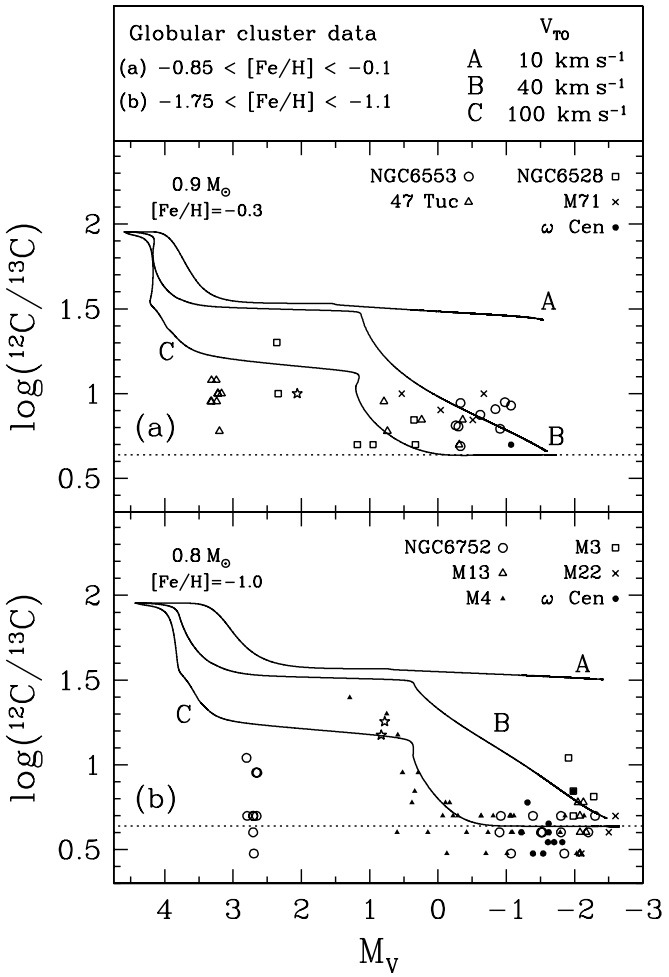

FIG. 17.—Comparison between surface $^{12}C/^{13}C$ ratios of globular cluster giants and our rotating models. The data have been separated into two ranges of metallicity and plotted in comparison to stellar models representative of the corresponding sample, for initial rotation rates of 10, 40, and 100 km s^{-1} at turnoff. These correspond to models with a turnoff rotation rate of 4 km s^{-1} and mixing velocities enhanced by a factor of $(10/4)^2$, $(40/4)^2$, and $(100/4)^2$, respectively. Data for NGC 6553, NGC 6528, and 47 Tuc are taken from Shetrone (2003), except for the 47 Tuc giants populating the lower RGB ($M_V \sim 3.3$), which are from Carretta et al. (2005); for M3 from Pilachowski et al. (2003); for ω Cen from Smith et al. (2002); for M71 from Briley et al. (1997); for M13 from Shetrone (1996b); for M22 from Suntzeff & Smith (1991); for NGC 6752, the brightest giants are from Suntzeff & Smith (1991) and the lower RGB giants ($M_V \sim 2.7$) from Carretta et al. (2005); and for M4 from both Shetrone (2003) and Suntzeff & Smith (1991). The data point marked as a star in (*a*) is a giant in NGC 6528 ([Fe/H] $= -0.1$) for which the measurement is only a lower limit, as are the two stars in (*b*) but representing red giants in M4 ([Fe/H] $= -1.1$).

The $^{12}C/^{13}C$ data in Figure 17 have been separated in two samples according to metallicity. In Figure 17*a* we include clusters with [Fe/H] > -0.7, plus one ω Cen star of [Fe/H] $= -0.85$, and Figure 17*b* shows data from clusters with $-1.6 <$ [Fe/H] < -1.1 and ω Cen stars as metal-poor as [Fe/H] $= -1.75$. The data point marked as a star in Figure 17*a* is a giant in NGC 6528 ([Fe/H] $= -0.1$) for which the measurement is only a lower limit, as are the two stars in Figure 17*b* but representing red giants in M4 ([Fe/H] $= -1.1$). Error bars have been omitted to avoid confusion, but the reader should bear in mind that all the faintest data points in both panels have large uncertainties: in Figure 17*a*, the

two NGC 6528 giants with $M_V \sim 2.4$ have error bars that reach $\log(^{12}C/^{13}C) \sim 1.5$, and the same applies, in Figure 17*b*, for the three M4 giants closest to the data points representing lower limits and marked by stars.

Until very recently, almost all the $^{12}C/^{13}C$ data for globular cluster giants were restricted to luminous giants past the RGB bump and close to the RGB tip. Therefore, little could be said about the first two stages in the post-MS mixing history amply discussed for M67 and the field giants (the first dredge-up dilution and the lower RGB, before the RGB bump). Recently, however, Carretta et al. (2005) obtained the first measurements of $^{12}C/^{13}C$ in stars close to the base of the RGB (as well as some MS turnoff stars) in 47 Tuc and NGC 6752. These data, although restricted to a very narrow range of luminosities, have important implications for our following discussion.

Both groups of globular cluster giants in Figure 17 show very low $^{12}C/^{13}C$ ratios, but it is still possible to notice the slight metallicity dependence of these data: the more metal-rich sample has $\langle ^{12}C/^{13}C \rangle \sim 6.3$, while the most metal-poor sample has $\langle ^{12}C/^{13}C \rangle \sim 4$.

Next, is there indication in the globular cluster data of Figure 17 of any evolution of $^{12}C/^{13}C$ with luminosity on the RGB such as that observed among open cluster and metal-poor field giants? Shetrone (2003) found that to be the case among giants in the globular cluster M4 (Fig. 17*b*, *filled triangles*), which indeed seem to show high values of $^{12}C/^{13}C$ before and around the bump luminosity ($M_V \sim 0.5$), but which rapidly decrease toward higher luminosities, with all the M4 giants past $M_V \sim 0$ showing $^{12}C/^{13}C$ ratios already close to nuclear equilibrium. A similar indication, although not as obvious as in M4, may be seen in the data for NGC 6528 (Fig. 17*a*, *squares*). These two clusters, therefore, indicate a continuous evolution of the surface $^{12}C/^{13}C$ along the RGB. Also, as can be seen in the models in this figure, such luminosities correspond very well with the expected location of the RGB bump for stars of approximately the right masses and metallicities.

At the same time, however, the recent data from Carretta et al. (2005) for 47 Tuc and NGC 6752 tell a different story, by showing very low values of $^{12}C/^{13}C$ and a large scatter among giants at the base of the RGB, that is, much earlier than the RGB bump. This indicates that the stars in these samples already had these low values of $^{12}C/^{13}C$ before becoming giants. If that is the case, then these stars acquired their current anomalous patterns of surface abundances via pollution from more massive stars from the same or a previous generation, and the problem then becomes figuring out at what point in their evolution the current giants incorporated this enriched material, either while they were MS stars or, alternatively, during the star formation process.

An alternative to this pollution scenario would be the action of very strong extra mixing soon after the MS turnoff, but this possibility is unlikely given the unrealistically large mixing velocities that would be required. Note, nevertheless, that three of the lower RGB stars in NGC 6752 from Carretta et al. (2005) show $^{12}C/^{13}C \sim 10$, while all the stars from this same cluster but with higher luminosities studied by Suntzeff & Smith (1991) display essentially nuclear equilibrium values. This may be an indication of continuous extra mixing even among stars that arrived to the RGB already with anomalous abundance ratios. There is, therefore, clear evidence in globular clusters for both evolutionary and primordial variations in the abundances of carbon isotopes, with neither of these scenarios necessarily excluding the other but, rather, operating at the same time.

For comparison with the globular cluster $^{12}C/^{13}C$ data in Figure 17, we generate rotating stellar models of 0.9 $M_\odot$ with [Fe/H] $= -0.3$ and 0.8 $M_\odot$ with [Fe/H] $= -1.0$, for Figures 17*a* and 17*b*, respectively. The former corresponds to a metallicity intermediate between that of M71 or 47 Tuc and that of NGC 6528, and the latter corresponds closely to giants in M4, which has a turnoff mass $\sim$0.81 $M_\odot$ and [Fe/H] $= -1.1$ (Richer et al. 1997). Only models with constant specific angular momentum in the convective envelopes are shown.

Adequate turnoff rotation rates for the progenitors of globular cluster giants are $V_{TO} \sim 4$ km s^{-1}. However, with the estimates of mixing velocities available today (implemented in YREC), such a slow rotation does not produce almost any changes in the surface abundances. Therefore, we run models with turnoff rotation rates of 10, 40, and 100 km s^{-1}, which correspond to models with $V_{TO} = 4$ km s^{-1} and diffusion velocities multiplied by a factor of $(10/4)^2$, $(40/4)^2$, and $(100/4)^2$, respectively. Similarly, models with fast initial rotation mimic models of slow initial rotation but rapidly spinning cores at the turnoff (§ 3.2).

As previously seen for models of M67 and field giants, different initial rotation rates produce different amounts of extra mixing immediately after the turnoff and during the SGB, so that the post–first dredge-up $^{12}C/^{13}C$ ratio is a function of the initial angular momentum budget. Again, this is just a consequence of the noninclusion in our models of any inhibiting effects of μ-barriers. Vigorous mixing during the SGB, as indicated by the model with $V_{TO} = 100$ km s^{-1} [equally reproduced by a model of $V_{TO} = 4$ km s^{-1} plus a factor of FC $= (100/4)^2 = 625$ more efficient extra mixing, i.e., larger diffusion coefficients], is capable of producing a factor of 2 smaller $^{12}C/^{13}C$ ratios after dredge-up. However, if the starting $^{12}C/^{13}C$ ratio is indeed like that of the solar system, one would need even stronger extra mixing than that experienced by the most mixed model in Figure 17 during the SGB in order to get close to the $^{12}C/^{13}C$ values shown by the lower RGB giants studied by Carretta et al. (2005), which is very unlikely.

Instead, what these low-luminosity giants might indicate is that the starting mixture has a significantly lower $^{12}C/^{13}C$ than that of the solar system. Indeed, rotating models with initial $^{12}C/^{13}C$ as low as 30 (not shown in Fig. 17 to avoid confusion), while achieving lower levels of $^{12}C/^{13}C$ during the first dredge-up, still do not fall as low as the lower RGB stars in 47 Tuc and NGC 6752. We conclude, therefore, that the low $^{12}C/^{13}C$ ratios of lower RGB giants in 47 Tuc and NGC 6752 are most likely primordial to the RGB, and their origin poses an interesting problem yet to be solved. This again demonstrates that the adoption of a solar system mixture of carbon isotopes as a starting point for the models is a bad one.

Past the bump [at $M_V \approx 1.2$ or $\log(L/L_\odot) \approx 1.45$ for the models in Fig. 17*a*, and $M_V \approx 0.4$ or $\log(L/L_\odot) \approx 1.90$ for models in Fig. 17*b*], on the upper RGB, stars are well mixed, based on $^{12}C/^{13}C$ as an indicator.

In Figure 18 we plot carbon and nitrogen abundances for giants in M92 and compare them to our M92-like rotating models. The [C/Fe] data in the top panel represented by filled circles are from Bellman et al. (2001), who extended earlier work by Carbon et al. (1982) and Langer et al. (1986) in order to determine the luminosity at which the carbon depletion reported by these works sets in. The open circles represent stars from Langer et al. (1986) that were not observed by Bellman et al. (2001), which mainly fill the faint end of the M92 RGB. Since Bellman et al. (2001) report only carbon abundances, we plot in the middle and bottom panels the carbon and nitrogen abundances of Carbon et al. (1982). In these two panels the filled circles represent all those M92 stars for which the nitrogen abundance is reliable as reported by Carbon et al. (1982), and the open

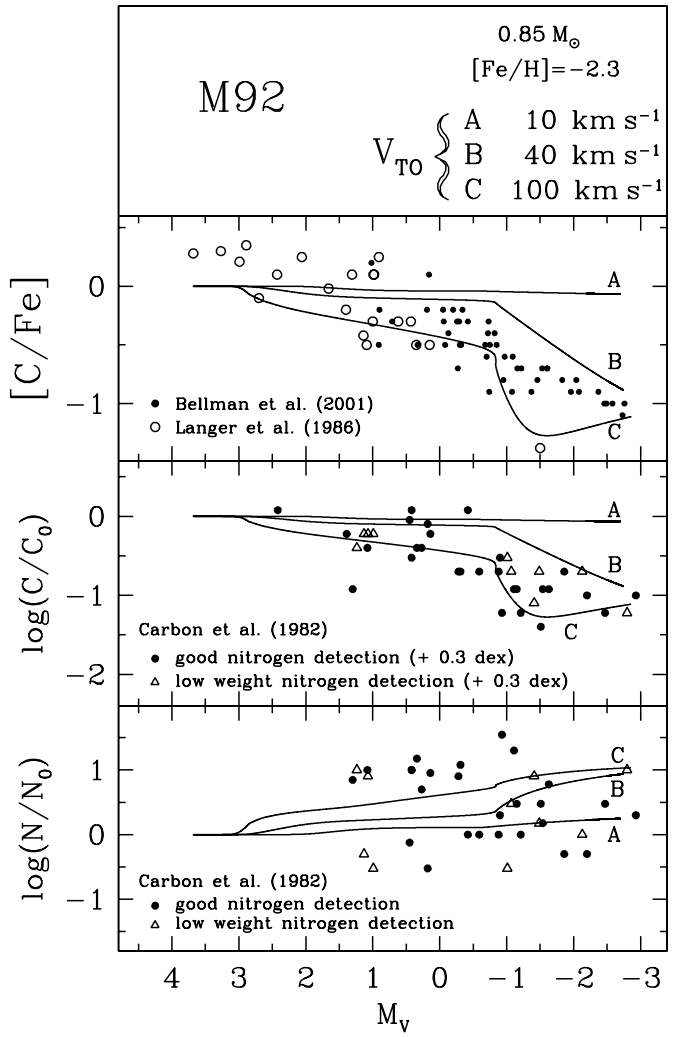

FIG. 18.—Carbon and nitrogen abundances of M92 giants as compared to the same rotating models of M92-like giants of Fig. 17. The models, which all started from a solar mixture, have been arbitrarily set to zero in the vertical axes of all panels. Note, however, that initial mixtures more appropriate to globular cluster stars would make the models shift up and down.

triangles represent those with uncertain (low weight) nitrogen abundances. The carbon abundances from Carbon et al. (1982) have been shifted vertically by +0.3 dex in order to bring the zero point of those measurements in agreement with the (solar) initial mixture of our models, and we do this because the goals of this investigation do not involve initial abundances, but rather their subsequent evolution under the action of extra mixing.

The carbon abundance data in the upper two panels of Figure 18 unambiguously show a progressive depletion of carbon with increasing luminosity along the RGB, although the large dispersion at any given magnitude makes difficult a secure determination of where this depletion starts. Note that the data points with uncertain nitrogen determinations do not alter the pattern of carbon depletion in the Carbon et al. (1982) data. Regarding nitrogen, the bottom panel shows a dispersion larger than 1 dex at all luminosities, and thus one cannot distinguish if either the nitrogen abundances are not altered along the RGB of M92 or, alternatively, if any pattern of nitrogen enhancement is lost in a larger dispersion of initial abundances.

Once again, we conclude that in order to bring our maximal mixing scenario in agreement with the data, either the diffusion velocities associated with hydrodynamic instabilities would have to be underestimated by about 2 orders of magnitude (FC $\sim$ 400), or turnoff stars in globular clusters need to have rapidly rotating interiors, in contrast with the helioseismological data. Finally, note the good agreement between the luminosity of the RGB bump in our models and that shown by the data, especially for the case of M4: the model with $V_{\rm TO} = 100$ km s^{-1} follows very closely the evolution of the ^{12}C/^{13}C ratio for the M4 giants from the lower RGB, across the onset of extra mixing right after the RGB bump, and up to the RGB tip.

As final remarks on Figure 18, let us address the controversial issue of the location of the onset of carbon depletion in M92. In contrast with the ^{12}C/^{13}C evolution of the field giants in the Gratton et al. (2000) sample (Fig. 16, *top panel*), as well as in M4 (Fig. 17*b*), the M92 giants do not show a clear break point in luminosity before which stars have high and approximately constant carbon abundances and after which they start to decline. Instead, what we see when going from brighter to less luminous stars is that the average carbon abundance slowly but progressively increases, without indication of leveling off at least as far as the least luminous data points are concerned, which belong already to M92's SGB.

Bellman et al. (2001) conclude that there is carbon depletion in M92 stars at least from $M_V = 0.5$ to 1.0 and, as most of the literature on the subject, regard this as a problem for the theory because such luminosity is well below that of the RGB bump in M92, which has been observationally determined to occur at $M_V = -0.4$ (Fusi Pecci et al. 1990) and is located at $M_V \approx -0.8$ in the models of Figure 18.

As stressed on various occasions in the present work, we think this just reflects the theoretical prejudice that a μ-barrier completely inhibits even the slightest amount of extra mixing until it gets erased or smoothed by the advancing HBS. Such a chocking off of the meridional currents responsible for the extra mixing might certainly turn out to be the case, but we argue that, at the time of writing this, there is no observational result that firmly establishes that as a fact. Thus, we let the extra mixing in our models occur whenever the conditions allow so, that is, whenever there is an energy reservoir available to drive the mixing, as equation (5) captures and is discussed elsewhere in this section. The end result is that, although in much smaller degree than after the RGB bump, our models of M92-like giants do show extra mixing as early as $M_V = 2.0$, which produces a much better agreement with the observed pattern of carbon depletion than models that assume complete inhibition of extra mixing before the RGB bump.

Furthermore, it is quite likely that the M92 giants we currently see come from MS progenitors polluted by the ashes of previous nucleosynthesis, and which therefore already had a large spread in carbon abundances before becoming giants. This is supported by the recent finding of Cohen et al. (2005) of a spread larger that 1 dex in the carbon abundances among M15 subgiants.

Next we explore the question of oxygen depletion. Metal-poor giants in the field do not show any variation of the oxygen abundance with position on the RGB, with $\langle$[O/Fe]$\rangle \approx 0.34$ and a dispersion of only $\sigma \sim 0.15$ dex at all luminosities from the MS turnoff to the tip of the RGB (Gratton et al. 2000). In globular clusters, on the other hand, the issue is controversial. This is not surprising because the effect itself is expected to be small: since oxygen burns at higher temperatures than carbon and nitrogen, the appearance of ON-processed material at the surface requires even deeper mixing than that needed to transport material enriched by CN burning. In addition, mixing of oxygen-depleted material is expected to be more evident with decreasing metallicity (Sweigart & Mengel 1979): being hotter, regions of ON

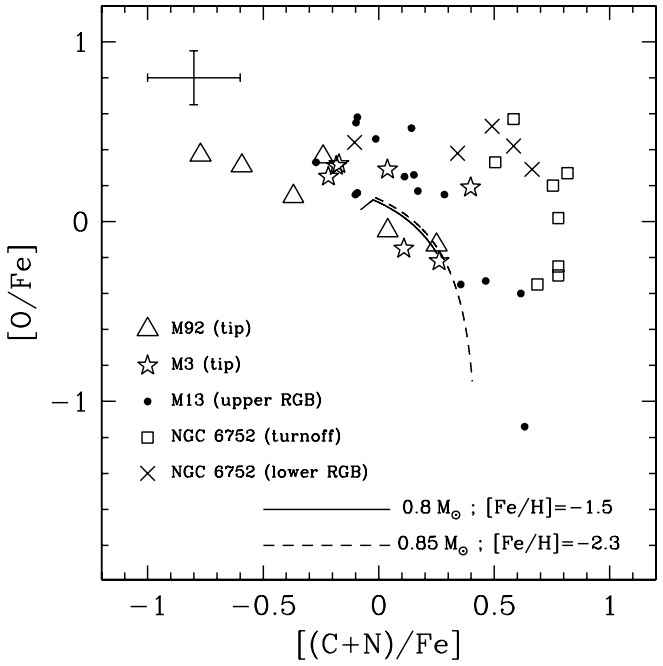

FIG. 19.—Oxygen and (C+N) in globular cluster giants. The signature of ON burning would be the depletion of oxygen accompanied by a simultaneous enhancement of the sum (C+N). Dashed and solid lines indicate ON burning in two of our most metal-poor rotating models.

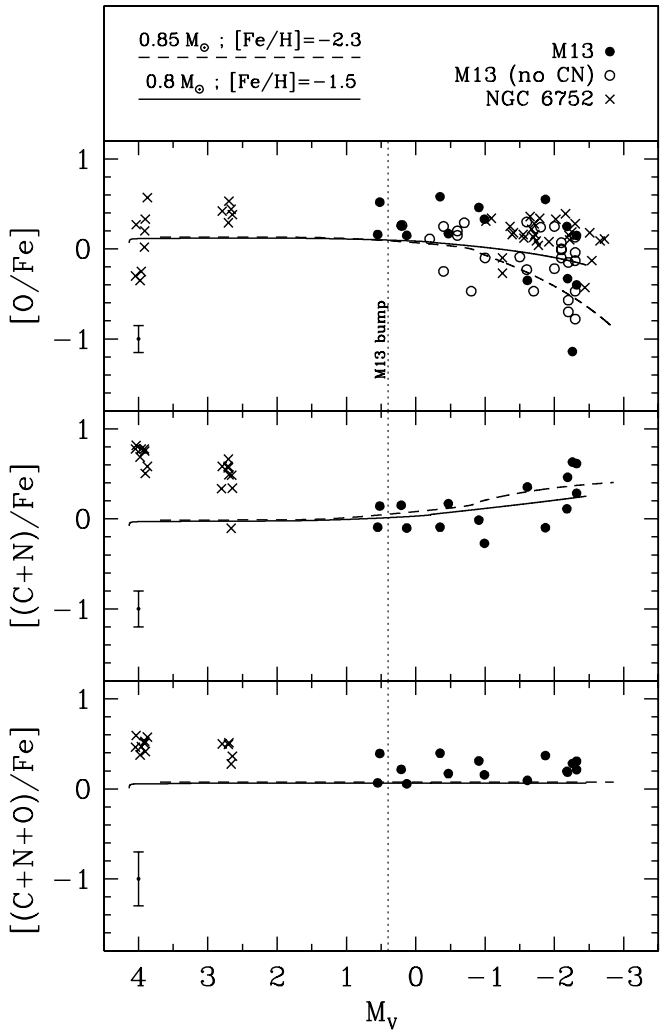

FIG. 20.—Oxygen depletion among M13 and NGC 6752 giants, together with carbon and nitrogen data when available. Also shown are the MS and lower RGB stars in NGC 6752 of Carretta et al. (2005). The same metal-poor rotating models of Fig. 19 are shown. The location of the RGB bump of M13 is indicated by the vertical dotted line at $M_V \sim 0.4$.

burning are closer to the surface in metal-poor stars than in more metal-rich ones. Finally, primordial variations in oxygen abundances, now known to exist, complicate the issue even more.

An apparent anticorrelation between the nitrogen and oxygen abundances in M92 giants, although restricted to a narrow range of luminosities close to the RGB tip, has been interpreted as evidence of mixing of ON-processed material (Pilachowski 1988; Sneden et al. 1991). Apart from being an intrinsically small effect, the evidence for oxygen depletion becomes controversial due to possibly large systematics between abundance determinations from different investigators, which might arise from the use of different spectral regions or differences in the spectral analysis. Thus, ideally, uncontroversial evidence for or against the occurrence of oxygen depletion should come from measured abundances of stars in the same cluster that, while sampling the extension of the RGB as best as possible, are obtained through a homogeneous procedure. However, such an example is still not available.

In order to investigate whether the extra mixing reaches regions of significant ON burning, we need first to isolate the effects of CN burning made evident by the pattern of carbon depletion in M92 (Fig. 18). This is achieved by comparing the oxygen abundances with the sum of carbon and nitrogen, (C+N), which should remain constant if only CN burning is involved. To this goal we use recent data for the globular clusters M13 (Cohen & Meléndez 2005; Brown et al. 1991) and NGC 6752 (Yong et al. 2003; Carretta et al. 2005), as well as data for M92 (Sneden et al. 1991) and M3 (Smith et al. 1996). M13 and NGC 6752 have approximately the same metallicity ([Fe/H] ~ -1.5), and, more importantly, they have giants with measured CNO abundances spanning a relatively wide range of luminosities along their RGBs, allowing an assessment of how these species evolve.

Figure 19 shows a comparison between oxygen and (C+N) abundances for all the stars with measured CNO abundances in the clusters under consideration, and Figure 20 shows the run of oxygen and (C+N) as a function of position on the RGB. Globally, the combined data in Figure 19 indicate an increasing spread in [O/Fe] when going toward higher (C+N), and clusters like M92 and M13 (*triangles and filled circles, respectively*) can have their giants separated into two distinct groups, one with high [O/Fe] and low (C+N), and another with low [O/Fe] and high (C+N). Nevertheless, there is also a clear primordial spread of [O/Fe], as evidenced by the MS turnoff stars of NGC 6752 (*open squares*).

In Figure 20, a fraction of the M13 giants close to the tip of the RGB are oxygen-poor with respect to all the less luminous giants in the same cluster, and it can be verified that this oxygen depletion corresponds to a simultaneous enhancement of the sum of (C+N) with increasing luminosity (Cohen & Meléndez 2005). Along with this anticorrelated evolution of oxygen and (C+N) on the upper RGB of M13, the total (C+N+O) remains constant, clearly indicating the appearance of ON-processed material at the surface. Although not shown in Figure 19 to avoid confusion and spanning a small range of luminosities, the seven M3 bright giants of Smith et al. (1996) also provide an indication of

ON-processed material having been mixed to the surface, by displaying (C+N+O) values clustered within a range of 0.3 dex, but, at the same time, (C+N) values dispersed within 0.6 dex.

In the case of NGC 6752 (*crosses*), while the lower RGB giants studied by Carretta et al. (2005) share, within the uncertainties, the same oxygen abundance ($\langle$[O/Fe]$\rangle \sim 0.4$), the giants on the upper RGB (Minniti et al. 1996) clearly show a lower average [O/Fe] and a substantial scatter, suggesting some depletion of oxygen along its RGB. Nevertheless, NGC 6752 already displays an anticorrelation of oxygen and CN among turnoff and lower RGB stars, and therefore any further oxygen burning on the upper RGB of this cluster occurs on top of these earlier patterns.

The models in Figures 19 and 20, which use mixing coefficients enhanced by a factor needed to reproduce the nuclear equilibrium values of $^{12}C/^{13}C$ on the upper RGB (FC = 400), are both able to deplete oxygen and produce an anticorrelation with (C+N) similar to that suggested by the data. They also show a strong metallicity dependence, with the M92-like model (0.85 $M_\odot$, [Fe/H] $= -2.3$) depleting about 5 times more oxygen than the model for giants in M13 and NGC 6752 (0.80 $M_\odot$, [Fe/H] $= -1.6$). However, the models, in general, do not span the entire ranges of [O/Fe] and (C+N) that the data occupy. This suggests that a significant part of the spread in (C+N) in M92 is of primordial origin, a conclusion also supported by the pattern of carbon depletion in Figure 18. The model with [Fe/H] $= -1.5$ does not deplete as much oxygen as is suggested by the giants of both M3 and M13. We note, nevertheless, that M13 is the globular cluster whose giants show the largest observed spread of oxygen abundances (see Fig. 12 of Ramírez & Cohen 2002).

6.4. *The Interaction between Rotation and Convection*

The most straightforward conclusion from our Population II results is that the efficiency of mixing in RGB stars is underestimated in our models. However, a simple rescaling of the diffusion coefficients to match the Population II abundances would certainly overmix the Population I models even at low mass, and the higher mass Population I giants are already overmixed relative to the data. The root cause is simple: in our models, the major factor governing the degree of rotational mixing in the radiative interior of red giants is the degree of rotation at the base of the surface convection zone. Empirically, this implies that the degree of rotational mixing does not increase with increased absolute angular momentum content to the degree implied in the models. We begin by justifying the physical basis for an interaction between convection and rotation, in the sense that the degree of differential rotation in convective regions decreases as the rotation rate increases. We then present some preliminary calculations on the magnitude of the change needed to explain the data.

There is strong evidence that the angular momentum distribution in convective regions depends on rotation and evolutionary state. In the solar convection zone the rotation velocity is comparable to, or larger than, typical convective velocities inferred from mixing-length theory; the latitude-averaged rotation period is independent of depth, consistent with a strong interaction between convection and rotation. By contrast, the survival of rapid rotation in metal-poor HB stars requires strong differential rotation with depth in the convective envelopes of their RGB precursors. This is not surprising; the convective envelopes of halo giants have a large moment of inertia and small starting angular momentum content, so the rotation velocities will be much less than the typical convective velocities (and there are many more pressure scale heights in the convective envelope of a giant than there are in the solar case). We therefore can infer that the angular momentum distribution in convective regions can vary between solid body and constant J/M as the number of pressure scale heights in the convection zone and the relative rotational and convective velocities differ. The higher mass Population I giants could therefore represent an intermediate case, with a shallower rotation velocity profile as a function of depth than the one expected from a simple extrapolation of the behavior of the very slowly rotating low-mass giants.

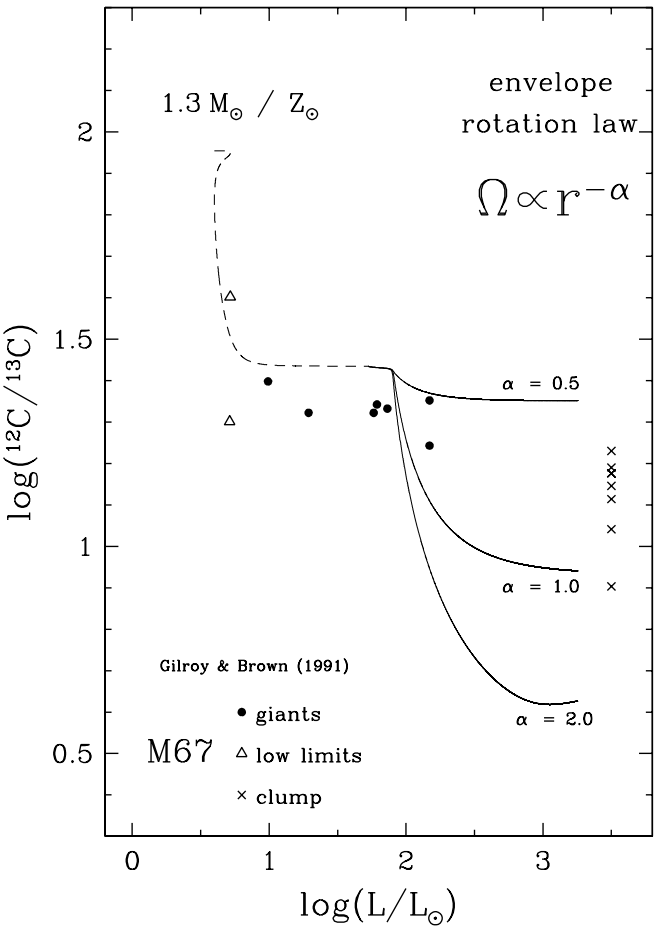

FIG. 21.—Dependence of canonical extra mixing (*solid lines*) on the angular momentum distribution of the convective envelope, as parameterized by α. The data shown are the same as in Fig. 14. The dashed line is a typical rotating model with very mild mixing and an initial rotation rate of 30 km s^{-1} at turnoff, appropriate for progenitors of current M67 giants. The solid lines are models with varying degrees of differential rotation in their convective envelopes. A much shallower profile than that required for globular cluster giants is needed to account for the $^{12}C/^{13}C$ levels of clump stars in M67. See § 6.4 for a detailed discussion.

We estimate the magnitude of the change needed as follows. We make use of the M67 data discussed in § 6.1 to determine how steep the angular momentum gradient in the convective envelope of an M67-like giant must be in order to reproduce the difference between the $^{12}C/^{13}C$ levels of the lower RGB giants and the clump giants in M67 while, at the same time, using diffusion coefficients (i.e., strength of extra mixing) scaled by the factor of $\sim$400 needed to account for the field and globular cluster $^{12}C/^{13}C$ ratios (§§ 6.2 and 6.3).

Our results are shown in Figure 21, where we plot a series of rotating models for an M67-like giant with canonical mixing

(that is, only from the RGB bump[5]) enhanced by FC = 400 and differentially rotating convection zones with varying angular velocity power laws. The initial surface rotation rate, at turnoff, is 30 km s^{-1}.

What concerns us here is the behavior past the RGB bump, when canonical extra mixing is strong. Starting from the bump model left by the run described above (end of dashed line in Fig. 21), we run models with the new diffusion coefficients (FC = 400) and with varying angular velocity profiles in the convective envelope, parameterized by $\Omega_{CZ} \propto r^{-\alpha}$ and shown by the solid lines in Figure 21.

The model with constant specific angular momentum ($\alpha = -2$), as expected from our results of § 6.1, mixes too much in comparison to what is needed to account for the $^{12}C/^{13}C$ levels of the clump stars in M67 (which, we recall, are supposed to represent the abundance ratios of tip giants in this cluster). The models with shallower rotation profiles in the envelope, however, mix less efficiently, as is expected from the discussion in § 5.1, and it can be verified that values of α between 0.5 and 1.0 can reproduce the $^{12}C/^{13}C$ ratios of clump stars.

In conclusion, we have shown that, assuming that the diffusion coefficients associated with extra mixing have been underestimated by about 2 orders of magnitude (which can be explained by more instabilities, higher order terms for angular momentum and composition transport, or additional physical mechanisms needed to be taken into account), one can reproduce the different mixing levels seen in Population I and Population II giants with the same models, underlying physics, and with their corresponding initial conditions (surface rotation rates and internal angular momentum distributions), provided that the convective envelopes of these two different populations respond differently to the degree of absolute rotation.

7. SUMMARY AND CONCLUSIONS

The problem addressed in the present work is an old one and consequently has been the subject of numerous investigations: to what extent can the CNO abundance anomalies seen in low-mass red giants be explained by extra mixing driven by rotationally induced hydrodynamic instabilities? This old question, however, has always been explored with at least one of two extremely important requirements either ignored or unsatisfactorily addressed. The first one is that whatever solution is put forward, it must be able to explain, using the same machinery and set of assumptions, the data on abundance patterns seen in Population II giants, as well as those of Population I. That is, the problem of abundance anomalies is not restricted to metal-poor stars in the field and globular clusters, but also extends to the more metal-rich red giants in open clusters, which must also be addressed. Second, any successful model must make use of initial conditions and assumptions in compliance with existent observations. Particularly, initial rotation rates must be adopted following data on rotation rates seen among stars of the type under study, and any assumptions on the distribution of angular momentum interior to the stars must similarly be based on some sort of empirical evidence. These two broad requirements are essential for a satisfactory solution to the problem of abundance anomalies in red giants and constitute the most important long-term goals of our efforts in the present work.

7.1. *Overall Properties of RGB Models with Rotational Mixing*

In agreement with previous work, models with rigidly rotating convective envelopes do not experience any extra mixing, while models with differentially rotating envelopes do (§ 5.1). Observations of fast rotation of HB stars in globular clusters strongly argue for a large reservoir of angular momentum in the interior of their progenitor red giants, which is only possible if these slowly rotating stars have their convective envelopes rotating differentially with depth (Sills & Pinsonneault 2000).

For giants with differentially rotating envelopes, the amount of extra mixing experienced on the RGB is highly dependent on the choice of the angular momentum profile of the progenitor MS turnoff star. The reason is that the quantity that ultimately determines the amount of rotational energy available to drive extra mixing is the angular momentum content of the material incorporated into the convective envelope during the standard dredge-up and that will later fall from the envelope into the radiative region above the HBS where extra mixing takes place. At a fixed surface rotation rate, this quantity is larger for a star that reaches the MS turnoff with a differentially rotating interior (i.e., its radiative core more rapidly spinning than its envelope) than for a turnoff star with a solid-body rotational profile such as that of the Sun (eq. [3]). As a consequence, the material that during the RGB ascent (past the first dredge-up) falls from the convective envelope into the radiative region where extra mixing takes place has a much higher angular velocity when the progenitor MS star had a rapidly spinning core than when its interior rotated at the same rate as its surface, and thus the former case will experience diffusion velocities much larger than the latter. However, there is no reason to expect that old MS turnoff stars would have rapidly spinning cores, while, actually, there are reasons to expect the opposite, with the flat rotational profile of the Sun among the strongest. Thus, we advocate that rotating RGB models should start from rigidly rotating turnoff stars, at least until either direct observations or indirect empirical evidence suggest otherwise.

We find that rotational mixing, albeit existent, is inefficient on the SGB and lower RGB, independently of any inhibiting effects of μ-gradients. Therefore, we argue against the widespread notion that the scarcity (or absence) of well-mixed stars on the lower RGB of globular clusters (i.e., before the bump) is evidence for the inhibiting effects of the μ-barriers. In our view, the ability of the star to experience extra mixing is directly proportional to its luminosity, so that when it is on the upper RGB it experiences much more mixing than during the lower RGB, when the available energy (luminosity) is much smaller. Whether μ-barriers do or do not inhibit mixing is an effect that goes on top of this more fundamental result.

As a consequence, the lack of CNO anomalies in giants below the RGB bump luminosity in globular clusters should not be taken as evidence for the inhibition of mixing by μ-barriers because mixing is inefficient during those stages anyway. Moreover, and for this very same reason, even if μ-barriers do indeed inhibit mixing, the CNO abundances should not be used to calibrate the effects of μ-barriers on mixing, as has been done in the past.

[5] The evolution through the SGB and lower RGB until the location of the RGB bump (*dashed line*) is done under the same conditions as those of the models in Fig. 14, that is, with the current estimations for the diffusion coefficients (FC = 1). Note that our use of different values of FC before and after the RGB bump is the sensible thing to do because of the different origins of rotational mixing in these two regimes: while mixing before the bump is a consequence of meridional circulation and depends on the degree of departure from spherical symmetry (absolute rotation rate), upper RGB canonical extra mixing operates only in the presence of large angular velocity gradients. Therefore, it is the latter mode of extra mixing that is affected by the details of the angular momentum distribution in the envelope and around which there exists considerable uncertainty regarding the actual size of the diffusion velocities associated with it. It is this type of extra mixing that we are calibrating using the factor FC in order to produce the mixing levels of bright globular cluster giants.

Nevertheless, our noninclusion of inhibiting effects by μ-barriers has the effect of rapidly smoothing, and eventually erasing, the RGB bump, in contradiction with the observational situation. We therefore conclude that the very existence of the RGB bump provides the first sound evidence for an inhibiting effect of mixing by μ-barriers, rather than the apparent lack of CNO mixing before the RGB bump. However, the peak in the LF that signals the bump is not a good diagnostic of the strength of this inhibition and simply indicates the previous existence of an effective wall for extra mixing. Better tests will be needed to attempt an empirical calibration of the effect of μ-barriers, one of the most promising being provided by HB stars (Sills & Pinsonneault 2000; Behr 2003).

For giants with differentially rotating envelopes, the degree of extra mixing is primarily determined by the initial rotation rate. Mass and metallicity effects are of second order. For fixed stellar mass and initial rotation rate, mixing is more efficient with decreasing metallicity. For fixed metallicity and rotation rate, lower mass stars experience more efficient mixing, but the effect is small.

Comparison between the CNO data for M13 and NGC 6752 (Figs. 19 and 20) argues for different initial mixtures of these elements from cluster to cluster. This, added to the different values of $^{12}C/^{13}C$ measured at different places in the Galaxy (§ 6.1), indicates that the usually adopted assumption of an initial $^{12}C/^{13}C$ ratio close to the solar value might be far from adequate. This is important in the context of models of low-mass giants because the exact post–first dredge-up value of $^{12}C/^{13}C$ depends on the starting adopted ratio.

7.2. *A Semiempirical Picture of Rotational Mixing*

Maximal mixing models of giants with differentially rotating convective envelopes that started from a rigidly rotating turnoff star are able to reproduce the surface $^{12}C/^{13}C$ data of giants in open clusters with initial rotation rates adequate to these stars but fail to do so in the case of metal-poor giants in both the field and globular clusters. Successful reproduction of the latter by these same models would require either prohibitively large initial rotation rates or else progenitor MS stars with rapidly spinning cores, requirements that are either not supported by current observational evidence or not yet probed with any current technique.

To reproduce the data, our models of field and globular cluster giants would require about 7 and 20 times faster initial rotation rates, respectively, than has been determined by observations. This means that, in order for rotationally induced instabilities to account for these data with reasonable initial conditions, one of the following two alternatives must be true: (1) the strength of mixing (i.e., the diffusion coefficients) associated with angular velocity gradients has been underestimated by factors of at least $7^2 \sim 50$ and $20^2 \sim 400$ for field and globular cluster giants, respectively, and so a serious revision of these theoretical computations is needed; or (2) higher order terms in the equations governing the evolution of the angular momentum and mixing inside the star, which have been neglected in our models, are actually important and need to be implemented. Among these we can mention the effects of gravity waves and magnetic fields, as well as the additional terms contemplated in the advection-diffusion scheme of Chaboyer & Zahn (1992) and Zahn (1992). These mechanisms are already beyond the scope of the present work, and thus we elaborated only on the first alternative.

The assumption that the mixing velocities have indeed been underestimated by a large factor, while solving the problem of field and globular cluster giants, would constitute, however, a new problem for the more metal-rich giants, since larger diffusion coefficients would now produce much more mixing than needed to account for the open cluster data. This is an inescapable result if one still requires, as we advocate in this work, that the same models are to be applied to both Population I and Population II giants and, furthermore, starting with sensible surface rotation rates for each stellar type.

There is, nevertheless, a possible solution to this dilemma, which, however, involves the interaction between convection and rotation. While convincing evidence for differential rotation in the convective envelopes of RGB stars exists, both from the observed levels of surface rotation of HB stars (Sills & Pinsonneault 2000) and from the fact that giants with rigidly rotating envelopes are not capable of any mixing, what remains as an open question is the degree of such differential rotation, that is, how steep is the angular velocity gradient between the stellar surface and the base of the convective envelope. We found in § 5.1, by exploring the two most extreme cases, that the shallower this gradient is, the less extra mixing is experienced by the star. Then, with the diffusion coefficients calibrated to match the globular cluster data with slow initial surface rotation, we showed that the only way to also account for the mixing levels seen in open cluster giants with their appropriate rotation rates is if they have convective envelopes with a significantly shallower angular velocity gradient than their metal-poor counterparts. If that were indeed the case, then our models of rotating giants with maximal mixing would be able to reproduce the patterns of CNO abundances shown by both Population I and Population II giants, with the same physics and using initial conditions in complete agreement with the known properties of these stars.

This conclusion, therefore, leads us to speculate if indeed we have indirectly come across important clues on the not well understood interaction between convection and rotation; that is, what the different levels of mixing in Population II and Population I giants might be telling us is simply that small levels of rotation (field and globular cluster stars) would allow the development of strong differential rotation in convective regions, while fast absolute rotation (the earlier type stars) would lead to convective regions with flatter rotation curves. In this sense, the different levels of mixing seen in giants of different populations would be just the result of the Kraft curve combined with the interaction between rotation and convection. Our results thus highlight the foremost importance of the study of the interaction between convection and rotation in stars (Kumar et al. 1995).

Finally, we end with a note on the kind of data that are needed to better constrain the theory and improve our understanding of mixing and the chemical evolution of stellar clusters. First, we need more data on red giants in open clusters with turnoff masses between 1 and 2 $M_{\odot}$. Open clusters of different ages have the crucial advantage of offering information on the mixing properties of stars of different masses, but our only source of information of this kind remains the works of Gilroy (1989) and Gilroy & Brown (1991), which contain only four clusters in this range of turnoff mass (Fig. 15) and, furthermore, with few giants in each case. Similarly, field metal-rich (Population I) giants with available parallaxes (so that their evolutionary state can be determined) are certainly available but also unexplored, and they should provide another window for understanding the mixing properties of stars and for refinement of the models. Second, applicable to all environments, the observing strategies should be ideally designed such that abundances are obtained as homogeneously as possible, so that possible systematics between

samples from different clusters or for different evolutionary states are minimized.

We are grateful to Ana Palacios and Corinne Charbonnel for valuable discussions during scientific meetings at the shores of Cancún and Tuscany, which led to significant improvements on this paper. We also thank Eugenio Carretta for providing us with data on the faint giants in 47 Tuc and NGC 6752 prior to publication. We are also grateful to the anonymous referee, whose questions and suggestions led to improvements to the manuscript. This work was supported in part by grant AST 02-06008 from the National Science Foundation to the Ohio State University Research Foundation.

APPENDIX

DIFFUSION COEFFICIENTS FOR SECULAR INSTABILITIES

For the secular shear we use the expression of Zahn (1992),

$$D_{\rm SS} = \frac{8}{45}{\rm Ri}_c K \left(\frac{r}{N}\frac{d\Omega}{dr}\right)^2, \tag{A1}$$

where ${\rm Ri}_c \lesssim \frac{1}{4}$ is the critical Richardson number and K is the thermal diffusivity. The buoyancy frequency N is given by $N^2 = g(\nabla_{\rm ad} - \nabla)/H_p$, where $\nabla_{\rm ad}$ and ∇ are, respectively, the adiabatic and actual temperature gradients, g is the gravity, and H_p is the pressure scale height. In the classical case the critical Richardson number is $\frac{1}{4}$, which we adopt for the current work. The instability is triggered if $D_{\rm SS} > \nu{\rm Re}_c/3$, where ν is the viscosity and ${\rm Re}_c$ is the critical Reynolds number; we take a value of 1000 from laboratory experiments on Couette flow.

For the GSF instability we use the expression of Kippenhahn et al. (1980),

$$D_{\rm GSF} = \frac{K_0}{2c_p\rho(\nabla_{\rm ad} - \nabla)}\frac{\tilde{g}}{g}\frac{H_p}{H_\Omega}, \tag{A2}$$

where $K_0 = 4acT^3/3\kappa\rho$, c_p is the heat capacity at constant pressure, $\tilde{g}/g$ is the departure from spherical symmetry, and H_Ω is the angular velocity scale height. To determine $\tilde{g}/g$ both here and in the expression for meridional circulation below, we use equation (3.23) from Zahn (1992) (an expression that includes the quadrupole term in the potential).

Our diffusion coefficient for meridional circulation has the form $D_{\rm eff} = f_c r U(r)$, where f_c is an efficiency factor for chemical mixing relative to angular momentum transport and the velocity $U(r)$ is taken, with some additional approximations, from equation (4.38) of Maeder & Zahn (1998) (which updates eq. [3.39] of Zahn 1992).

The Maeder & Zahn (1998) treatment for meridional circulation derives driving terms from variations in gravity, density, temperature, and mean molecular weight on isobars. Strong horizontal turbulence is invoked to turn a two-dimensional velocity field into a one-dimensional diffusion equation for chemical mixing and a one-dimensional diffusion plus advection equation for angular momentum transport. We make three simplifying assumptions relative to the extremely complex prescription therein. First, we retain only terms of order Ω and $d\Omega/dr$; second, we neglect the inhibiting or enhancing effect of μ gradients; and third, we assume that the efficiency factor f_c for chemical mixing relative to angular momentum transport is unity. The latter two assumptions are consistent with our maximal mixing approach, namely, considering the maximum degree of mixing consistent with a given angular velocity distribution. The higher order terms in the Maeder & Zahn (1998) treatment, in addition to being extremely challenging numerically, duplicate the physical driving mechanisms of the GSF instability that are already included in our treatment and are thus neglected for the current purpose along with the time-dependent driving terms from entropy variations from Maeder & Zahn (1998). Numerical experiments indicate that inclusion of these higher order terms largely leads to cancellation effects, with a final angular velocity comparable to that obtained with a simpler first-order treatment.

The expression we use is

$$U(r) = \frac{P}{\rho c_p T}\left(\frac{1}{\nabla_{\rm ad} - \nabla - \nabla_\mu}\right)\frac{\epsilon_m(r)}{g}E_\Omega, \tag{A3}$$

where $\nabla_\mu = d\ln\mu/dP$, $\epsilon_m(r) = L(r)/M(r)$, and E_Ω is given by a simplified version of equation (4.42) of Maeder & Zahn (1998),

$$E_\Omega = 2\left(1 - \frac{\Omega^2}{2\pi G\rho} - \frac{\epsilon}{\epsilon_m}\right)\frac{\tilde{g}}{g} - \frac{3M}{4\pi\rho r^3}\left(\frac{2}{3} - \frac{2H_T}{r}\right)\Theta - \frac{\epsilon}{\epsilon_m}\left(\frac{\epsilon_*}{\epsilon}\frac{d\epsilon_*}{dT} - \frac{dK_0}{dT} + 1 - \frac{\epsilon_*}{\epsilon}\right)\Theta. \tag{A4}$$

In this last expression, the specific rate ϵ refers to the sum of nuclear and gravitational energies, while ϵ_* includes the nuclear energy only. Finally, H_T is the temperature scale height, and the factor Θ represents density fluctuations and is given by

$$\Theta = \frac{\tilde{\rho}}{\rho} = \frac{1}{3}\frac{r^2}{g}\frac{d(\Omega^2)}{dr}. \tag{A5}$$

REFERENCES

Alexander, D. R., & Ferguson, J. W. 1994, ApJ, 437, 879
Allard, F., & Hauschildt, P. H. 1995, ApJ, 445, 433
Armosky, B. J., Sneden, C., Langer, G. E., & Kraft, R. P. 1994, AJ, 108, 1364
Bahcall, J. N., Pinsonneault, M. H., & Basu, S. 2001, ApJ, 555, 990
Balachandran, S. 1995, ApJ, 446, 203
Barnes, S. A. 2003, ApJ, 586, 464
Behr, B. 2003, ApJS, 149, 67
Bellazzini, M., Ferraro, F. R., Origlia, L., Cacciari, C., Pancino, E., Monaco, L., & Oliva, E. 2002, AJ, 124, 3222
Bellazzini, M., Ferraro, F. R., & Pancino, E. 2001, MNRAS, 327, L15
Bellman, S., Briley, M. M., Smith, G. H., & Claver, C. F. 2001, PASP, 113, 326
Bessell, M. S., & Norris, J. 1982, ApJ, 263, L29
Boesgaard, A. M., & Tripicco, M. J. 1986, ApJ, 302, L49
Boothroyd, A. I., & Sackmann, I.-J. 1999, ApJ, 510, 232
Briley, M. M., Cohen, J. G., & Stetson, P. B. 2002, ApJ, 579, L17
Briley, M. M., Smith, V. V., King, J., & Lambert, D. L. 1997, AJ, 113, 306
Brown, J. A., & Wallerstein, G. 1992, AJ, 104, 1818
Brown, J. A., Wallerstein, G., & Oke, J. B. 1991, AJ, 101, 1693
Carbon, D. F., Langer, G. E., Butler, D., Kraft, R. P., Suntzeff, N. B., Kemper, E., Trefzger, C. F., & Romanishin, W. 1982, ApJS, 49, 207
Carretta, E., Gratton, R. G., Lucatello, S., Bragaglia, A., & Bonifacio, P. 2005, A&A, 433, 597
Chaboyer, B., Demarque, P., & Pinsonneault, M. H. 1995a, ApJ, 441, 865
———. 1995b, ApJ, 441, 876
Chaboyer, B., & Zahn, J.-P. 1992, A&A, 253, 173
Charbonneau, P., & MacGregor, K. B. 1992, ApJ, 387, 639
———. 1993, ApJ, 417, 762
Charbonnel, C. 1994, A&A, 282, 811
———. 1995, ApJ, 453, L41
Charbonnel, C., Brown, J. A., & Wallerstein, G. 1998, A&A, 332, 204
Charbonnel, C., Vauclair, S., & Zahn, J.-P. 1992, A&A, 255, 191
Cohen, J. G., Briley, M. M., & Stetson, P. B. 2002, AJ, 123, 2525
———. 2005, AJ, submitted (astro-ph/0505263)
Cohen, J. G., & Meléndez, J. 2005, AJ, 129, 303
Denissenkov, P. A., Da Costa, G. S., Norris, J. E., & Weiss, A. 1998, A&A, 333, 926
Denissenkov, P. A., & Denisenkova, S. N. 1990, Soviet Astron. Lett., 16, 275
Denissenkov, P. A., & Herwig, F. 2003, ApJ, 590, L99
Denissenkov, P. A., & Tout, C. A. 2000, MNRAS, 316, 395
Denissenkov, P. A., & VandenBerg, D. A. 2003, ApJ, 593, 509
Denissenkov, P. A., & Weiss, A. 1996, A&A, 308, 773
———. 2001, ApJ, 559, L115
———. 2004, ApJ, 603, 119
Eddington, A. S. 1925, Observatory, 48, 73
———. 1929, MNRAS, 90, 54
Endal, A. S., & Sofia, S. 1976, ApJ, 210, 184
———. 1978, ApJ, 220, 279
Ferraro, F. R., Messineo, M., Fusi Pecci, F., de Palo, M. A., Straniero, O., Chieffi, A., & Limongi, M. 1999, AJ, 118, 1738
Fulbright, J. P., & Johnson, J. A. 2003, ApJ, 595, 1154
Fusi Pecci, F., Ferraro, F. R., Crocker, D. A., Rood, R. T., & Buonanno, R. 1990, A&A, 238, 95
Galilei, G., Welser, M., & de Filiis, A. 1613, Istoria E dimostrazioni intorno alle macchie solari E loro accidenti comprese in tre lettere scritte all'illvstrissimo signor Marco Velseri Linceo, In Roma, MDCXIII
Gilroy, K. K. 1989, ApJ, 347, 835
Gilroy, K. K., & Brown, J. A. 1991, ApJ, 371, 578
Goto, M., et al. 2003, ApJ, 598, 1038
Gratton, R. G., Sneden, C., Carretta, E., & Bragaglia, A. 2000, A&A, 354, 169
Grevesse, N., & Sauval, A. J. 1998, Space Sci. Rev., 85, 161
Grocholski, A. J., & Sarajedini, A. 2003, MNRAS, 345, 1015
Grundahl, F., Briley, M., Nissen, P. E., & Feltzing, S. 2002, A&A, 385, L14
Gruzinov, A., & Bahcall, J. N. 1998, ApJ, 504, 996
Guenther, D. B., Demarque, P., Kim, Y.-C., & Pinsonneault, M. H. 1992, ApJ, 387, 372
Harris, W. E., et al. 1997, AJ, 114, 1030
Henry, R. B. C., Edmunds, M. G., & Köppen, J. 2000, ApJ, 541, 660
Iben, I. 1965, ApJ, 142, 1447
Iglesias, C. A., & Rogers, F. J. 1996, ApJ, 464, 943
Israelian, G., Ecuvillon, A., Rebolo, R., García-López, R., Bonifacio, P., & Molaro, P. 2004, A&A, 421, 649
Ivans, I. I., Kraft, R. P., Sneden, C., Smith, G. H., Rich, R. M., & Shetrone, M. 2001, AJ, 122, 1438
Ivans, I. I., Sneden, C., Kraft, R. P., Suntzeff, N. B., Smith, V. V., Langer, G. E., & Fulbright, J. P. 1999, AJ, 118, 1273
Izotov, Y. I., & Thuan, T. X. 2004, ApJ, 602, 200
Johnson, J. A., & Bolte, M. 1998, AJ, 115, 693
Keller, L. D., Pilachowski, C. A., & Sneden, C. 2001, AJ, 122, 2554
King, C. R., Da Costa, G. S., & Demarque, P. 1985, ApJ, 299, 674
Kippenhahn, R., Ruschenplatt, G., & Thomas, H.-C. 1980, A&A, 91, 181
Kippenhahn, R., & Thomas, H.-C. 1970, in Stellar Rotation, ed. A. Slettbak (Dordrecht: Reidel), 20
Kippenhahn, R., & Weigert, A. 1990, Stellar Structure and Evolution (Berlin: Springer)
Kraft, R. P. 1967, ApJ, 150, 551
———. 1994, PASP, 106, 553
Kraft, R. P., Sneden, C., Langer, G. E., Shetrone, M. D., & Bolte, M. 1993, AJ, 106, 1490
———. 1995, AJ, 109, 2586
Kraft, R. P., Sneden, C., Smith, G. H., Shetrone, M. D., & Fulbright, J. 1998, AJ, 115, 1500
Kraft, R. P., Sneden, C., Smith, G. H., Shetrone, M. D., Langer, G. E., & Pilachowski, C. A. 1997, AJ, 113, 279
Kumar, P., Narayan, R., & Loeb, A. 1995, ApJ, 453, 480
Kumar, P., & Quataert, E. J. 1997, ApJ, 475, L143
Kumar, P., Talon, S., & Zahn, J.-P. 1999, ApJ, 520, 859
Langer, G. E., Hoffman, R., & Sneden, C. 1993, PASP, 105, 301
Langer, G. E., Kraft, R. P., Carbon, D. F., Friel, E., & Oke, J. B. 1986, PASP, 98, 473
Langer, W. D., & Penzias, A. A. 1990, ApJ, 357, 477
Lejeune, T., Cuisinier, F., & Buser, R. 1998, A&AS, 130, 65
Li, Y., & Burstein, D. 2003, ApJ, 598, L103
Lucatello, S., & Gratton, R. G. 2003, A&A, 406, 691
Maeder, A., & Meynet, G. 2000, ARA&A, 38, 143
———. 2003, A&A, 411, 543
———. 2004, A&A, 422, 225
Maeder, A., & Zahn, J.-P. 1998, A&A, 334, 1000
Majewski, S. R., Siegel, M. H., Patterson, R. J., & Rood, R. T. 1999, ApJ, 520, L33
Melo, C. H. F., Pasquini, L., & De Medeiros, J. R. 2001, A&A, 375, 851
Mestel, L. 1953, MNRAS, 113, 716
Mestel, L., & Weiss, N. O. 1987, MNRAS, 226, 123
Meynet, G., & Maeder, A. 1997, A&A, 321, 465
Michaud, G., Richard, O., Richer, J., & VandenBerg, D. A. 2004, ApJ, 606, 452
Minniti, D., Peterson, R. C., Geisler, D., & Clariá, J. J. 1996, ApJ, 470, 953
Monaco, L., Ferraro, F. R., Bellazzini, M., & Pancino, E. 2002, ApJ, 578, L47
Montgomery, K. A., Marschall, L. A., & Janes, K. A. 1993, AJ, 106, 181
Norris, J. E., Ryan, S. G., & Beers, T. C. 2001, ApJ, 561, 1034
Norris, J. E., Ryan, S. G., Beers, T. C., Aoki, W., & Ando, H. 2002, ApJ, 569, L107
Pagel, B. E. J. 1997, Nucleosynthesis and Chemical Evolution of Galaxies (Cambridge: Cambridge Univ. Press)
Palacios, A., Talon, S., Charbonnel, C., & Forestini, M. 2003, A&A, 399, 603
Peterson, R. C. 1980, ApJ, 237, L87
Pilachowski, C., Sneden, C., Freeland, E., & Casperson, J. 2003, AJ, 125, 794
Pilachowski, C., Sneden, C., Hinkle, K., & Joyce, R. 1997, AJ, 114, 819
Pilachowski, C. A. 1988, ApJ, 326, L57
Pinsonneault, M. H. 1997, ARA&A, 35, 557
Pinsonneault, M. H., Kawaler, S. D., & Demarque, P. 1990, ApJS, 74, 501
Pinsonneault, M. H., Kawaler, S. D., Sofia, S., & Demarque, P. 1989, ApJ, 338, 424
Press, W. H. 1981, ApJ, 245, 286
Ramírez, S., & Cohen, J. 2002, AJ, 123, 3277
———. 2003, AJ, 125, 224
Richer, H. B., et al. 1997, ApJ, 484, 741
Rogers, F. J., Swenson, F. J., & Iglesias, C. A. 1996, ApJ, 456, 902
Salaris, M., Cassisi, S., & Weiss, A. 2002, PASP, 114, 375
Saumon, D., Chabrier, G., & van Horn, H. M. 1995, ApJS, 99, 713
Shetrone, M. D. 1996a, AJ, 112, 1517
———. 1996b, AJ, 112, 2639
———. 2003, ApJ, 585, L45
Shetrone, M. D., Sneden, C., & Pilachowski, C. A. 1993, PASP, 105, 337
Sills, A., & Pinsonneault, M. H. 2000, ApJ, 540, 489
Sills, A., Pinsonneault, M. H., & Terndrup, D. M. 2000, ApJ, 534, 335
Smith, G. H., & Martell, S. L. 2003, PASP, 115, 1211
Smith, G. H., Shetrone, M. D., Bell, R. A., Churchill, C. W., & Briley, M. M. 1996, AJ, 112, 1511
Smith, G. H., & Tout, C. A. 1992, MNRAS, 256, 449
Smith, V. V., Terndrup, D. M., & Suntzeff, N. B. 2002, ApJ, 579, 832
Sneden, C., Kraft, R. P., Langer, G. E., Prosser, C. F., & Shetrone, M. D. 1994, AJ, 107, 1773
Sneden, C., Kraft, R. P., Prosser, C. F., & Langer, G. E. 1991, AJ, 102, 2001

Sneden, C., Kraft, R. P., Prosser, C. F., & Langer, G. E. 1992, AJ, 104, 2121
Sneden, C., Kraft, R. P., Shetrone, M. D., Smith, G. H., Langer, G. E., & Prosser, C. F. 1997, AJ, 114, 1964
Spruit, H. C. 1999, A&A, 349, 189
———. 2002, A&A, 381, 923
Suntzeff, N. B., & Smith, V. V. 1991, ApJ, 381, 160
Sweigart, A. V., & Mengel, J. G. 1979, ApJ, 229, 624
Talon, S., & Charbonnel, C. 1998, A&A, 335, 959
———. 2003, A&A, 405, 1025
———. 2004, A&A, 418, 1051
Talon, S., Kumar, P., & Zahn, J.-P. 2002, ApJ, 574, L175
Talon, S., & Zahn, J.-P. 1998, A&A, 329, 315
Talon, S., Zahn, J.-P., Maeder, A., & Meynet, G. 1997, A&A, 322, 209
Tautvaisiene, G., Edvardsson, B., Tuominen, I., & Ilyin, I. 2000, A&A, 360, 499
Tomczyk, S., Schou, J., & Thompson, M. J. 1995, ApJ, 448, L57
Vogt, H. 1925, Astron. Nachr., 223, 229
von Zeipel, H. 1924, MNRAS, 84, 665
Wasserburg, G. J., Boothroyd, A. I., & Sackmann, I.-J. 1995, ApJ, 447, L37
Weiss, A., Denissenkov, P., & Charbonnel, C. 2000, A&A, 356, 181
Wolff, S. C., & Simon, T. 1997, PASP, 109, 759
Yong, D., Grundahl, F., Lambert, D. L., Nissen, P. E., & Shetrone, M. D. 2003, A&A, 402, 985
Zahn, J.-P. 1992, A&A, 265, 115
Zahn, J.-P., Talon, S., & Matias, J. 1997, A&A, 322, 320
Zoccali, M., Cassisi, S., Piotto, G., Bono, G., & Salaris, M. 1999, ApJ, 518, L49